UNIVERSITÀ
DEGLI STUDI
FIRENZE

PhD in
Atomic and Molecular Photonics

CYCLE XXXII

COORDINATOR Prof. Francesco S. Cataliotti

ENHANCEMENT OF INCLINED OPTICAL SHEET ILLUMINATION AND ITS APPLICATION TO QUANTITATIVE SUPER-RESOLUTION MICROSCOPY

Academic Discipline (SSD) FIS/03

Doctoral Candidate Vignolini Tiziano	Supervisor Dr. Capitanio Marco
(signature)	(signature)
Co-supervisor Dr. Gardini Lucia	Coordinator Prof. Cataliotti Francesco S.
(signature)	(signature)

Years 2016/2019

Contents

INTRODUCTION

PART I - CHARACTERIZATION AND IMPROVEMENT OF HIGHLY INCLINED OPTICAL SHEET ILLUMINATION FOR SINGLE-MOLECULE LOCALIZATION MICROSCOPY

PART II - QUANTITATIVE IMAGING OF EFFLUX PUMPS IN PLANKTONIC AND BIOFILM-ASSOCIATED BACTERIA THROUGH SINGLE-MOLECULE LOCALIZATION MICROSCOPY

INTRODUCTION

Over the last couple of decades, the field of optical microscopy has been revolutionized by the possibility of breaking the diffraction limit, which ushered in the new era of “super-resolution”. Optical techniques can now produce images of biological systems with a level of detail that was previously only accessible via specialized methods, such as electron or scanning probe microscopy. The 2014 Nobel Prize in Chemistry, won by super-resolution pioneers William Moerner, Eric Betzig and Stefan Hell, vastly popularized these techniques and sprouted a widespread interest in both finding useful applications for super-resolution microscopy and expanding its capabilities.

Among the various existing super-resolution microscopy techniques, localization-based methods such as PALM and STORM are the ones that can achieve the highest image resolutions (a few tens of nanometers), and they also provide information at the single-molecule level. However, they suffer from two fundamental drawbacks: the first is the long time necessary to acquire these kinds of images (ranging from minutes to hours), which severely limits the applicability of PALM and STORM to non-fixed, living biological samples; the other is the high susceptibility of these techniques to factors of noise influencing the signal-to-background ratio, such as signal coming from out-of-focus planes in the acquired images: as the amount of photons produced by individual fluorescent molecules is very low, fluorescence background in the image can easily mask the on-focus signal, which in turn leads to inefficient sampling and image artifacts, especially for densely labelled, highly scattering or intrinsically fluorescent specimens.

Localization-based super-resolution techniques also carry an intrinsic capability of providing not only qualitative information on the underlying structure of a fluorescent specimen, but also quantitative information on the number and position of the fluorescent molecules composing it. However, this capability is seldom exploited by researchers applying PALM and STORM to their research, as common experimental designs do not allow for it – e.g., because they employ labelling strategies that insert an arbitrary amount of fluorescent molecules in the sample, limiting the obtainable information to qualitative structural data.

This doctoral dissertation reports our work in addressing the aforementioned issues of (i) improving single-molecule localization microscopy techniques when it comes to acquisition times and susceptibility to background fluorescence, and (ii) employing localization-based methods to obtain quantitative single-molecule data with an ad hoc experimental design.

This thesis is therefore divided in two main parts. Part I deals with our efforts to characterize and improve the fluorescence excitation methods employed in PALM and STORM imaging. After introducing and explaining in detail the principles behind these techniques, we present our newly developed methods for measuring some crucial parameters of a fluorescence excitation system (e.g.: the thickness of the specimen volume undergoing excitation, the achievable signal-to-background ratio, and the sampling efficiency in single-molecule localization experiments). We also report on our improvements on the current state-of-the-art, showing that reducing the fluorescence excitation volume to subcellular sizes leads to a massive improvement in fluorophore sampling when applied to STORM imaging.

Part II deals with our efforts towards obtaining quantitative single-molecule information from PALM imaging, and with our application of a quantitative PALM technique to the study of an open biological problem. We introduce the issue of bacterial efflux pumps, which are a class of proteins that mediate antimicrobial resistance in a growing number of pathogens. We report on our development of a genomically engineered *Escherichia coli* strain,

encoding for a fluorescent version of the AcrB efflux pump, that we expressly designed to be used in quantitative PALM imaging. We describe our method for directly counting the number of copies of AcrB contained in individual bacteria via super-resolution microscopy, and we report our preliminary findings on the varying expression of this protein under planktonic and biofilm-associated growth. Moreover, we describe the application of our experimental strain and technique to elucidate the mechanism of action of a novel antimicrobial drug.

PART I

–

CHARACTERIZATION AND IMPROVEMENT OF HIGHLY INCLINED OPTICAL SHEET ILLUMINATION FOR SINGLE-MOLECULE LOCALIZATION MICROSCOPY

1 Single-molecule localization microscopy

Fluorescence microscopy has been an invaluable tool for understanding the inner workings of biological systems for more than a century. Oskar Heimstäd developed the first fluorescence microscope in 1911, which he used to image the natural fluorescence of bacteria[1], while Max Haitinger introduced the concept of fluorescent staining with exogenous chemicals in 1933[2], coining the term "fluorochrome". However, arguably, the biggest leap towards fluorescence microscopy as we know it today happened in 1941, when Albert Coons described the use of fluorescently labelled antibodies to selectively label Type III pneumococci, at first with cultured bacteria[3] and subsequently in the tissues of infected mice[4]. With the advent of fluorescent antibodies came the possibility to look at specific components of biological entities, and with further development of optical technologies in the following decades the detail achievable by fluorescence microscopy switched from the tissue, to the cellular, to the subcellular level. Fluorescence microscopy represents nowadays an unparalleled tool to study the functional anatomy of cells.

However, fluorescence microscopy, as other light microscopy techniques, suffers from one great limitation: its spatial resolution. In 1873, Ernst Abbe reported that there was a theoretical limit to the resolving power of a light-based microscope[5], which is to say the minimal distance that two points may have between each other while still being resolvable. This distance depends on the wavelength of light λ used to create the image (the longer the wavelength, the larger the distance, the lower the resolution) and on the numerical aperture of the microscope objective NA as follows:

$$d = \frac{\lambda}{2NA}$$

Equation 1

For visible light microscopy, this distance sits at around 200 nanometers. This resolution is adequate to look at relatively large features such as organelles and cellular compartments, but many subcellular structures are much smaller than that, with the thickness of cell membranes ranging from 4 to 10 nanometers and proteins averaging at 3-6 nanometers in diameter[6]. Under a conventional fluorescence microscope, details such as the branched actin filaments in the cytoskeleton of mammalian cells are completely unresolvable[7].

But from the same phenomenon of fluorescence comes also one of the solutions to this technical limitation. Single-molecule localization microscopy (SMLM) is an umbrella term encompassing all light microscopy techniques that employ the highly precise localization of isolated fluorescence emitters to achieve “super-resolution”, which is to say a higher spatial resolution than the one allowed by Abbe’s theoretical limit. As I am going to explain in detail in the next few chapters of this thesis, it is possible to determine the position of an isolated fluorescent molecule with an extremely high precision – with an uncertainty as small as 1 nanometer in the proper conditions[8] – as long as this molecule is sufficiently far from its fluorescent neighbors to be individually resolvable. This trick can be used to obtain otherwise inaccessible information on nanoscale structures within living cells (Figure 1), and also to observe and follow individual proteins as they perform their functions in real time.

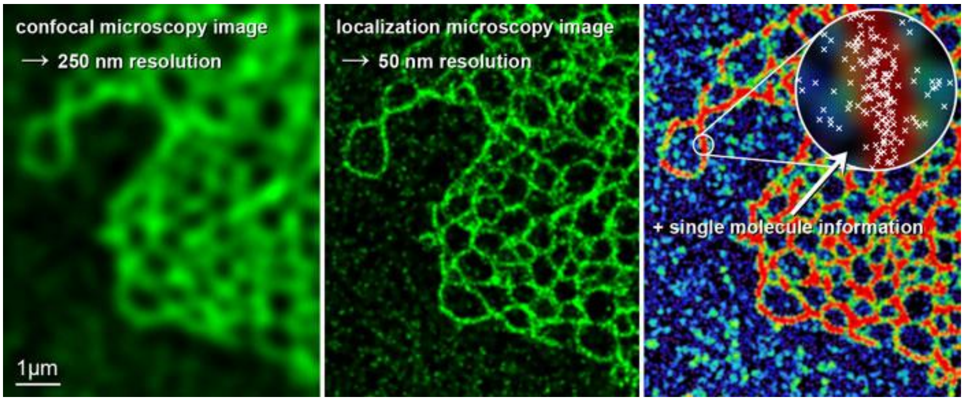

Figure 1. By determining the position of the individual molecules making up a fluorescent sample, SMLM techniques achieve much higher resolutions than conventional optical microscopy. Image retrieved from [9].

1.1 The diffraction limit and optical resolution

When light passes through a circular aperture it is diffracted, creating a diffraction pattern known as an "Airy disk"[10]. A lens such as a microscope objective acts like a circular aperture in this regard, and so every point-like source of light in the observed sample will appear as an Airy disk pattern in the final image (Figure 2). The diffraction pattern generated from a point-like source by a given optical system is also called the "point spread function" (or PSF), and the image generated by a distribution of point-like sources will therefore be a convolution of the PSFs of all points.

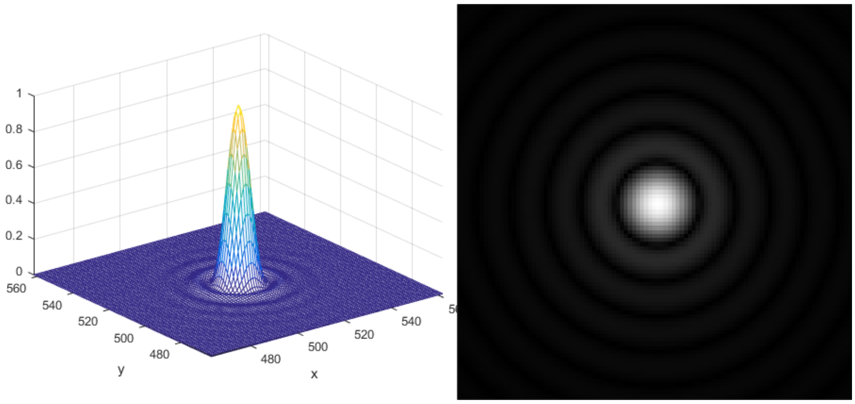

Figure 2. The Airy diffraction pattern generated by a point-like source on a camera chip. Image retrieved from [11]

Based on this phenomenon, several criteria have been proposed to set the minimum distance between two light point sources for them to be fully resolved. The Rayleigh and Abbe criteria are commonly used in microscopy and they respectively define the distance where two PSFs overlap as described in Figure 3.

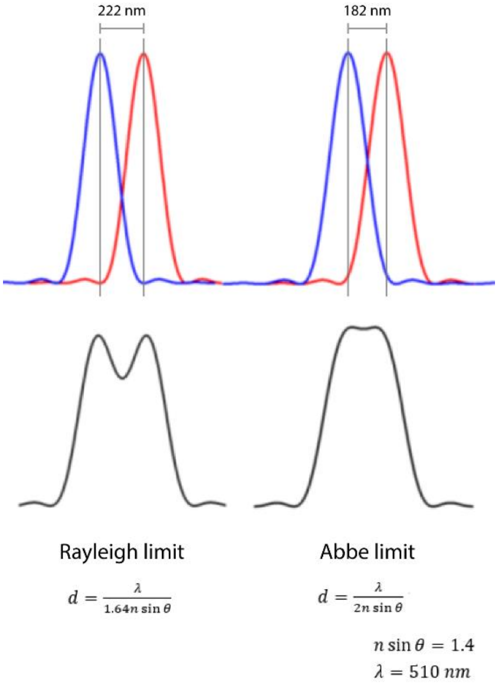

Figure 3. The Rayleigh and Abbe diffraction limits and their definitions. The values are calculated for two point-like sources emitting at a wavelength of 510 nm and being imaged by an objective with a numerical aperture of 1.4. In the upper panel, pairs of Airy patterns are plotted at the distance given by the respective diffraction limit. In the lower panel, the summed profiles are shown.

Where d is the minimal resolvable distance according to each criterion. For the Rayleigh criterion, it corresponds to the distance where the minimum of the first PSF overlaps with the maximum of the second (and vice versa); for the Abbe criterion, it corresponds to a distance at which the peak of one Airy function overlaps with the second function where its value is equal to zero. In all cases, d depends on the wavelength λ emitted by the light source, the refractive index of the medium in which the objective is immersed (n), and half of the objective aperture angle θ (Figure 4). The term $n \sin\theta$ is called the numerical aperture (NA) of the objective, which can usually reach a maximum value of about 1.4 – 1.5 for common oil immersion objectives.

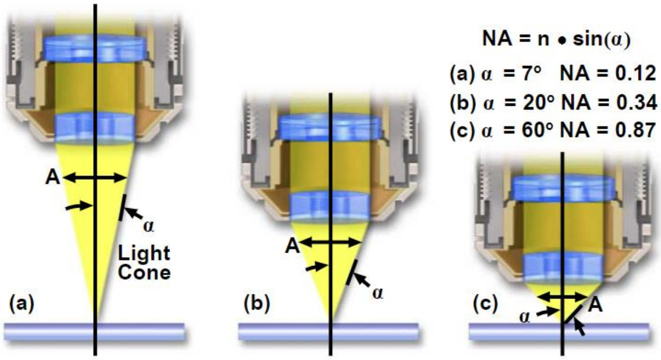

Figure 4. Numerical aperture. This example is referring to objectives working in air. To obtain values of NA>1 the objective needs to be immersed in a medium with a refractive index n>1, such as water or oil. Image retrieved from [12].

All of these three criteria set the maximum resolution achievable with an optical microscope to a value between $^1/_2$ and $^1/_3$ of the emitted wavelength, which is about 200 nm.

This number has historically been considered to be the ultimate limit of optical microscopy. Until something more than a decade ago, the only ways to achieve a higher imaging resolution were to either use shorter wavelengths such as the ultraviolet – which was first achieved by August Köhler in 1904[13] – or electrons, having much shorter wavelengths than visible light, ranging from tens of picometers to fractions of a picometer depending on their energy[14] – with the first electron microscope developed by Ernst Ruska in 1931[15].

But in more recent years, a plethora of techniques have emerged that allow investigators to reach a much higher spatial resolution while using visible light microscopy. These techniques have been grouped under the general description of "super-resolution microscopy", but their working principles vary greatly. In this thesis I am going to focus on one category of super-resolution microscopy methods, the so-called “stochastic super-resolution”, which rely on the principle of single-molecule localization to achieve extremely high spatial resolutions.

1.2 Fitting the PSF: 3D localization of single molecules

As discussed previously, Abbe’s law sets a limit to the minimum distance resolvable by an optical microscope, meaning that every object smaller than this limit will appear as a diffraction-limited spot in the image produced by the system. It is impossible to discriminate between multiple objects which are closer together than this resolution limit, but if the diffraction-limited spot is generated by a single light source, it is possible to localize the center of this spot – and as such the position of the object – with a much higher precision.

As mentioned in the previous section, it is known from wave propagation theory that the diffraction pattern generated by a sub-diffraction light source on the focal plane of an optical system (the PSF) is described by an Airy function (Figure 2). Indeed, for a single fluorescent dye imaged on a fluorescence microscope the shape of the PSF can be fairly described as a two-dimensional Gaussian[16], the Airy pattern being hindered by the surrounding background fluorescence signal. Based on this assumption, it has been proven that the intensity profile created on the focal plane of an optical system by a sub-diffraction sized fluorescent probe can be fitted with a two-dimensional Gaussian model function, which allows to localize the center of the peak (Figure 5).

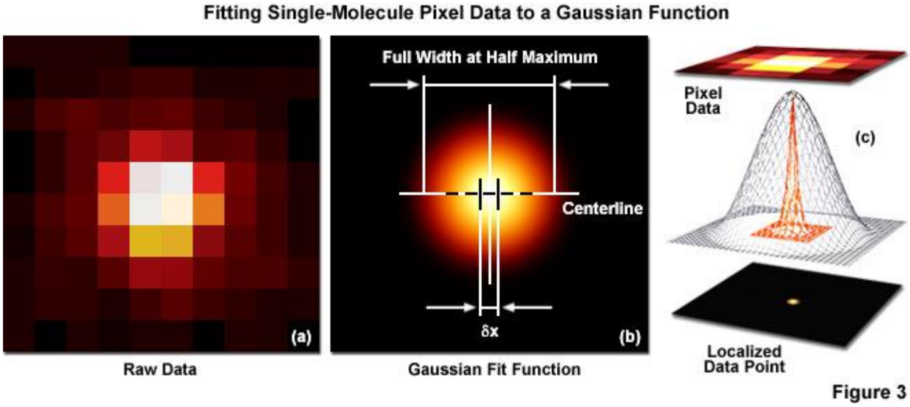

Figure 5. schematic illustration of the single-molecule localization process. The image of a single emitter (a) is fitted with a two-dimensional Gaussian function and localized with nanometer accuracy (δx) (b). The entire process is summarized in (c), where the standard deviation of the orange Gaussian is equal to δx. Image retrieved from [17].

The precision to be associated to the localized x,y coordinates has been fully characterized by Thompson *et al.* in 2002[18], who determined its exact dependence on some experimental parameters and consequently set the technical requirements to reach nanometer-level localization precisions:

$$\langle(\Delta x)^2\rangle = \frac{s^2 + a^2/12}{N} + \frac{8\pi s^4 b^2}{a^2 N^2}$$

Equation 2

Here, the localization precision $\sqrt{\langle(\Delta x)^2\rangle}$ is expressed as the standard error of the mean on the Gaussian profile fitted on the diffraction-limited spot. Its value depends on a number of factors:

- The s term is the standard deviation of the Gaussian function fitted on the diffraction-limited spot, which is directly dependent on the wavelength used and on the NA of the objective, as per Abbe's law.
- The a term is the pixel size of the image.

- The b term is the background signal, calculated as the standard deviation of the residuals between the raw data and the fitted Gaussian profile.
- N is the amount of detected photons.

It follows from the above that the uncertainty on the position of the fluorescent particle being imaged can be reduced by employing optics and wavelengths which produce a smaller PSF (acting on the s term), by reducing the noise factors in the picture (the b term), or by maximizing the amount of collected photons (the N term) through the use of highly bright fluorophores, high numerical aperture objectives and very sensitive cameras. The a term is more ambivalent, as pixel size is directly correlated with the amount of detected photons per pixel, but smaller pixels allow for better sampling of the PSF profile.

Given a certain optical setup, the localization uncertainty can be made arbitrarily small by collecting more photons and reducing the noise factors. By employing highly performing fluorophores or fluorescent particles, high numerical aperture objectives, extremely sensitive cameras such as Electron Multiplying CCD cameras capable of single-photon detection, and by minimizing the out-of-focus fluorescence background through careful illumination design (see chapter 3), it is possible to determine the position of single, isolated fluorescent emitters with an uncertainty of a few nanometers[19].

The possibility to localize a single fluorescence emitter with nanometer precision was first exploited by Yildiz and Selvin, who named this technique FIONA (Fluorescence Imaging with One Nanometer Accuracy), to unravel the walking mechanism of myosin V[20], myosin VI[21] and kinesin[22] between 2003 and 2004¹⁹. By labelling these molecular motors with very bright fluorophores they could accurately localize and track their movements along actin and microtubules for the first time.

2 Localization-based super-resolution microscopy: PALM and STORM

FIONA was developed with single-molecule tracking in mind. While in principle it could also be used to localize the position of individual molecules making up larger structures, there was the fundamental problem that two fluorophores closer than the diffraction limit would be unresolvable, as explained in section 1.1. Indeed, FIONA requires non-overlapping PSFs in order to determine the position of individual emitters.

In 2006, two independent groups came up with techniques to overcome this limitation, applying single-molecule localization to the imaging of labelled structures inside cells. PhotoActivated Localization Microscopy (PALM)[23] and STochastic Optical Reconstruction Microscopy (STORM)[24] both rely on the FIONA principle but they extend it to the entirety of the fluorescence emitters in densely labelled samples. The end result of both techniques is a super-resolved image in the form of a “map” of individual localizations, which can achieve effective resolutions up to a few tens of nanometers.

The solution to the overcrowding problem relies on the complex temporal behavior of the fluorescence emission of several fluorescent molecules, which can be exploited to have many close-by fluorophores emit light at different times. By leveraging on the peculiar photochemistry of these molecules, it is possible to have just a small fraction of a densely packed population of dyes emit fluorescence at any given time (Figure 6). If the individual emitters are far apart enough to be distinguishable (i.e.: a maximum of one emitter per PSF area is in a fluorescent state), they can be localized with great precision by fitting their emission pattern with a two-dimensional Gaussian. This process can be repeated many times, every time recording the signal coming from a different subset of emitters, until a sufficient number of fluorescent molecules in the image have been localized and the labelled structure is properly sampled (see section 2.2).

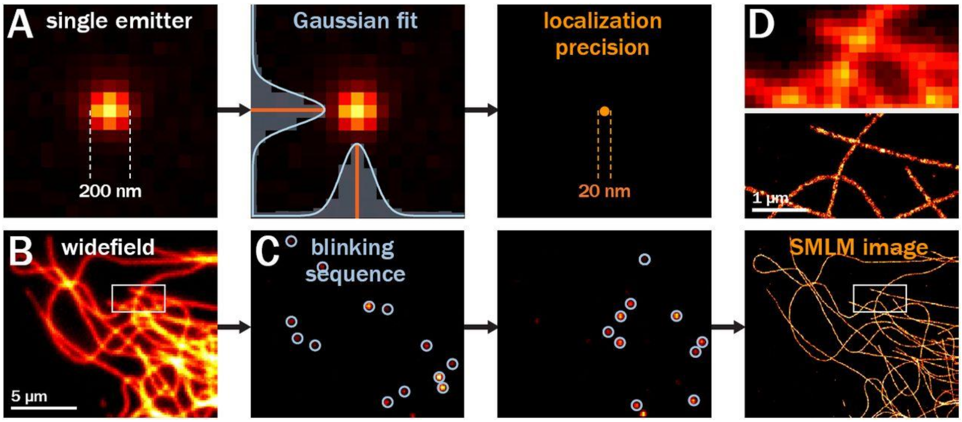

Figure 6. A. Epifluorescence image of a single emitter, showing the ~200 nm width of the PSF (left) that is fitted using Gaussian curves (center) to determine its position with a ~20 nm precision (right). B. Epifluorescence image of microtubules. C. During SMLM acquisition, a blinking mode of fluorescence emission is induced and thousands of frames are recorded, containing individual blinking events that can be fitted to localize each emitter. D. After processing, all localizations are plotted to generate the SMLM images (bottom). Top panel is a zoom corresponding to the box highlighted in the full image and shows the gain in resolution (top). Image and caption retrieved from [25].

The differences between PALM and STORM are subtle, and can be traced to the way in which they first implemented the same principle. PALM was demonstrated on photoactivatable fluorescent proteins such as PAmCherry[26,27], which would be expressed in a non-fluorescent form by the host organism and then converted into a fluorescent state upon "activation" with a specific wavelength, which is different from the one used to excite fluorescence. This conversion generally involves some irreversible change in the chemical structure of the proto-fluorophore. The intensity of this activation wavelength and the duration of the exposure would determine the amount of photoconverted proteins at any given time. The photoactivation mechanism of PAmCherry1 is shown in Figure 7. STORM, on the other hand, relied on synthetic chemical dyes exhibiting photoswitching properties (i.e., they can be reversibly switched multiple times between a fluorescent and a non-fluorescent state) such as the cyanine dye Cy5. In the early years of STORM, there was no known method to convert photoswitchable reporter dyes such as Cy5 back to their native fluorescent configuration after being deactivated, and it was necessary to link them to a secondary "activator" dye, such as the cyanine Cy3, in order to create a proper reversible switch. In the following years, reactivation of individual photoswitchable cyanine dyes via irradiation with a secondary wavelength was reported[28], and several other molecules have been characterized that exhibit spontaneous, stochastic fluctuations between fluorescent and non-fluorescent states, which made it possible to employ them as standalone photoswitchable dyes (Figure 8). The reversible photoswitching mechanism of STORM employing standalone photoswitchable dyes has been dubbed "direct-STORM" or "dSTORM"[29].

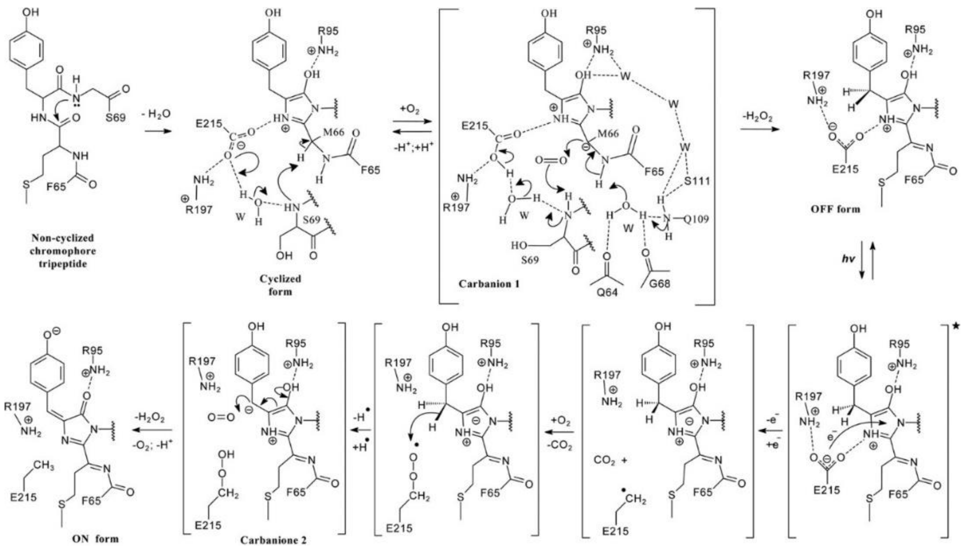

Figure 7. Suggested mechanisms for the formation of the PAmCherry1 dark chromophore (OFF state) and its light-induced conversion into the fluorescent state (ON state) are shown. The cyclized form is the chromophore with the non-oxidized bond between p-hydroxyphenyl and imidazolone moieties and without N-acylimine. Hydrogen bonds are shown with dashed lines. Intermediate compounds are shown in parentheses. The chromophore in the excited state is

denoted with asterisk. hv, indicates the illumination with violet light. Migration of the electron density is shown with curved arrows. Image and caption retrieved from [30].

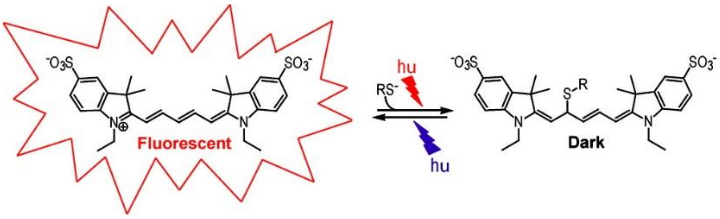

Figure 8. Photoswitching mechanism of the cyanine dye Cy5. A thiolate anion (RS^-) can bind reversibly to the dye upon fluorescence excitation, converting it into a dark state. Detachment of the thiol group can be triggered by irradiation with violet light. Image retrieved from [28].

2.1 Building the image

The raw output of a PALM/STORM experiment is a stack of consecutive images taken from the same field of view. In each of these images only a small fraction of the underlying fluorophores is visible, appearing as a sparse “constellation” of bright spots (Figure 9). These images are then processed by dedicated image analysis software and individual fluorophores are localized (see section 2.2.2).

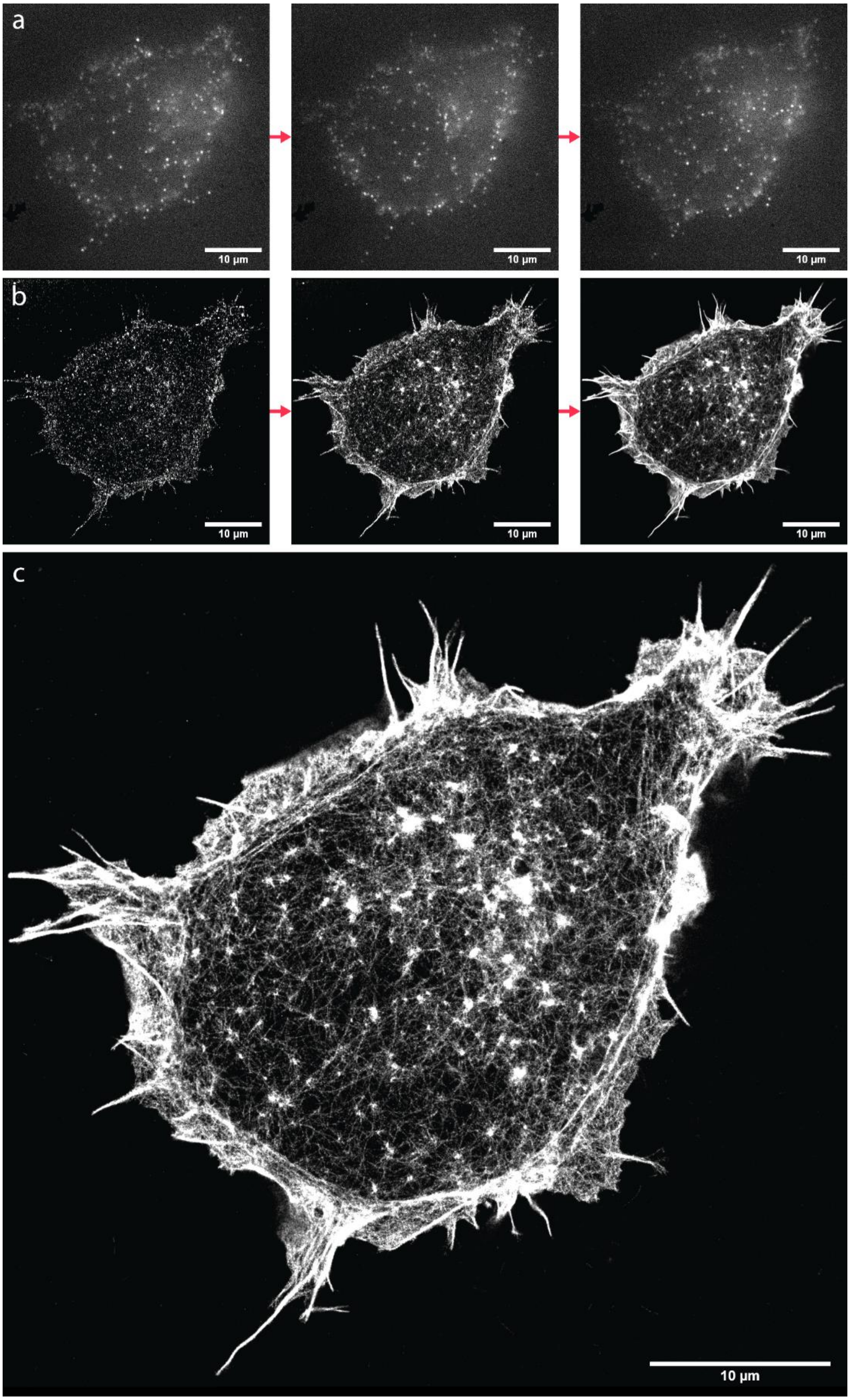
a
10 µm
10 µm
10 µm
b
10 µm
10 µm
10 µm
c
10 µm

Figure 9. Numerous images are acquired during a PALM/STORM experiment, each containing the PSFs generated by sparse fluorescent molecules. The position of the individual molecules in each frame is determined with sub-diffraction accuracy, and the resulting spatial coordinates are superimposed to create a super-resolved image. (a) Raw blinking sequence of Alexa Fluor 647 labelling the actin cytoskeleton of a HEK 293 cell. (b) Progressive reconstruction of a super-resolution image. From left to right: STORM image obtained after processing the first 100 frames of the raw movie, STORM image obtained after processing the first 1,000 frames, and final image obtained after processing all of the 30,000 frames of the movie. (c) Larger version of the fully reconstructed image.

The amount of frames necessary to map the sample sufficiently is strongly dependent on the nature of the underlying structure and on the labelling density (see section 2.2). A PALM/STORM movie can range from a few hundred frames in length for imaging very sparse proteins, to around 100,000 frames in the case of abundant and densely packed structures such as cytoskeletal networks. As such, the acquisition time for a PALM/STORM movie can range from a few seconds to more than an hour, limiting the imaging of dense and complex structures to non-living, chemically fixed samples. Recently though, large improvements in image analysis software regarding the localization of multiple close-by emitters[31] are allowing researchers to successfully perform PALM/STORM in high-density labelling conditions, in which a much higher concentrations of active fluorophores per frame are imaged. These new developments can drastically reduce the amount of frames required to accurately reconstruct an image, allowing for faster acquisition and potentially making localization-based super-resolution techniques viable for live-cell imaging.

In the next sections, the experimental procedure to perform a PALM/STORM experiment is described in detail, from sample preparation to image acquisition and final image reconstruction.

In any case, a crucial aspect of performing a PALM/STORM experiment lies in controlling the amount of active fluorophores during the acquisition. There are many different ways to go about this, which depend mostly on the photochemical behavior of the fluorophore being used. Typically, the photoactivatable fluorescent proteins used in PALM are non-fluorescent in their native state[32]. As such, the rate of photoactivation determines the amount of active fluorophores in each frame. Since these proteins are switched to their fluorescent state by irradiation with a specific wavelength, the rate of photoactivation can be controlled by modulating the intensity of the activating light[23]. The mechanism is generally different and more complex in the case of STORM photoswitchable dyes. This, along with important considerations about the optimal density of active fluorophores during a PALM/STORM image acquisition, is discussed in detail in section 2.2.

2.1.1 dSTORM imaging procedure

In this section I will describe the imaging procedure for a typical dSTORM experiment performed in our lab. The dyes of choice are generally Alexa Fluor dyes (more specifically, Alexa Fluor 488 or Alexa Fluor 647), which are a family of photoswitchable fluorophores with excellent brightness and photostability.

As illustrated in Figure 10, Alexa Fluor dyes can switch from a fluorescence-emitting ON-state to a non-fluorescent triplet state via intersystem crossing upon excitation. At this point, the triplet state can either switch back to the singlet ground state or react with a thiolate to form a non-fluorescent radical anion. This dark state can then be oxidized, which returns it to the singlet ground state, or form a thiol adduct which is a longer-lived non-fluorescent species. As such, Alexa Fluor dyes require both the presence of a thiol and lack of oxygen in the medium in order to stably switch into their non-fluorescent forms.

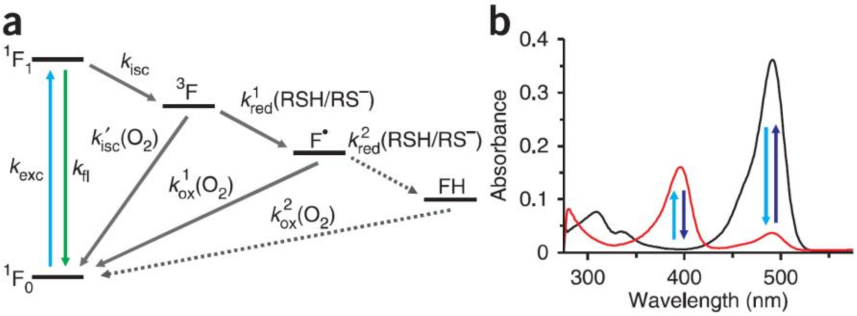

Figure 10. Reversible photoswitching of Alexa Fluor and ATTO dyes in the presence of thiols. (a) The fluorophore is either cycled between its singlet ground and excited state emitting fluorescence photons or can undergo intersystem crossing with rate k_{isc} upon irradiation. The triplet state (^3F) can react with molecular oxygen to recover the singlet ground state and produce singlet oxygen or react with the thiolate with rate k_{red} to form the radical anion of the fluorophore (F^*) and the corresponding thiyl radical. The radical anion can be oxidized by oxygen with rate k_{ox} to recoverthe singlet ground state. Because radical anions of most rhodamine and oxazine derivatives show pronounced absorption at ~400 nm irradiation, for example, at 405 nm promotes recovery of the fluorescent form (i.e., OFF- and ON-switching are photoinduced). Whereas the thiyl radicals formed react efficiently with molecular oxygen to produce superoxide radicals and hydrogen peroxides, the fluorophore radical anion is very unreactive and survives for up to several seconds even in the presence of molecular oxygen. Fluorophores such as ATTO 655 and ATTO 680 accept a second electron to the fully reduced leuco-form (FH). Oxidation of FH with oxygen also recovers the ON state. (b) Absorption spectra of Alexa Fluor 488 in PBS (pH 9.3) in the presence of 100 mM MEA. After irradiation at 488 nm (light blue), the absorption at 488 nm decreases and the radical anion absorbing maximally around 400 nm appears. The fluorescent state is recovered spontaneously or by direct excitation of the radical anion at ~400 nm (dark blue). The stability (lifetime) of the radical anion is mainly determined by the oxygen concentration and can easily exceed several hours[33]. Image and caption retrieved from [34].

The imaging buffer that we commonly use for dSTORM involving Alexa Fluor dyes is a slight variation on the OxEA buffer developed by Nahidiazar *et al.*[35]. It features β-Mercaptoethylamine (MEA) as a reducing thiol and an oxygen scavenging system in the form of Oxyrase, an enzyme system derived from a membrane fraction of *E. coli* which selectively captures oxygen and reduces it to water by having it react with lactic acid. The exact composition of this buffer is reported in appendix 7.

The fluorescently labelled sample, which was grown on a round glass coverslip (the protocol for the growth and preparation of cells for STORM microscopy is reported in appendix 7), is placed inside of a steel imaging chamber with an open ceiling, as the one shown in Figure 11. The buffer is added directly into the chamber. The chamber is mounted on the microscope immediately after adding the imaging buffer.

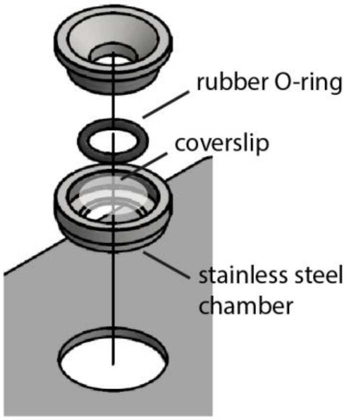

Figure 11. Imaging chamber schematics. Image retrieved from [36].

Imaging is performed in the following way:

- The sample is explored with bright field illumination and no electron-multiplying (EM) gain on the EMCCD camera until a suitable field of view is found.
- A diffraction-limited fluorescence reference image is acquired by illuminating the sample with a very low laser intensity (~10 W/cm^2, with an excitation wavelength of 488 nm for Alexa Fluor 488 or 640 nm for Alexa Fluor 647), filtering the fluorescence signal with a suitable bandpass filter (530/43 nm for Alexa Fluor 488 or 680/42 nm for Alexa Fluor 647) and recording with a camera integration time of around 40 ms. Typically no EM gain is needed at this point due to the very high labelling density used in STORM experiments which leads to elevated fluorescence signals.
- Most of the fluorophores are switched in a dark state by bringing up the power of the excitation laser (>1 kW/cm^2) which leads to a steady blinking of Alexa Fluor dyes after a few seconds.
- While keeping the same excitation laser power, the EM gain of the camera is brought up to 400 and images are taken with an integration time of 40 ms. Up to 100,000 frames can be acquired through direct spooling of the images on a solid-state drive (SSD). The actual length of the video depends on the nature of the sample being imaged.
- Optional: during acquisition, if blinking events are becoming excessively sparse, the sample can be irradiated with a low-intensity 405 nm light in order to speed up fluorophore recovery to the fluorescent state and increase the amount of visible spots per frame.

2.2 Sampling the structure: labelling density and Nyquist criterion

Reconstructing the architecture of a microscopic object by acquiring the coordinates of individual component molecules is akin to digitizing an analog signal; as such, the maximum resolution of a reconstructed image is equal to approximately twice the average distance between neighboring probes in accordance to the Nyquist-Shannon sampling theorem[37–39]. If the fluorescent labelling density of a specimen is insufficient, the resulting image will be undersampled and the finer details will be lost (Figure 12).

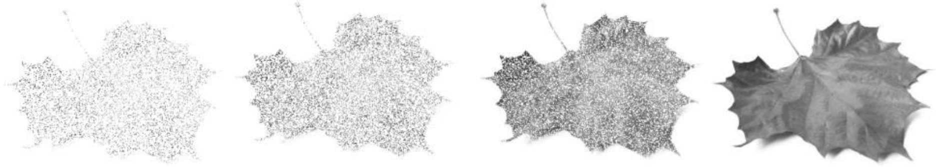

Figure 12. The first image on the left is composed of a sparse set of localization points, representing a low degree of molecular density in a virtual specimen. Increasing the number of localized molecules increases the resolution of the image as well. At the highest molecular density, fine specimen details become apparent. Image reworked from [40].

Therefore, if the optical resolution (i.e. the localization uncertainty on individual fluorophores) of a certain optical system is 20 nanometers in two dimensions, an equal image resolution can only be achieved if the labelling density of the specimen is such that neighboring fluorophores are separated by 10 nanometers or less. This would result in extremely high molecular densities of around 10,000 molecules per square micron, which means that at the Nyquist molecular density around 600 fluorophores are located within the lateral projection of a typical PSF with a diameter of ~250 nm. So many molecules in a diffraction-limited space can make it extremely difficult to perform accurate single-molecule localization imaging. This means that the density of actively emitting fluorophores must be finely tuned in order to have a maximum of one single active emitter within a PSF area at any given time.

More generally the image resolution in PALM/STORM experiments is dependent on two main parameters: (i) the amount of photons emitted per switching event, also called the "photon yield", which determines the localization precision (as discussed in section 1.2), and (ii) the "duty cycle", i.e.: the fraction of time that a probe spends in the fluorescent "on" state compared to the nonfluorescent "dark" state.

While the connection between photon yield and image resolution is straightforward, the duty cycle relates to the Nyquist molecular density mentioned before. As a high amount of fluorophores is located within a diffraction-limited spot, it is crucial that they spend the vast majority of their time in the "dark" state during imaging, so that only one single probe is emitting fluorescence at any given time. As such, a fluorophore with a duty cycle of 1/N can only allow less than N molecules to be localized within a PSF-delimited area. At Nyquist molecular density regimes, only dyes with a duty cycle of less than ~1/600 are viable for STORM imaging. The duty cycle of a given probe is the product of both the intrinsic chemical structure of the fluorophore and its environment, and it can be modified to an extent by acting on the latter (i.e. the imaging buffer).

Figure 13 shows the effects of different photon yields and duty cycles on a sample STORM image reconstruction.

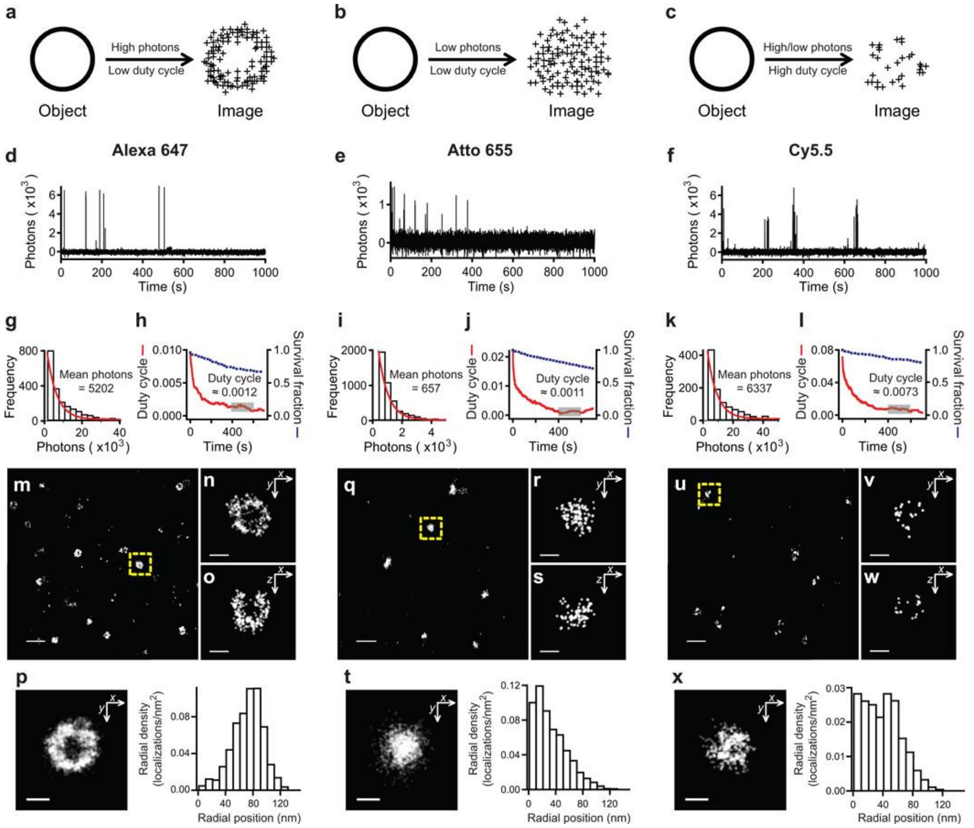

Figure 13. (a–c) The effect of number of detected photons per on-switching event and the on/off duty cycle (fraction of time in the on state) on STORM image quality for an example structure (a ring-like object). (a) A fluorophore with high photon number and low duty cycle produces a hollow, ring-like image with high localization precision and sufficient density. (b) A fluorophore with low photon number and low duty cycle maintains a large number of localizations, but suffers reduced localization accuracy, obscuring the ring-like structure. (c) A fluorophore with high on/off duty cycle requires reduction in the density of fluorescent probes to allow single-molecule localization, which in turn reduces the number of localizations and adversely affects the overall resolution. Single-molecule fluorescence time traces measured in the presence of βME and an oxygen scavenging system, as shown for three red-absorbing dyes (d) Alexa 647, (e) Atto 655, and (f) Cy5.5. Each of these dyes represents one of the scenarios described in (a–c). From these traces, the number of detected photons was determined for each switching event and a histogram was constructed from many events from hundreds of molecules (g,i,k). The indicated mean value was derived from the single exponential fit of the distribution (red curve). The on/off duty cycle value was calculated for each dye and plotted versus time (red curve; h,j,l) to show how each value begins high when most molecules are in the fluorescent state and reaches a quasi-equilibrium at a later time. The reported values are the average duty cycle measured between 400–600 sec (gray box). The fraction of molecules that survived

photobleaching was plotted together with the duty cycle (blue squares). Images of clathrin-coated pits (CCPs) in 3D using the three dyes. (m–p) Alexa 647, (q–t) Atto 655, and (u–x) Cy5.5. The large fields of view shown in (m,q,u) are 2D projection images. The images of the CCPs indicated by the yellow dashed boxes are magnified and their xy cross-sections (n,r,v) and xz cross-sections (o,s,w) are shown. The composite xy cross-sections for ten CCPs aligned to their respective centers of mass are shown along with the radial density distributions of localizations derived from the composite xy cross-sections (p,t,x). Scale bars are 500 nm for (m,q,u) and 100 nm for (n–p, r–t, v–x). Image and caption retrieved from [37].

As mentioned in section 2.1.1, the commonly used dye Alexa Fluor 647 requires the presence of a thiol and a low concentration of oxygen to maintain a long-lived "dark" state upon fluorescence emission. This requirement is common to many widely used fluorophores; as such, imaging buffers containing an oxygen scavenging system and some form of thiol – generally β-mercaptoethanol (βME) or mercaptoethylamine (MEA) – are employed to lower the duty cycle of photoswitchable probes, albeit a fine tuning of the buffer composition is required for different dyes. An overview of the properties and the photoswitching performance of many dyes in different imaging buffers can be found in Figure 14.

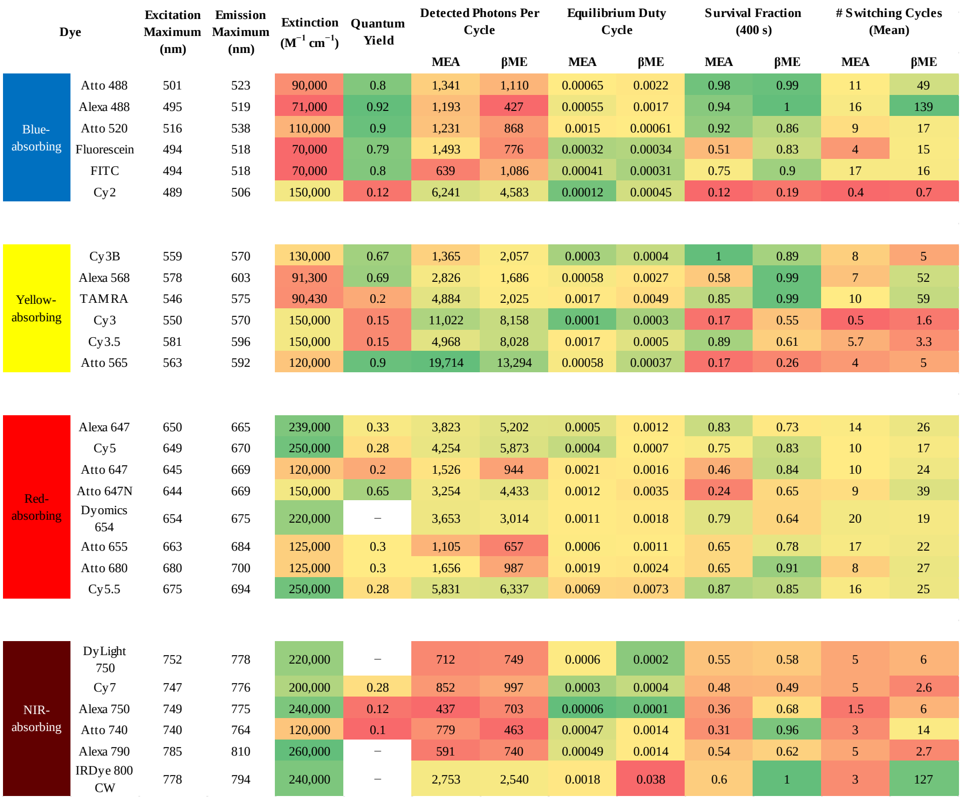

Dye		Excitation Maximum (nm)	Emission Maximum (nm)	Extinction (M^{-1} cm^{-1})	Quantum Yield	Detected Photons Per Cycle		Equilibrium Duty Cycle		Survival Fraction (400 s)		# Switching Cycles (Mean)	
						MEA	βME	MEA	βME	MEA	βME	MEA	βME
Blue-absorbing	Atto 488	501	523	90,000	0.8	1,341	1,110	0.00065	0.0022	0.98	0.99	11	49
	Alexa 488	495	519	71,000	0.92	1,193	427	0.00055	0.0017	0.94	1	16	139
	Atto 520	516	538	110,000	0.9	1,231	868	0.0015	0.00061	0.92	0.86	9	17
	Fluorescein	494	518	70,000	0.79	1,493	776	0.00032	0.00034	0.51	0.83	4	15
	FITC	494	518	70,000	0.8	639	1,086	0.00041	0.00031	0.75	0.9	17	16
	Cy2	489	506	150,000	0.12	6,241	4,583	0.00012	0.00045	0.12	0.19	0.4	0.7
Yellow-absorbing	Cy3B	559	570	130,000	0.67	1,365	2,057	0.0003	0.0004	1	0.89	8	5
	Alexa 568	578	603	91,300	0.69	2,826	1,686	0.00058	0.0027	0.58	0.99	7	52
	TAMRA	546	575	90,430	0.2	4,884	2,025	0.0017	0.0049	0.85	0.99	10	59
	Cy3	550	570	150,000	0.15	11,022	8,158	0.0001	0.0003	0.17	0.55	0.5	1.6
	Cy3.5	581	596	150,000	0.15	4,968	8,028	0.0017	0.0005	0.89	0.61	5.7	3.3
	Atto 565	563	592	120,000	0.9	19,714	13,294	0.00058	0.00037	0.17	0.26	4	5
Red-absorbing	Alexa 647	650	665	239,000	0.33	3,823	5,202	0.0005	0.0012	0.83	0.73	14	26
	Cy5	649	670	250,000	0.28	4,254	5,873	0.0004	0.0007	0.75	0.83	10	17
	Atto 647	645	669	120,000	0.2	1,526	944	0.0021	0.0016	0.46	0.84	10	24
	Atto 647N	644	669	150,000	0.65	3,254	4,433	0.0012	0.0035	0.24	0.65	9	39
	Dyomics 654	654	675	220,000	–	3,653	3,014	0.0011	0.0018	0.79	0.64	20	19
	Atto 655	663	684	125,000	0.3	1,105	657	0.0006	0.0011	0.65	0.78	17	22
	Atto 680	680	700	125,000	0.3	1,656	987	0.0019	0.0024	0.65	0.91	8	27
	Cy5.5	675	694	250,000	0.28	5,831	6,337	0.0069	0.0073	0.87	0.85	16	25
NIR-absorbing	DyLight 750	752	778	220,000	–	712	749	0.0006	0.0002	0.55	0.58	5	6
	Cy7	747	776	200,000	0.28	852	997	0.0003	0.0004	0.48	0.49	5	2.6
	Alexa 750	749	775	240,000	0.12	437	703	0.00006	0.0001	0.36	0.68	1.5	6
	Atto 740	740	764	120,000	0.1	779	463	0.00047	0.0014	0.31	0.96	3	14
	Alexa 790	785	810	260,000	–	591	740	0.00049	0.0014	0.54	0.62	5	2.7
	IRDye 800 CW	778	794	240,000	–	2,753	2,540	0.0018	0.038	0.6	1	3	127

Figure 14. Tabulated dye switching properties include: number of detected photons per switching event; equilibrium on-off duty cycle taken between 400 and 600 seconds of sustained laser illumination; the survival fraction after illumination for 400 seconds; and the number of switching cycles. The dye switching properties are reported in the presence of a glucose oxidase-based oxygen scavenging buffer (GLOX) and 10 mM MEA as well as GLOX and 140 mM βME. Also included are additional dye properties: excitation and emission peak wavelengths from the dye spectra; extinction coefficients from the dye manufacturers; and quantum yields from either the dye manufacturer when known or from the McNamara 2007 fluorophore data tables. Color-coded from most desirable (green) to least desirable (red) in SMLM imaging. Table and caption retrieved and reworked from [37].

From what has been explained so far, it would appear that an optimal fluorophore duty cycle exists for any given sample, that it ultimately depends on the molecular density of the probe being imaged and that it can be obtained simply with an appropriate combination of fluorescent dye and imaging buffer. However, when we take into account the phenomenon of photobleaching, this ceases to be true. During the course of sustained imaging, the photoswitchable probes will gradually convert irreversibly to a non-fluorescent state, in a process known as "bleaching”. This lowers the probe molecular density over time, which in turn decreases the information content in the individual frames of a STORM movie. In order to maintain an optimal number of emitting fluorophores per frame, the duty cycle of the probes needs to increase over time. For many molecules (especially red-emitting dyes[37]), this can be achieved by irradiating the sample with an “activation” laser at a shorter wavelength than the excitation laser, typically in the violet or ultraviolet range. This process effectively increases the speed at which molecules convert from the long-lived “dark” state back to the fluorescent ground state. Figure 15Figure 15 shows the varying sensitivity to violet photoactivation of many different dyes.

	Dye	Sensitivity to activation by violet light
Blue-absorbing	Atto 488	+
	Alexa 488	+
	Atto 520	+
	fluorescein	–
	FITC	–
	Cy2	–
Yellow-absorbing	Cy3B	+
	Alexa 568	+
	TAMRA	–
	Cy3	–
	Cy3.5	+
	Atto 565	+
Red-absorbing	Alexa 647	++
	Cy5	++
	Atto 647	+
	Atto 647N	+
	Dyomics 654	++
	Atto 655	+
	Atto 680	+
	Cy5.5	++
NIR-absorbing	Dylight 750	++
	Cy7	++
	Alexa 750	++
	Atto 740	+
	Alexa 790	++
	IRDye 800CW	++

Figure 15. The fraction of single fluorescent molecules that activate after a 0.25 seconds pulse of 405 nm excitation light (10–30 W/cm²) relative to the total initial population for each dye. Dyes were assigned a "–", "+", or "++" if <3%, 3–25%, or >25% are reactivated, respectively. Table and caption retrieved from [37].

2.2.1 Preparation of mammalian cell samples

When preparing biological samples for STORM imaging, the most important issue to consider is that of the acquisition time of a STORM movie. Depending on the structure being imaged, the fluorophore being used and the acquisition speed of the camera, a single acquisition can take between a few seconds and more than an hour to complete. With the possible exception of imaging very sparse cellular structures, the acquisition times associated with STORM are typically incompatible with having live cells under the microscope, as the sample would move significantly during the course of the measurement and the image resolution would be negatively affected. Some major strides have been recently made towards live-cell STORM imaging by adopting so-called "high-density localization" approaches[31,41,42], in which advanced image processing algorithms are employed to accurately localize overlapping PSFs, considerably speeding up movie acquisition; however, the standard practice remains that of chemically fixing biological samples prior to imaging. Typically, formaldehyde fixation is the method of choice as it results in cross-linking of primary amino groups of neighboring proteins, which preserves the architecture of cellular structures (especially the cytoskeleton).

Another issue to consider when preparing STORM samples is whether the molecular target we are interested in labelling is intracellular or extracellular. As most fluorescent probes are conjugated to large molecules such as antibodies or toxins in order to specifically bind to their target, they are not able to diffuse through an intact plasma membrane; therefore, permeabilization of the lipid bilayer with a surfactant is necessary when labelling an intracellular structure.

A detailed protocol for the growth and labelling of cells for STORM imaging of the actin cytoskeleton is reported in appendix 7.

2.2.2 Reconstruction of a super-resolved image

After acquiring a raw dataset from a STORM experiment, the resulting images need to be processed in order to determine the position of individual fluorescent molecules. One of the most largely used computational tools to perform this task is ThunderSTORM[43], an open-source plugin for the image processing program ImageJ[44,45] which features a variety of different algorithms for the processing, analysis and visualization of data acquired through PALM/STORM or other SMLM methods. ThunderSTORM accepts a sequence of raw images containing sparse PSFs as input, and reconstructs a super-resolution image with the following workflow:

- First, the approximate positions of the molecules in an image are determined by finding local intensity maxima, in combination with a variety of possible image filtering methods. It is also possible to specify a threshold for the intensity of localized maxima by using a mathematical expression with parameters based on the image being processed, which allows to systematically calculate an optimal threshold for each frame and for different datasets.
- Nanometer-level localization of molecules is then performed by fitting the PSF model of choice on the previously identified intensity maxima. The uncertainty on the localization for each molecule is calculated either according to Thompson *et al.* (section 1.2) or by using a variation on the same formula by Quan *et al.*[46] which takes into account the effects of signal amplification by EMCCD cameras. The parameters used for filtering, finding intensity peaks and PSF fitting in a typical STORM experiment involving Alexa Fluor 488 or Alexa Fluor 647 are shown in Figure 16.
- The previous step generates a set of sub-diffraction molecular coordinates, that can then be rendered into a super-resolution image by displaying each molecule as a two-dimensional Gaussian with a standard deviation corresponding to their respective localization uncertainty. A number of other less computationally intensive rendering options are also available. The difference between a Gaussian rendering and other rendering methods is shown in Figure 17.
- The output of a ThunderSTORM analysis consists in a table (a .csv file) which contains a series of other parameters associated to each localized molecule: the frame in which it was localized, the x and y coordinates expressed in nanometers, the standard deviation of the

fitted Gaussian function (in nanometers), the peak intensity (in photons), the offset (in photons), the standard deviation of the background intensity (in photons) and finally the localization uncertainty (in nanometers) calculated with Equation 2.

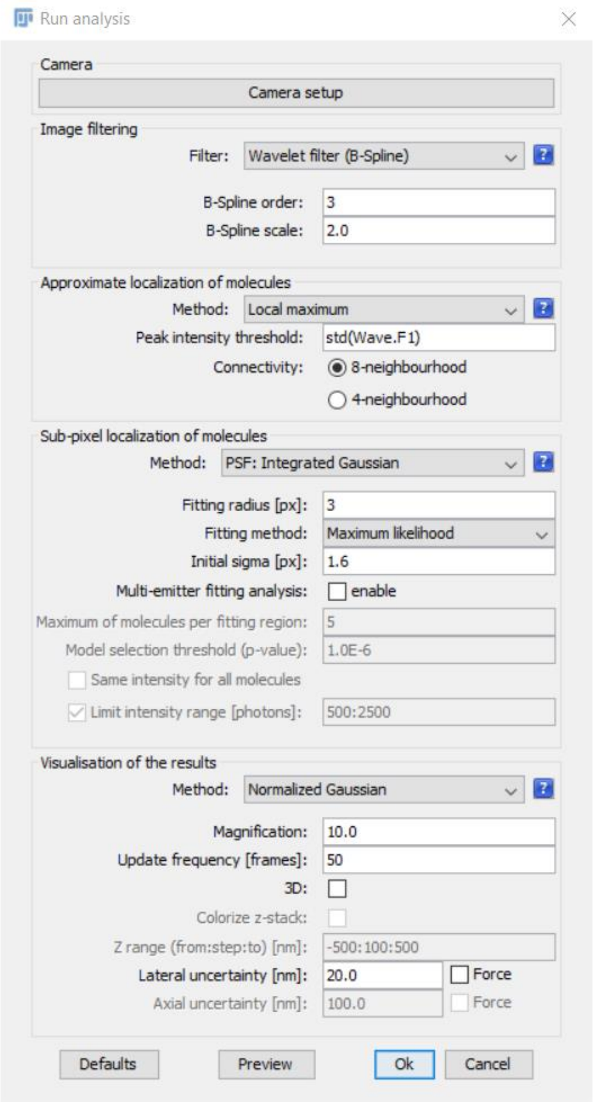

Filter: Wavelet filter (B-Spline)
B-Spline order: 3
B-Spline scale: 2.0

Method: Local maximum
Peak intensity threshold: std(Wave.F1)
Connectivity: ● 8-neighbourhood ○ 4-neighbourhood

Method: PSF: Integrated Gaussian
Fitting radius [px]: 3
Fitting method: Maximum likelihood
Initial sigma [px]: 1.6
Multi-emitter fitting analysis: ☐ enable
Maximum of molecules per fitting region: 5
Model selection threshold (p-value): 1.0E-6
☐ Same intensity for all molecules
☑ Limit intensity range [photons]: 500:2500

Method: Normalized Gaussian
Magnification: 10.0
Update frequency [frames]: 50
3D: ☐
Colorize z-stack: ☐
Z range (from:step:to) [nm]: -500:100:500
Lateral uncertainty [nm]: 20.0 ☐ Force
Axial uncertainty [nm]: 100.0 ☐ Force

Figure 16. ThunderSTORM UI showing the parameters used for the reconstruction of a typical STORM image acquired from a specimen labelled with Alexa Fluor 647 or Alexa Fluor 488.

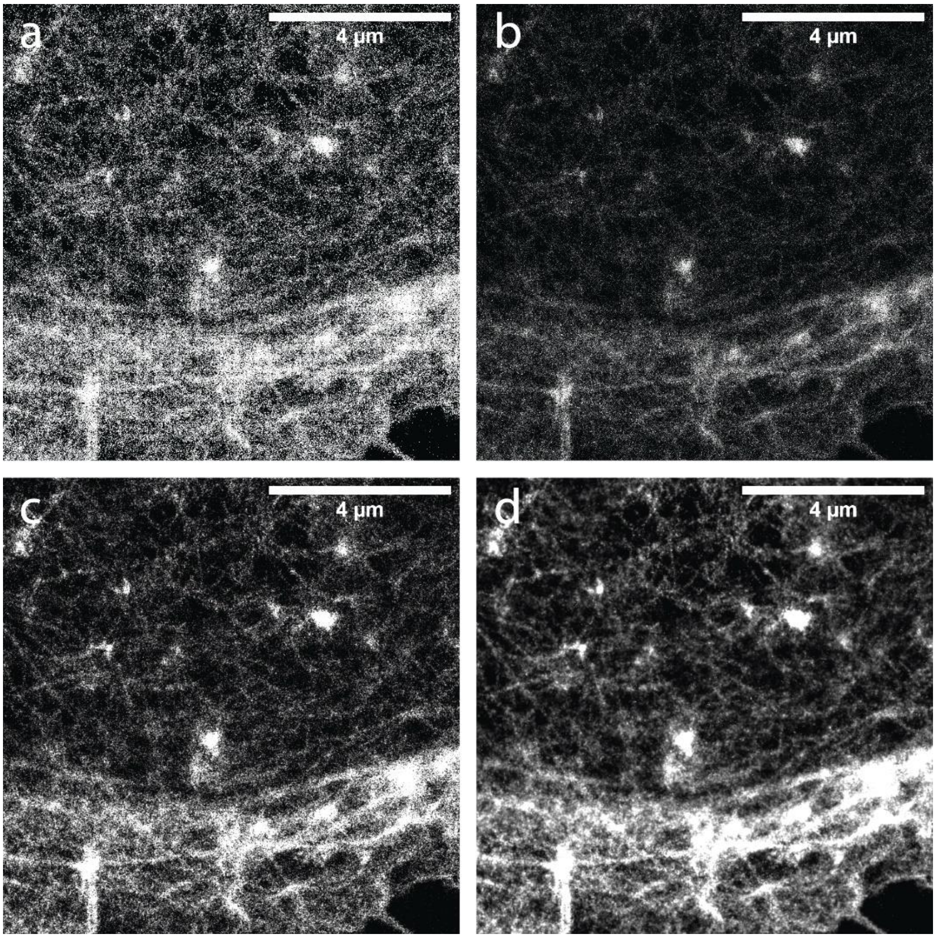

Figure 17. Detail of a reconstructed STORM image of the actin cytoskeleton of a HEK 293 cell displayed by ThunderSTORM with different rendering systems. (a) scatter plot; (b) histograms; (c) average shifted histograms; (d) normalized Gaussian. The Gaussian rendering produces an image in which each spot is a 2D Gaussian whose standard deviation corresponds to the localization uncertainty on the respective molecule, and whose peak corresponds to its fluorescence intensity.

3 Optical techniques to reduce the background fluorescence

As previously introduced in section 1.2, precisely localizing single fluorescent molecules is no easy task. Having single-photon detection capabilities means that background noise can become a serious hindrance, partially masking or completely covering the signal coming from isolated fluorophores and resulting, in the case of a PALM/STORM image, in fewer localizations (incomplete sampling) and in a lower localization precision according to Thompson's formula (Equation 2). As such, limiting the fluorescence coming from out-of-focus planes is of crucial importance. Since all SMLM techniques are fundamentally widefield microscopy techniques (which is necessary to speed up data acquisition to reasonable levels), there is no inherent optical sectioning given by pinholes or focused illumination; the only means to limit out-of-focus fluorescence is therefore to act on the pattern of excitation light, in order to limit the excited sample volume as much as possible along the z axis while keeping it centered on the focal plane of the objective. One of the most effective ways to achieve this excitation confinement is to use Total Internal Reflection Fluorescence (TIRF) illumination. By focusing a beam on the back focal plane of a high-numerical aperture objective along an axis which is parallel to the optical axis, but shifted sideways from the centre by a distance d, the beam comes out of the objective collimated and inclined by an angle θ_i (Figure 18). If this angle is higher than the critical angle at which total internal reflection occurs at the interface between glass (coverslip) and water (sample), then the beam is entirely reflected back and an evanescent wave is formed at the glass-water interface. The intensity of this evanescent wave decays exponentially within around 200 nm from the interface, which practically limits the excitation volume to the section of the sample in immediate contact with the coverslip surface. By avoiding out-of-focus fluorescence entirely, this technique has allowed for incredibly clear single-molecule images of cellular membrane structures[47]. But its strong point is also its biggest limitation, as it is impossible to image anything farther away than 200 nm from the coverslip by using TIRF. A good compromise between TIRF and epifluorescence illumination comes from so-called "Highly Inclined and Laminated Optical sheet" (HILO)[48]. By employing the same optical configuration used with

TIRF while limiting the angle θ_i to a lower value than the critical angle, the beam is not reflected back towards the objective but it is refracted along an axis, entering the sample as a collimated thin sheet of light with an inclination of θ_r at the interface between the coverslip and the sample (Figure 18) according to Snell's law:

$$n_i \sin \theta_i = n_r \sin \theta_r$$

Equation 3

$$\theta_r = \sin^{-1} \frac{n_i \sin \theta_i}{n_r}$$

Equation 4

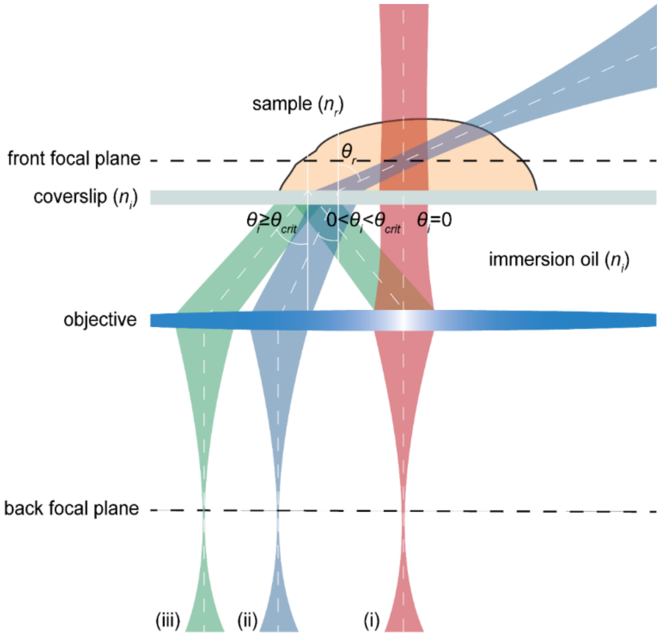

Figure 18. Schematic representation of (i) epifluorescence illumination, (ii) HILO and (iii) TIRF. When the angle θ_i at which the beam impacts with the glass/water interface is 0, the beam traverses the sample along the optical axis and the system is in an epifluorescence configuration. When θ_i reaches the critical angle θ_r, the beam is reflected entirely back towards the objective and the system is in TIRF configuration. For intermediate values of θ_i, the beam traverses the sample at an angle θ_r with respect to the optical axis and the system is in HILO configuration.

For geometrical optics approximation, the thickness of the light sheet dz along the z direction is roughly $dz = R/\tan\theta_r$, where R is the diameter of the illuminated area on the front focal plane of the objective (Figure 19). A very convenient feature of HILO illumination is also that, if properly aligned, the inclined light sheet will always cross the optical axis of the objective while being centered on the focal plane, thus illuminating the center of the field of view irrespectively of the position along z. The reduced thickness and the inclination of the optical sheet can limit the excitation volume to a "slice" of sample only a few microns thick, allowing for largely reduced background fluorescence and much higher contrast compared to epifluorescence illumination, while retaining the ability to image in depth along the z axis.

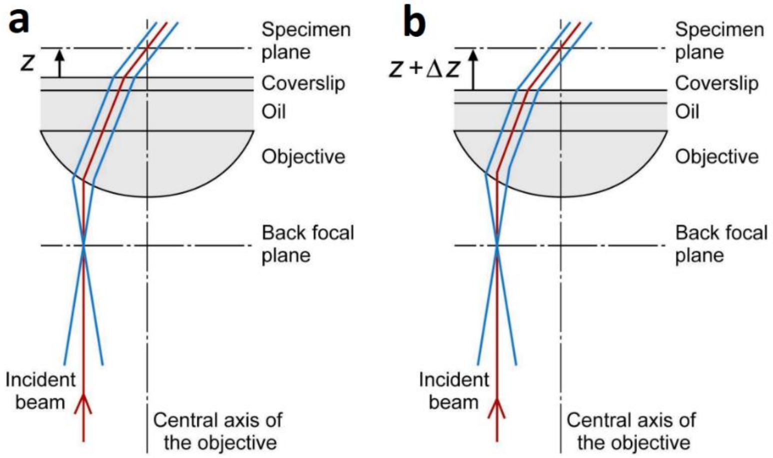

Figure 19. Beam paths of HILO microscopy before (a) and after (b) a z-directional shift of the objective. A beam parallel to the central axis of the objective (red line) passes through the center of the specimen plane [ed, the focal plane]. A beam focused at the back focal plane (blue line) becomes parallel at the specimen plane. In HILO, the illumination beam always passes through the center of the specimen plane, which means the illumination beam follow the z-directional shift of the specimen plane. Image and caption retrieved from [48].

3.1 Characterizing and optimizing the inclined illumination profile

Starting from the previous consideration that HILO illumination represents the current state-of-the-art for SMLM in relatively thick samples, we set forth on thoroughly characterizing this technique in order to identify crucial parameters that enable high-quality fluorescence microscopy (especially SMLM) by directly measuring the inclined light sheet profile within aqueous samples for the first time. We also propose specific improvements to the technique that allow for higher image contrast and better fluorophore sampling (i.e.: resolution) in PALM/STORM experiments.

HILO illumination exploits the refraction of a laser beam at the interface between a glass coverslip and a watery sample to generate an inclined beam, which is also squeezed into a “light sheet”. We modelled the behavior of this refracted beam based on Gaussian optics, used it to predict the thickness of the light sheet at various angles of inclinations and with different beam diameters, and tested the predictions by experimentally measuring the beam size along the optical axis of the objective both in the far field (in air) and directly within gel samples with refractive index close to that of water.

In Gaussian optics, the waist of a light beam is defined as the beam radius in its point of maximal intensity and minimal divergence[49] (where its radius is considered to be the radial distance from the beam propagation axis at which the intensity is reduced by a factor $1/e^2$).

In an epifluorescence configuration, in which the laser beam is not inclined, the beam waist is given by $\widetilde{w}_0$ (Figure 20, Figure 21). But when the beam is inclined by an angle θ_i with respect to the normal plane, its waist w_0 is given by $w_0 = \widetilde{w}_0 \cos\theta_i$. When refraction occurs at the interface between coverslip and sample, the beam is further inclined by an angle θ_r according to Snell’s law (Equation 5), and therefore the waist is squeezed a second time. The waist of the refracted beam within the sample is therefore w'_0 and given by[50]:

$$w'_0 = w_0 \frac{\cos\theta_r}{\cos\theta_i} = \widetilde{w}_0 \cos\theta_r$$

Equation 5

The refractive index of the water-immersed sample is always lower than the refractive index of the coverslip, which means that to a higher θ_i corresponds a higher θ_r and thus increasing θ_i always causes a reduction in the beam waist within the sample (w'_0)

The parameter indicating the thickness of the light sheet with respect to the z axis (which is perpendicular to the coverslip surface) is:

$$dz = 2\widetilde{w}_0 / \tan\theta_r$$

Equation 6

As mentioned before, refraction takes place along one axis, therefore the beam thickness along both the x and y directions does not vary with the inclination of the laser. As such, in the case of a Gaussian beam, dx and dy are the same and are equal to $2\widetilde{w}_0$, which also corresponds (in a geometrical optics approximation) to the diameter of the illuminated field of view (R) (Figure 20).

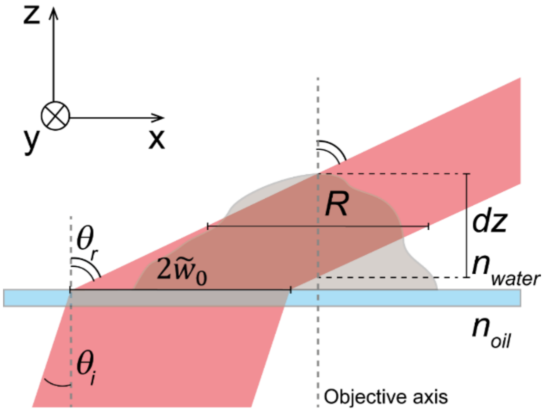

Figure 20. Geometrical optics representation of a refracted laser beam crossing a specimen immersed in water.

A small dz is desirable for HILO microscopy, because a thinner light sheet means having a more confined excitation volume and a lower out-of-focus fluorescence background. But with small beam waists, another parameter of Gaussian beams comes into play and becomes problematic: the confocal parameter, which is given by the following expression[49].

$$d\zeta = 2\zeta_0 = \frac{2\pi {w'_0}^2}{\lambda}$$

Equation 7

Where ζ indicates the axis of propagation of the refracted beam (Figure 21).

The confocal parameter ζ_0 indicates the distance from the minimal divergence point, along the beam propagation axis, within which the beam radius $w(z)$ does not exceed its waist by a factor of $\sqrt{2}$, and its double $d\zeta$ is used to define the range within which a Gaussian beam can be considered to be collimated. It follows from Equation 7 that Gaussian beams with smaller waists diverge faster, which represents a hindrance when applied to HILO microscopy as a heavily divergent beam means that the excitation laser intensity is not uniform within the field of view. The graph in Figure 22 shows how, given a certain refraction angle θ_r, both the confocal parameter and the thickness of the light sheet dz change with changing the beam size $dy = 2\widetilde{w}_0$ (which corresponds to the field of view diameter R).

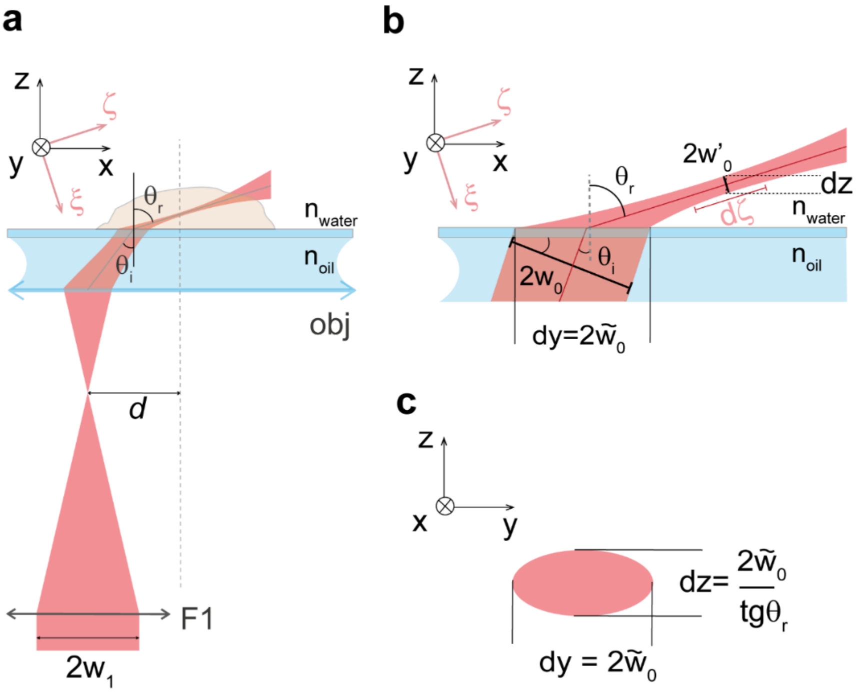

Figure 21. Schematic illustration of several parameters of an inclined Gaussian beam in a HILO configuration. The dependency between d and θ_r is illustrated in (a). (b) shows the different waists of a non-inclined ($\widetilde{w}_0$) and of an inclined beam (w_0 in oil and w'_0 in water), as well as the two important parameters of dz and $d\zeta$. (c) shows the dz and dy parameters from another perspective, where the point of view is directed along the x axis.

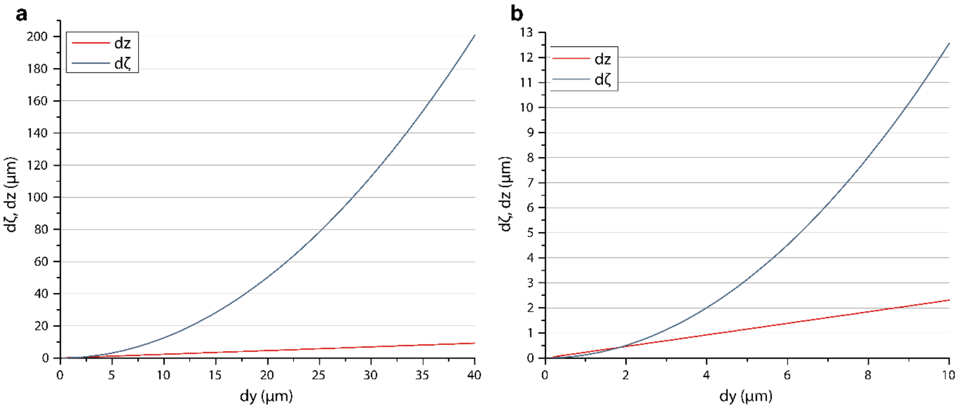

Figure 22. (a) Confocal parameter ($d\zeta$) and thickness (dz) of a Gaussian beam are plotted against the diameter of its section on the focal plane (dy). The values are relative to a beam inclined at a θ_r of 77°. (b) Detail of the same graph in a range between $dy = 0$ and $dy = 10$.

As the inclination angles θ_i and θ_r of the light sheet are directly dependent on the distance d between the beam and the objective optical axis (Figure 21), it is important to define the relationship between these different parameters. This can be derived from the consideration that the optical path crossed by a beam, collimated by an objective with a focal distance of f_{obj}, between the objective and its focal plane is equal to $n_{oil}f_{obj}$ (where n_{oil} is the refraction index of the immersion oil, which is the same of the coverslip glass). As such, the relationship between the distance d and θ_i is the following:

$$d = n_{oil}f_{obj}\sin\theta_i$$

Equation 8

By applying Snell's law we can also obtain the refraction angle θ_r:

$$\begin{cases} \theta_i = \sin^{-1}\left(\dfrac{d}{n_{oil} f_{obj}}\right) \\ \theta_r = \sin^{-1}\left(\dfrac{d}{n_{sample} f_{obj}}\right) \end{cases}$$

Equation 9

These mathematical relationships are especially useful, as the only parameter that can be experimentally controlled is the distance d, as will be explained in section 3.1.1.

In conclusion, from the previous theoretical description of inclined Gaussian beams in a HILO optical configuration we obtain that there are two crucial parameters, namely the thickness dz and the confocal parameter $d\zeta$, that determine the effectiveness of a specific beam configuration when applied to an imaging experiment. The thickness determines the total volume of sample that undergoes illumination, which directly influences the amount of out-of-focus fluorescence being collected by the objective and contributing to the image background; as such, a small dz is desirable. Conversely, the confocal parameter needs to be reasonably large (at least larger than the field of view) so that the illumination intensity can be considered uniform across the imaged section of the sample. As $d\zeta$ decreases when reducing the beam thickness, a compromise is necessary between these two parameters.

Moreover, dy is another factor to be considered as it determines the field of view size, intended as the area of the sample at the focal plane which is subject to illumination. Ideally, dy would be large enough that the field of view covers the entirety of the area imaged by the camera; but as dy is directly proportional to dz, the aforementioned issue of minimizing dz plays a role in the optimization of this parameter for imaging.

A separate argument should be made concerning the optimal θ_r of an inclined optical sheet configuration. In the original description of HILO[48], the authors report employing an inclination of 77° for the beam within the sample, without discussing their choice of angle. An obvious consideration would be that employing higher inclination angles and getting closer to TIR could be desirable, as that would translate to a smaller dz. However, the transition between refraction and total internal reflection does not happen suddenly at a specific angle, but rather the portion of reflected light of an inclined beam increases gradually with θ_i and θ_r until it reaches 100% at the critical angle. The reflection coefficients of an electromagnetic wave at a certain angle are given by the Fresnel equations, and depend also on the polarization direction of the wave with respect to the incident surface[49]:

$$\begin{cases} r_s = \dfrac{n_{oil}\cos\theta_i - n_{water}\cos\theta_r}{n_{oil}\cos\theta_i + n_{water}\cos\theta_r} \\ r_p = \dfrac{n_{oil}\cos\theta_r - n_{water}\cos\theta_i}{n_{oil}\cos\theta_r + n_{water}\cos\theta_i} \end{cases}$$

Equation 10

For $n_{oil} = 1.515$ and $n_{water} = 1.33$, we obtain that with a θ_r of 77° the reflectivity is included between 11.4% for a p-polarized wave and 20.1% for an s-polarized wave.

At higher angles, the increase in reflectivity means that the illumination of the sample becomes uneven, as the deeper sections (the ones that are farther away from the coverslip glass) receive a lower intensity of light, while TIRF phenomena become preponderant at the glass/water interface.

Therefore, we opted to perform all of our measurements with a θ_r of 77°.

3.1.1 Experimental setup

We set forth to experimentally test our theoretical predictions about the characteristics of a highly inclined optical sheet. The two beam parameters that can be directly controlled are the pre-refraction waist $\widetilde{w}_0$ and the distance *d* by which the propagation axis of the laser is displaced with respect to the optical axis of the objective.

We designed and built an optical setup for single-molecule fluorescence imaging with adjustable size and inclination of the excitatory laser beams, which is illustrated in Figure 23. 640 nm, 488 nm, 532 nm and 405 nm diode lasers are directed along the same optical axis by specific dichroic mirrors (DM1, DM2, DM3, DM4) and are magnified through a 10x telescope (L3, L4) before being focused on the back focal plane of a TIRF Nikon 60x oil immersion objective with a numerical aperture of 1.49. Two adjustable apertures – an iris and a slit – are placed on a conjugated plane with the sample to set the pre-refraction dimension of the excitation beam. The objective is placed in inverted configuration, and the fluorescence signal is separated from the excitation through the DM4 dichroic mirror, which directs it towards the detection components. The 60X fluorescence image generated after the tube lens is magnified 3 times through telescope lenses L6 and L7 and projected on an Andor iXon X3 EMCCD camera, with a final field of view of 40 x 40 μm^2 and a pixel size of about 90 nm. The objective is mounted on a piezoelectric translator to adjust the focus and the sample is mounted on a piezoelectric stage with two independent axes of movement.

The inclination of the excitatory beam can be controlled by moving the motorized translator T1, which shifts both the M3 mirror and the L5 lens sideways with respect to the optical axis of the objective (Figure 24).

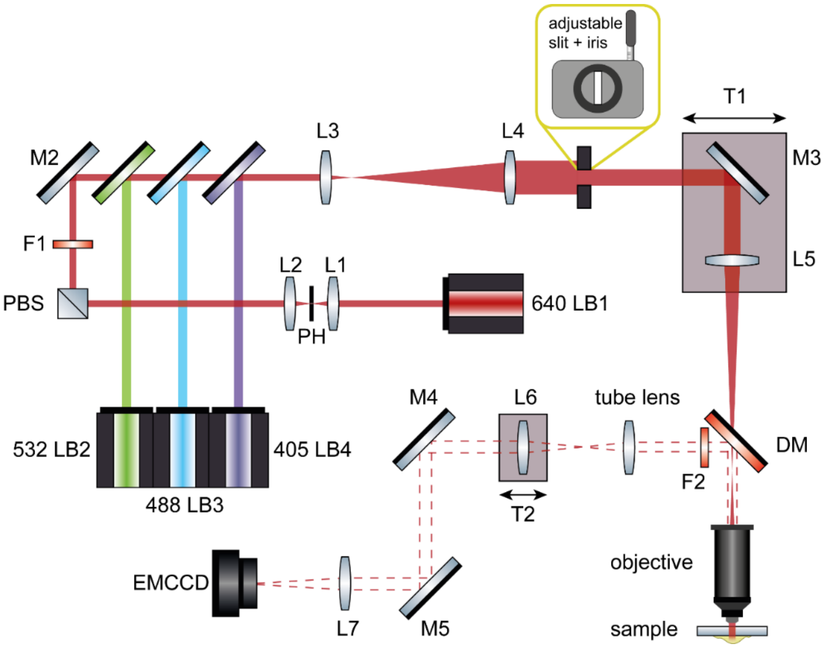

Figure 23. Schematic representation of our custom-built microscopy setup.

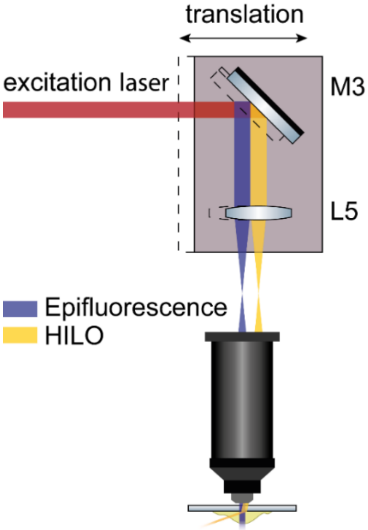

Figure 24. Schematic representation of the system used to control the refraction angle of the inclined beam. The translator displacement corresponds to the parameter d discussed in section 3.

3.2 Profile measurement in the far field

In order to experimentally verify the relationship between the distance d of the beam from the optical axis and the refraction angle θ_r (Equation 9, section 3.1), we measured the height h and the profile of the refracted beam on a screen positioned at a fixed distance L from the objective, while changing the distance d through the motorized translator. In this experiment, the beam is refracted from a coverslip into air and hits a screen after traveling a distance $R = \sqrt{L^2 + h^2}$ from the objective (Figure 25). Pictures of the beam profile on the screen were taken with a digital camera mounted on a tripod.

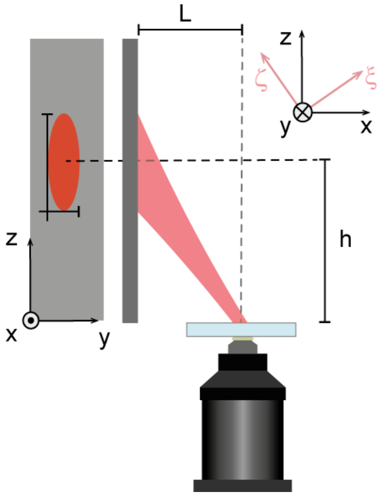

Figure 25. Schematics of the experimental setup employed for far-field measurements of the beam profile.

The beam radius in the y and ξ directions at a distance R is given by[49]

$$w_{y,\xi}(R) = \sqrt{1+\left(\frac{R\lambda}{\pi w_{0\,y,\xi}^{2}}\right)^{2}}$$

Equation 11

where $w_{0_{y/z}}$ are the refracted beam waists along y and z for $R \approx 0$ (immediately after refraction):

$$\begin{cases} w_{oy} = \widetilde{w}_0 \\ w_{0\xi} = \widetilde{w}_0 \cos\theta_r \end{cases}$$

Equation 12

For distances $R \gg \frac{\pi w_0^2}{\lambda}$ Equation 11 can be approximated as:

$$w_{y,\xi}(R) \approx \frac{R\lambda}{\pi w_{oy,\xi}}$$

Equation 13

From the previous considerations, we obtain that the ratio between w_ξ and w_y is only dependent on the θ_r refraction angle. Since the beam is projected on a screen which is not perpendicular to the propagation axis, the measured waists along z and y will be $w_z = w_\xi/\sin\theta_r$ and w_y. Their ratio is thus given by:

$$\frac{w_z}{w_y} = \frac{1}{\sin\theta_r \cos\theta_r}$$

Equation 14

We took pictures of the inclined beam projected on the screen at different values of x and fitted the intensity profiles along y and z with a function describing a Gaussian beam intensity after a propagation distance R:

$$\begin{cases} I(y) = \dfrac{A}{w_y}\, e^{-2\frac{(y-y_O)^2}{w_y^2}} \\ I(z) = \dfrac{A}{w_z}\, e^{-2\frac{(z-z_O)^2}{w_z^2}} \end{cases}$$

Equation 15

From this fit we were able to extract parameters w_y and w_z, while the position of the Gaussian peak indicated the height h at which the inclined beam hits the screen. Figure 26 shows the measured w_z/w_y ratios at different angles, plotted against the theoretical model.

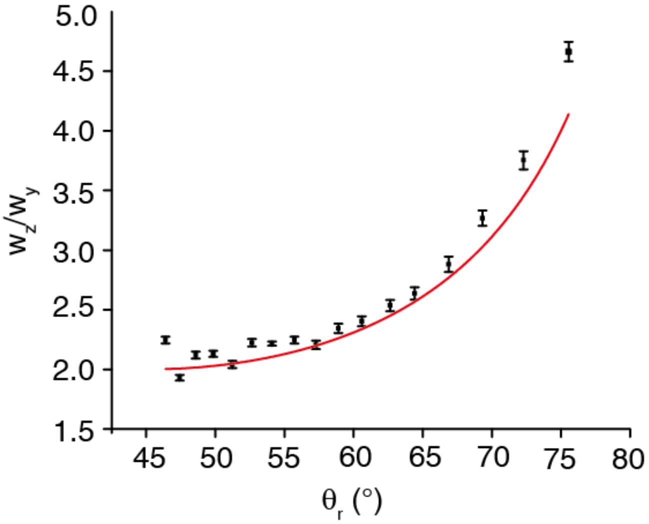

Figure 26. Experimental measurements of the ratio between the beam radii w_z/w_y, plotted alongside the theoretical predictions. The error bars of the measured values are obtained by summing the relative errors on the fitting parameters σ_{w_z} and σ_{w_y}

As the theoretical model fit quite well our experimental data, we assumed that our predictions on the beam propagation would be reasonably accurate in water as well. As such, we designed two possible improvements to the inclined beam profile that would allow for better imaging performances according to our models by reducing dz while keeping a large enough confocal parameter and field of view.

The first improvement consisted in reducing the diameter of the excitation beam before it is refracted at the coverslip-water interface from 40 µm down to 20 µm by reducing the iris diameter in our experimental setup accordingly. This would result in a smaller dz while keeping the confocal parameter beyond the size of the field of view (~20 µm). The major downside would be the restriction of the effective field of view from an area of around 1260 µm^2 to an area of around 315 µm^2.

The second proposed improvement consisted in reducing the size of the adjustable slit, which is located on our setup on the same plane as the iris, resulting in a final beam section on the (x, y) plane that would no longer be a circle, but roughly a 10 µm x 40 µm rectangle. By reducing the size of the beam along the refracted axis only, we would further reduce dz to around 2.3 µm while maintaining a confocal parameter of around 13 µm according to our model (Figure 22). The downside would be a reduction in the effective size of the field of view to an area of around 400 µm^2, which is however bigger than what we obtained with a circular aperture of 20 µm in diameter.

3.3 Profile measurement within the sample

In order to test our predictions about the inclined beam parameters in water, we developed a technique that allowed us to indirectly measure the beam thickness in an aqueous sample, within several microns from the glass/water interface at which refraction takes place. We came up with a model sample consisting of a 2% agarose gel containing uniformly distributed 100 nm fluorescent TetraSpeck™ microspheres (Invitrogen). This sample composition was ideal, as the agarose gel has a refraction index very similar to that of water[51] ($n_{agarose} = 1.344$, $n_{water} = 1.33$) and the microspheres, while being sub-diffraction limit in size, were large enough to be stably trapped in the gel mesh and evenly distributed across the sample. A detailed description of the procedure employed to prepare this model sample is reported in appendix 7. The fluorescent beads contain four different dyes, each one absorbing and emitting in well-separated spectral intervals; as such, they can be employed in conjunction with many different laser sources and emission filters. In our case, we employed a 640 nm laser for excitation (Figure 23) while filtering the fluorescence emission with a dark red bandpass filter (central wavelength: 680 nm, bandwidth: 42 nm).

In order to characterize the vertical profile of the inclined beam we needed to optically scan the fluorescent bead sample along the *z* axis under laser excitation, while keeping the laser beam itself fixed in space. This was achieved by keeping the objective still and moving the L6 lens (Figure 27) in the detection path with a translator, thereby focusing different planes of the sample on the camera.

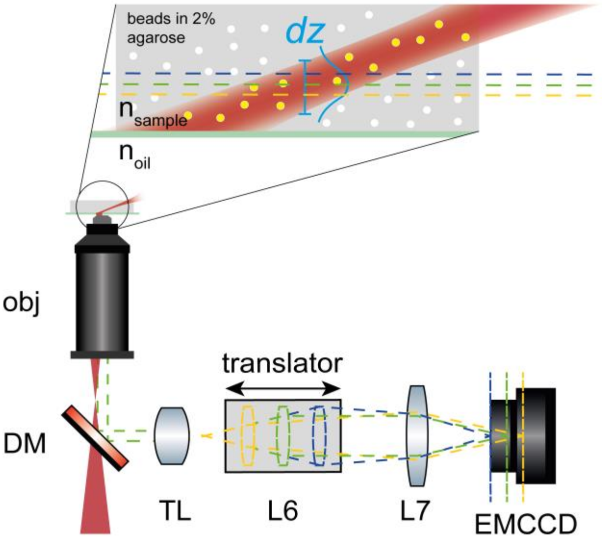

Figure 27. By displacing the lens L6 along the detection optical axis, it is possible to focus on the camera different planes of the sample which do not correspond to the objective focal plane. Within a certain movement range, image aberrations are negligible and this allows to scan the sample in z without moving the objective.

As the displacement of the lens L6 does not correspond to an equal displacement of the focal plane, a calibration was needed in order to be able to move the focal plane by known distances along the z axis. The translator on which L6 is mounted has a movement range of 2.5 cm. We performed the calibration in the following way: after moving the translator to the 0 cm position, a microscope slide with a calibration reticle was imaged on the camera. The translator was then moved of a known distance, and the objective was moved using the piezoelectric translator to refocus the calibration slide. The movement of the piezoelectric translator corresponds to the displacement of the objective focal plane, which was recorded and plotted against the corresponding displacement of L6 (Figure 29). However, this calibration is only valid as long as the focal plane is centered on a glass surface: when imaging within an aqueous sample, a correction needs to be applied to take into account the propagation of light in differently refracting media[52]. If focusing the surface of a coverslip, the medium separating the objective and its front focal plane will be optically homogeneous as immersion oil has the same refraction index of glass; but when the focal plane is located inside a sample with a different diffraction index (such as an agarose gel), the focal distance changes. As such, we associated the displacement of the piezoelectric stage $\Delta z_{piezo} = z'_{piezo} - z_{piezo}$ (Figure 28) to a corresponding focal plane displacement in the sample ($\Delta z_{agarose} = z'_{agarose} - z_{agarose}$) with the following formula[53]:

$$\Delta z_{piezo} = \frac{n_{oil}}{n_{agarose}} \Delta z_{agarose}$$

Equation 16

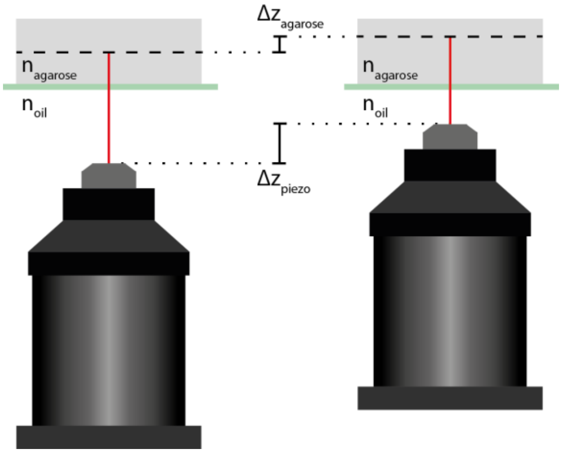

Figure 28. Schematic illustration of the difference between the displacement of the objective along z and the corresponding displacement of the focal plane within the agarose gel.

Knowing this, we could associate the displacement of the L6 lens translator to a corresponding displacement of the focal plane within the agarose sample as reported by the calibration graph in figure Figure 29.

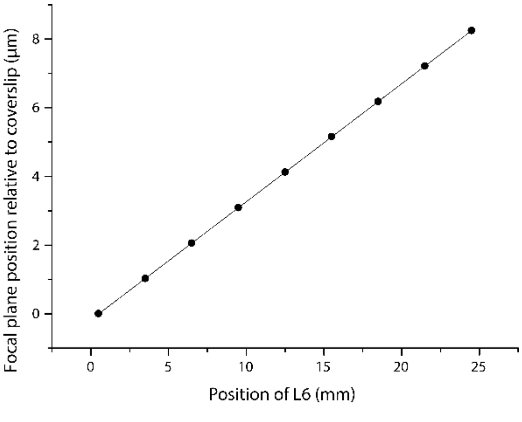

Figure 29. Calibration curve for obtaining the focal plane displacement from the movement of L6. Experimental data corrected with Equation 16 (dots) were fitted with a linear function.

After calibrating our focusing system, we set forth to measure the local intensity of the inclined beam at different depths in the agarose sample. We did this by measuring the fluorescence intensity of individual, in-focus beads and taking it as a function of the local intensity of the beam. As the fluorescent microspheres are smaller than the optical diffraction limit, the light emitted by an individual bead results in a PSF on the acquired image, which is described by an Airy function as discussed in section 1.2. As such, it is possible to determine the axial position of a bead by measuring the intensity and the number of visible rings in the diffraction pattern[54]. Most importantly, it is easy to determine which beads in the image are in focus. Before making the measurements, however, a preliminary calibration of the bead fluorescence intensity versus laser power was necessary to verify its linear dependence and to avoid saturation of the bead fluorescence emission. In this way, we could ensure that the measurement of the bead fluorescence intensity really reported on the intensity of the inclined excitation beam. In-focus beads were excited with increasing laser intensities and their fluorescence output measured and plotted against the laser power (Figure 30). The fluorescence intensity of individual beads was calculated as the difference between the average signal measured within a circular region of interest (ROI) centered on the bead, and the average background intensity measured within a circular crown outside the region of interest (Figure 31).

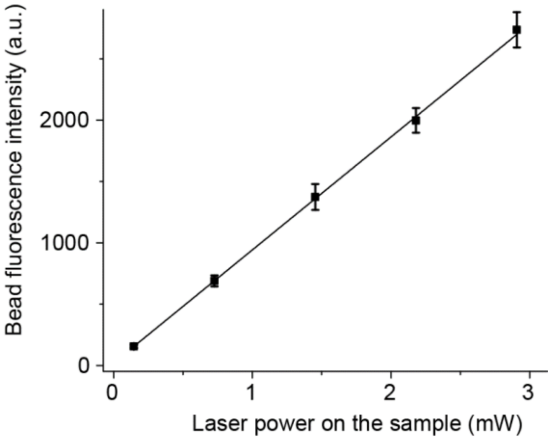

Figure 30. Verification of the linear dependence between excitation laser power and fluorescence intensity of the beads. The error bars represent the standard deviation on the mean between individual bead intensities.

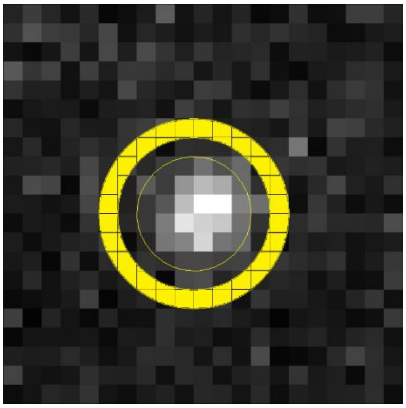

Figure 31. Regions of interest (ROIs) employed to measure the fluorescence signal coming from individual beads. The total intensity of each bead (I_{tot}, or "gross signal") was calculated as the average intensity of the pixels included within a 3-pixel radius approximately centered on the PSF peak. The background (I_{back}, or "tare signal") was considered to be the average intensity of the pixels in a circular crown centered on the emission peak and separated by one pixel (yellow area). The final intensity (I_{bead}, or "net signal") was calculated as $I_{bead} = I_{tot} - I_{back}$.

Another consideration was necessary to obtain reliable information from the beam profile measurements. As the laser beam is kept fixed in space, every time an image is taken of a certain plane, all of the other planes within the beam volume are subject to illumination as well. This means that the fluorescence intensity coming from planes imaged later during the experiment could be underestimated due to the progressive bleaching of the dyes contained in the microspheres. In order to correct for this possible bias we conducted the measurements using a so-called “to&fro” procedure: two sets of images are taken, the first one starting from the coverslip plane and going towards the deeper layers of the gel sample (the “to” image set), and the second one starting from the deepest layer and going back all the way to the coverslip plane (the “fro” set). In this way, each fluorescent bead is imaged twice and the fluorescence intensity associated with it is calculated as the geometric mean intensity from the two images. The “to&fro” procedure is schematized in Figure 32, and the reasoning behind it is the following: let’s assume we are going to image n planes along the z axis, where each plane is numbered $n_z \in [1, n]$. Each time an image is taken, all of the planes are illuminated for a time t_{exp} equal to the exposure time of the image. Therefore, the n_z plane will be exposed to a total illumination time $n_z t_{exp}$ when its first image is taken (the “to” image), and to an illumination time $[(2n+1) - n_z]t_{exp}$ when its second image is taken (the “fro” image). Assuming that the fluorescence intensity I_{nz} of a microsphere laying in the plane n_z decays exponentially with laser exposure time, we have that its intensity in the “to” image is given by:

$$I_{n_{z_{to}}} = I_{n_z} e^{-\frac{n_z t_{exp}}{\tau}}$$

Equation 17

Where τ is the characteristic bleaching time of the bead, while the intensity of the bead in the “fro” image will be:

$$I_{n_{z_{fro}}} = I_{n_z} e^{-\frac{(2n+1-n_z)t_{exp}}{\tau}}$$

Equation 18

As such, the geometric mean between I_{to} and I_{fro} for any given bead will be independent of the term n_z:

$$\langle I \rangle = \sqrt{I_{n_{z\,to}} I_{n_{z\,fro}}} = I_{n_z} e^{-\frac{(2n+1)t_{exp}}{\tau}}$$

Equation 19

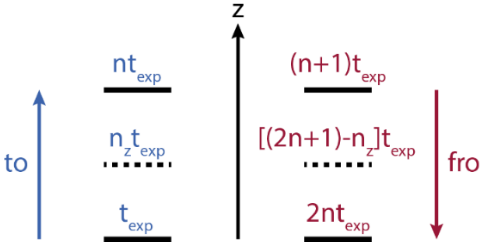

Figure 32. Schematic representation of the "to&fro" experimental method to compensate for bleaching in the bead intensity measurements. Each horizontal level represents a plane of the sample, with associated its experienced exposure time after it has been imaged during the "to" series (blue) and the "fro" series (red).

The corrected fluorescence intensity of individual beads was calculated in this way, and the average intensity of all the imaged beads on each plane was plotted as a function of the axial position of the plane, and the profiles obtained this way were fitted with Gaussian functions.

We employed this protocol to measure the vertical profiles of three different HILO configurations, within an ~8-μm range and with a step size of about 1 μm. We characterized an inclined beam with a circular profile of 40 μm in diameter (standard HILO) and our two improved configurations: an inclined beam with a circular profile of 20 μm in diameter, and an inclined beam with a rectangular profile of 10 μm x 40 μm (HILO-slit). The measured profiles and their respective fitted Gaussian functions are shown in Figure 33.

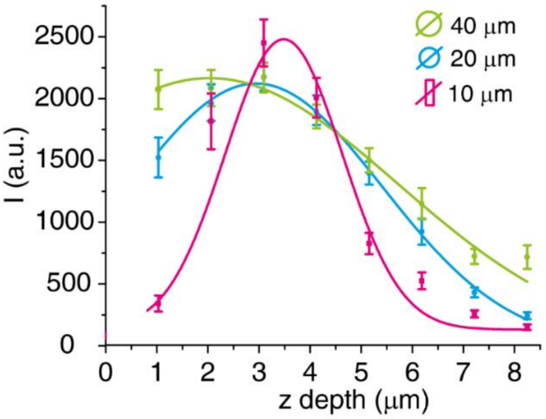

Figure 33. Experimental measurements of the z profiles of the three inclined beam configurations, plotted alongside the respective fitted Gaussian functions. Error bars represent the standard deviation of the mean intensity of the beads imaged at each plane. Green: standard HILO (40 µm diameter); cyan: HILO with reduced iris diameter (20 µm); magenta: HILO-slit (10 µm x 40 µm).

In order to validate our measurements we compared our results with those obtained with a mathematical model of the experiment. In fact, the curves displayed in Figure 22 represent the beam thickness *dz* along the optical axis of the microscope, whereas our measurements are based on an average intensity of the beam on the imaged plane. Therefore, based on the Gaussian beam propagation model described above, we calculated the average intensity of the beam on each imaged plane and fitted its dependence with *z* with a Gaussian function, as in an *in silico* experiment. The beam profiles predicted by the model are, as expected, larger than the beam thickness calculated along the microscope optical axis and showed a good agreement with the experimental results, as shown in Figure 34.

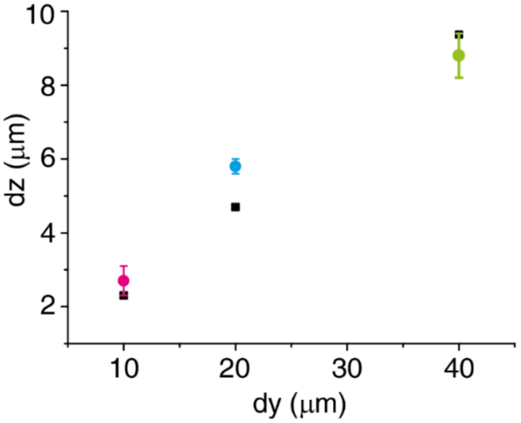

Figure 34. Color coded: values of dz calculated on the fitted profiles in Figure 33 and plotted over dy. Error bars represent the standard error on the fitting parameters. Black: in silico *predictions.*

By considering the thickness of the beam to be the full width at half maximum (FWHM) of the fitted Gaussian function (which corresponds to about 0.6 dz), we obtained that by employing a standard HILO configuration with a circular illumination profile and $dy = 40\ \mu m$, the resulting beam thickness is 8.8 ± 0.6 μm. It is worthy to note that this value is comparable to the thickness of a single mammalian cell adhered to a coverslip surface, which represents the most common type of microscopy specimen employed in single-molecule localization techniques. This means that the reduction in excited sample volume is de facto negligible, whereas a subcellular excitation volume would be more beneficial in terms of background minimization. Subcellular beam thickness was achieved with both the restricted diameter beam ($dz = 5.8 \pm 0.2\ \mu m$) and with the HILO-slit beam ($dz = 2.7 \pm 0.4\ \mu m$).

3.4 Effects on the image contrast in diffraction-limited imaging

After characterizing the different illumination configurations as described in the previous sections, we set forth to compare the performance of each configuration when applied to an actual imaging experiment.

We began by measuring the difference in the contrast of images obtained by illuminating a sample with each of the four beam configurations: epifluorescence (Epi), HILO with a circular illumination profile and $dy = 40\ \mu m$ (HILO Ø 40 µm), HILO with a circular illumination profile and $dy = 20\ \mu m$ (HILO Ø 20 µm) and HILO with a rectangular illumination profile of 10 µm x 40 µm (HILO-slit). As reducing the illumination volume translates to reducing the out-of-focus fluorescence, we expected that excitation beam configurations with reduced dz would result in images with enhanced contrast and sharper details.

To test this hypothesis quantitatively, we decided to image a model sample similar to the one employed for the beam thickness measurements described in section 3.3. However, sparsely distributed beads in an agarose gel do not provide an appreciable background – as would be the case in a real biological specimen – so we introduced a source of background fluorescence in the form of a low concentration of dissolved fluorescent molecules in the gel matrix. While preparing the agarose gel, we dissolved 2.6 nM of a phalloidin conjugate of Alexa Fluor 647, which has an emission peak at 668 nm and is therefore visible in the same spectral range as the TetraSpeck beads.

We imaged different areas of the fluorescent gel using each beam configuration. For each image, the in-focus beads were analyzed using the fitting algorithm developed by Gardini *et al.* in [54]. The algorithm fits a two-dimensional Gaussian function on the image produced by individual beads, and calculates the bead intensity (I), corresponding to the peak of the Gaussian, as well as the background level (I_{back}), corresponding to the

Gaussian offset. In order to calculate the signal-to-background ratio of the imaged beads, we also needed to measure the dark noise (I_{dark}) produced by the EMCCD camera, which we did by recording a few frames with the camera aperture covered by an opaque lid and averaging the pixel values in the resulting images. The signal-to-background ratio (SBR) is then calculated as:

$$SBR = \frac{I - I_{back}}{I_{back} - I_{dark}}$$

Equation 20

An SBR value was calculated for each imaged bead, and the final SBR for a given illumination configuration was calculated as the average of at least 40 individual SBRs. The results are shown in Figure 35.

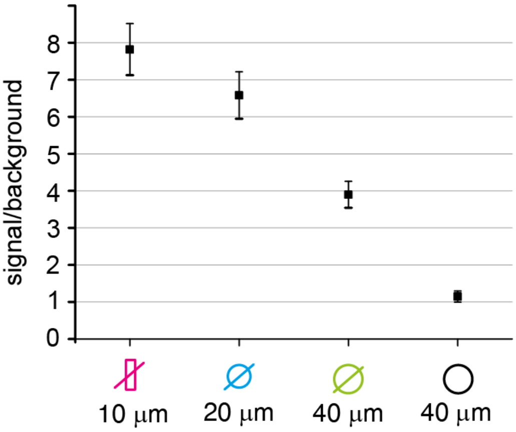

Figure 35. SB values measured for the different beam configurations.

The absolute value of the SB ratio measured for a given specimen is of course heavily dependent on the composition of the specimen itself, but comparing these different techniques in a homogeneous sample clearly shows the relationship between a reduced illumination beam thickness and higher signal-to-background ratios in the resulting images.

To have a qualitative idea of how these different techniques fare in an actual biological sample, we performed fluorescence imaging in mammalian cells. We grew, stained and fixed AC16 human cardiomyocytes following the same protocol used for STORM imaging (appendix 7). The cells were stained with phalloidin-conjugated Alexa 647 in order to fluorescently label the actin cytoskeleton and some images were taken in areas where several close-by actin filaments or bundles were clearly visible. The four configurations were employed one after the other to image the same field of view. Figure 36 shows a detail of one such image series, where the intensity profile of an actin bundle was measured along the yellow line. By normalizing each plot to its maximum value and superimposing them in the same graph (Figure 36), the progressive reduction of background fluorescence with decreasing beam dz becomes evident.

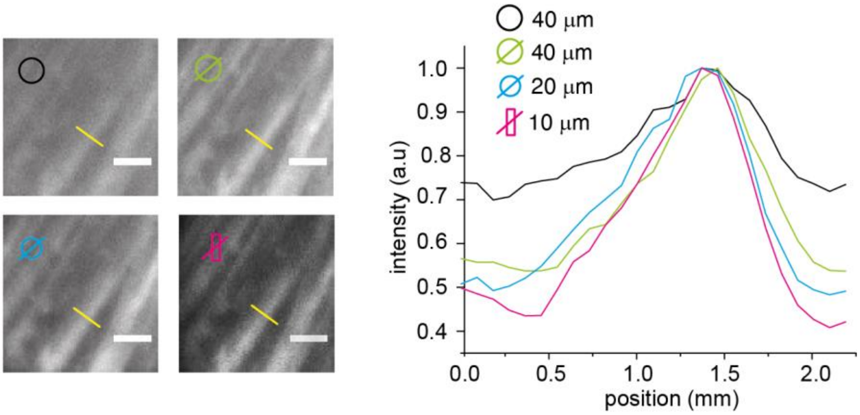

Figure 36. Details and intensity profiles of fluorescently labelled actin filaments imaged with different illumination configurations.

3.5 Effects on super-resolution imaging

After characterizing each illumination configuration and evaluating their effects in diffraction-limited fluorescence microscopy, we set forth to test them in localization-based super-resolution imaging. Localization-based imaging is especially susceptible to problems arising from high fluorescence background, given the small amount of photons emitted by single fluorophores that constitute the signal detected in these kind of experiments; as such, we expected a noticeable improvement in the quality of SMLM images acquired with background-limiting configurations.

We compared the performances of Epi, HILO ∅ 40 µm and HILO-slit illuminations in STORM super-resolution experiments of the actin cytoskeleton of mammalian cells. The first proposed improved configuration (HILO ∅ 20 µm) was not further characterized, as HILO-slit proved to be superior in every parameter measured previously (FOV area, dz,SB ratio of images).

More specifically, for each configuration we quantified:

1) The single-molecule localization accuracy.
2) The fluorophore sampling efficiency (i.e., the amount of individual fluorophores successfully localized per frame).

In order to avoid any bias due to the high heterogeneity of biological samples, our plan was to perform consecutive acquisitions with different techniques on the same field of view. This introduced a problem concerning mainly the quantification of sampling efficiency, which is discussed in detail in section 3.5.2 along with our solution. But in general, the problem lies in the response of photoswitchable fluorophores to prolonged excitation: as described by Dempsey *et al.* in [37], after being subjected to high-intensity illumination, it takes a while for the majority of the photoswitchable fluorophores in a specimen to convert to their “off” non-fluorescent state. During the first ~400 seconds of sustained illumination in a STORM movie, a decay in the number of active fluorophores per frame can be observed, which ends when the fluorophores reach a "quasi-equilibrium" between on and off states[37]. After this point the only decay in the number of visible emitters per frame is due to the slow, irreversible photobleaching of the fluorescent molecules.

We cultured, fixed and stained human embryonic kidney cells from the HEK 293 cell line as described in the general protocol for the preparation of cells for STORM imaging in appendix 7. We labelled the actin cytoskeleton of these cells with a phalloidin conjugate of Alexa Fluor 488 and imaged them with the STORM imaging procedure described in section 2.1.1, using a 488 nm laser for excitation and filtering the fluorescence signal coming from the dye with a suitable bandpass filter (central wavelength: 530 nm, bandwidth: 43 nm). After choosing a suitable field of view, continuous excitation with the 488 laser in the Epi configuration at an elevated intensity (~5.3 kW/cm^2) was carried on for 600 seconds to bring the photoswitchable dyes to a steady switching state, as described above. We introduced this step to decrease the density of active chromophores and to make sure the results obtained with different configuration were comparable. Then, a STORM movie of 10,000 frames was acquired with the Epi configuration, followed immediately by another STORM movie of 10,000 frames acquired on the same field of view with the HILO Ø 40 µm configuration, and ultimately by another movie acquired with the HILO-slit configuration. This procedure was carried out on three independent fields of view.

To compare the exact same sample region with the three different techniques, a rectangular region of interest (ROI) was drawn using ImageJ around the field of view delimited by the HILO-slit illumination. All of the STORM movies were cropped using the same ROI before being processed with ThunderSTORM, using the same parameters shown in section 2.2.2 and in Figure 16, to reconstruct the super-resolution images. A simple filter was applied on the resulting localization maps, based on the parameters assigned by ThunderSTORM to each localized spot (frame > 1 & intensity < 10000 & offset > 1) in order to eliminate false positive localizations, such as artifacts due to elevated fluorescence background or possible cosmic rays impacting the camera chip during image acquisition. After which, the localization maps were analyzed as described in sections 3.5.1 and 3.5.2.

3.5.1 Quantification of localization precision

Localization precision was calculated as the standard deviation between the localized positions of persisting fluorophores (i.e. fluorophores that remain visible for multiple consecutive frames). A custom MATLAB script was developed to automatically search for persisting fluorophores and perform this calculation on whole image stacks. The input is a localization map produced by ThunderSTORM, which contains the x and y positions of each localized fluorophore along with the number of the frame in which it has been localized. The MATLAB script compares the molecular coordinates in consecutive frames, and identifies a persisting fluorophore as a point that appears multiple times within a given distance threshold. Only localized fluorophores that kept being visible for at least 8 consecutive frames were taken into consideration. To avoid confusing spatially close fluorophores for the same molecule, if two fluorophores appearing in the same frame could both be considered to be a persisting fluorophore from the frame before (because they both fall within the specified distance threshold), they are both excluded from the analysis. The distance threshold was set at 20 nm, after testing different values (up to 100 nm) and not finding any significant difference in the resulting localization precisions.

For each persisting fluorophore, the localization precisions along the x and y axis were independently calculated, and the final localization precision was computed as the average between the two. The values reported in Figure 37 represent averages between – respectively – 27, 19 and 51 persisting fluorophores.

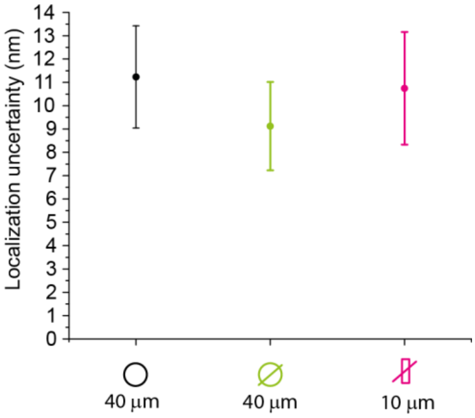

Figure 37. Measured single-molecule localization uncertainty for either Epi, HILO Ø 40 µm and HILO-slit, obtained from repeated localizations of persisting fluorophores. Error bars represent standard deviations.

Identifying individual persisting fluorophores in a STORM movie of a densely labelled specimen is not often possible, due to the risk of confusing nearby molecules for the same one. This resulted in a relatively small statistical sample of a few tens of fluorophores, which however shows that the localization precision does not seem to be significantly affected by the reduction in illumination volume.

3.5.2 Quantification of localization events: photobleaching correction

As mentioned in section 3.5, comparing the localization efficiency of the three techniques, while employing them one after the other on the same field of view, proved to be tricky. The issue was caused by bleaching: as each STORM acquisition lasts 400 seconds (10,000 frames with a frame integration time of 40 ms), subsequent measurements on the same field of view would suffer by a decreased number of localizations due to the progressive bleaching of the underlying fluorescent dyes. We needed to find a way to correct the number of localizations in subsequent acquisitions by taking into account the bleaching caused by the previous imaging sessions.

We did this by performing a series of calibration measurements in order to quantify, for each beam configuration, the "dead fraction" (as opposed to the "survival fraction" defined by Dempsey *et al.*[37]) of Alexa Fluor 488 over the same imaging times employed in the STORM acquisitions, i.e.: the percentage of fluorophores that have undergone bleaching over the course of a period of sustained illumination.

Simply, three independent STORM movies of 30,000 frames each (one for every beam configuration) were acquired, starting after the same 600-seconds buffer period employed for the experimental acquisitions. The field of view was different for each movie, as we assumed that the survival fraction would only be a function of the illumination configuration and the exposure time. These calibration movies were reconstructed into super-resolved localization maps with ThunderSTORM, and the resulting .csv files were imported into MATLAB and further processed in the following way:

1) For every calibration map, a plot was made with the number of localized spots per frame on the y axis, and the frame numbers on the x axis (Figure 38).

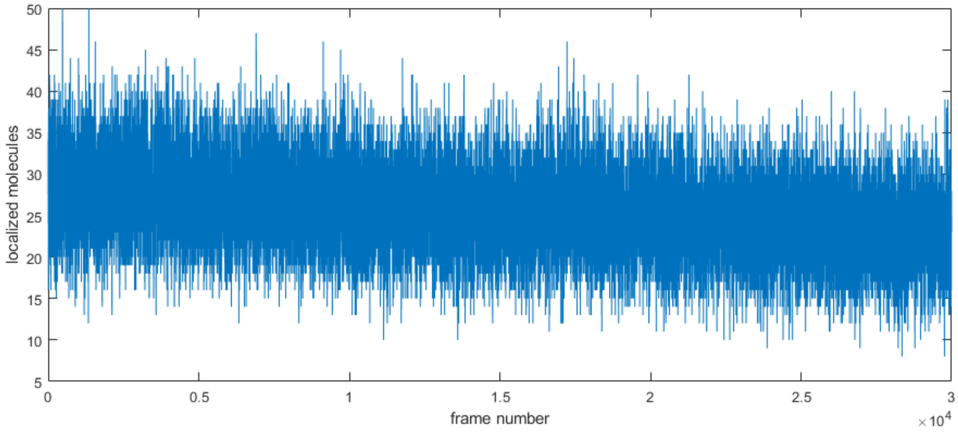

Figure 38. Number of localized molecules plotted over frame number in the Epi calibration measurement.

2) The MATLAB curve fitting toolbox was used to fit the plot with an exponential function, in the form of $n(n_{frame}) = n(0)e^{-b \cdot n_{frame}}$. This function represents the decay rate of the number of localizations per frame n due to bleaching after n_{frame} frames of exposure in each of the three configurations; b represents the bleaching rate expressed in n_{frame}^{-1}.

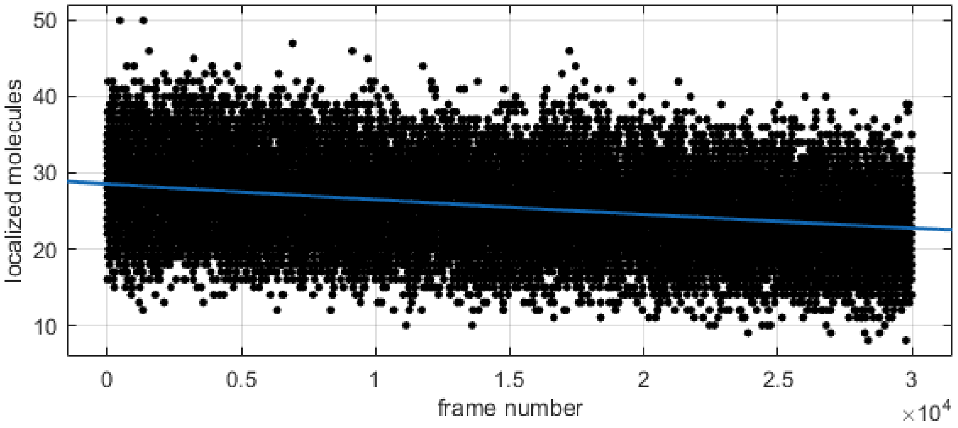

Figure 39. Exponential fit of the data in Figure 38.

3) We used the fitted functions to calculate the survival fraction S of Alexa Fluor 488 as a function of the frame number after Epi and HILO illumination. There was no need to correct for the bleaching occurred during the HILO-slit acquisition, as it was the last in every series.

$$\begin{cases} S_{Epi}(n_{frame}) = \dfrac{n_{Epi}(n_{frame})}{n_{Epi}(0)} = e^{-b_{Epi} \cdot n_{frame}} \\ S_{HILO}(n_{frame}) = \dfrac{n_{Hilo}(n_{frame})}{n_{HILO}(0)} = e^{-b_{HILO} \cdot n_{frame}} \end{cases}$$

Equation 21

Where n_{Epi}, n_{Hilo}, n_{Slit} are the localization numbers per frame for each configuration. We then obtained the dead fraction D as:

$$\begin{cases} D_{Epi}(n_{frame}) = 1 - S_{Epi}(n_{frame}) = 1 - e^{-b_{Epi} \cdot n_{frame}} \\ D_{HILO}(n_{frame}) = 1 - S_{HILO}(n_{frame}) = 1 - e^{-b_{HILO} \cdot n_{frame}} \end{cases}$$

Equation 22

We then calculated D_{Epi} and D_{HILO} for a 10,000-frames window:

$$\begin{cases} D_{Epi} \cong 0.0728 \\ D_{Hilo} \cong 0.1445 \end{cases}$$

Equation 23

4) Knowing the dead fraction parameters, we could then correct the number of localizations in each STORM image acquired after the first to take into account the bleaching caused by the previous acquisition. We did so in the following manner:

$$\begin{cases} N'_{Epi} = N_{Epi} \\ N'_{Hilo} = N_{Hilo}(1 + D_{Epi}) \\ N'_{Slit} = N_{Slit}(1 + D_{Hilo} + D_{Epi} - D_{Hilo} D_{Epi}) \end{cases}$$

Equation 24

Where N_{Epi}, N_{Hilo} and N_{Slit} are the amounts of localized fluorophores for respectively Epi, HILO Ø 40 µm and HILO-slit measurements; while

N'_{Epi}, N'_{Hilo} and N'_{Slit} are the corrected ones. Both the non-corrected and the corrected values are displayed in Figure 40. The number of localization for each experimental series (Epi → HILO Ø 40 µm → HILO-slit) was normalized on the value obtained for the respective Epi measurement. The data points shown in Figure 40 are averages obtained from the normalized values of the three independent experimental series.

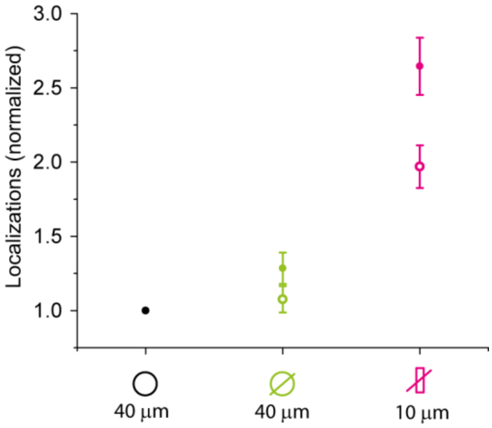

Figure 40. Number of fluorescent molecules localized in the same field of view in 10,000 frames-long STORM movies with different illumination configurations. Closed symbols represent values corrected to compensate for bleaching, while open symbols represent raw experimental values. Error bars represent the standard error of the mean.

Figure 41 shows one of the series of STORM images used for this analysis, along with a closeup of some details. The number of points making up the reconstructed images has been adapted to reflect the bleaching corrections described above. The procedure employed to readapt the images is explained in detail in appendix 7.

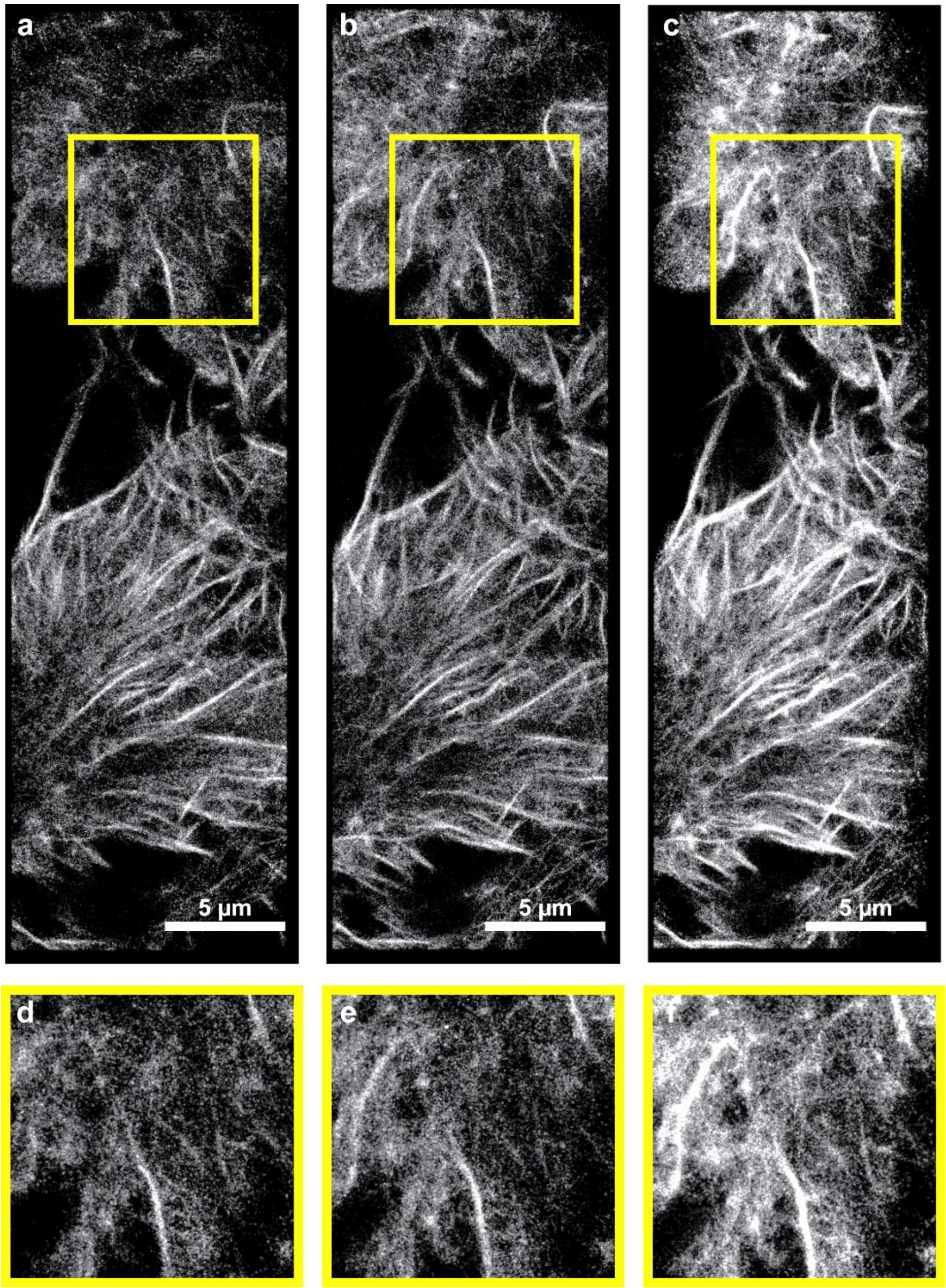

Figure 41. Super-resolved images reconstructed from one of the experimental series described in the previous sections. The same field of view was imaged first with (a) Epi illumination, followed by (b) HILO Ø40 µm and finally (c) HILO-slit. All the images were reconstructed from a 10,000-frames STORM movie. The highlighted detail in (a,b,c) is magnified and shown in (d,e,f) respectively.

In addition to the quantitative results obtained by counting the number of localizations for each image, we can get a clear qualitative idea of the different performances of the three tested configurations simply by looking at the reconstructed images. Reducing the dz to subcellular levels has a massive impact on the contrast of the blinking sequences which result from a STORM acquisition, which in turn allows for a much more effective sampling of the underlying fluorescent molecules. Even though the HILO-slit configuration was employed last in all of the imaging sequences, the reduction in background fluorescence was more than sufficient to compensate for the reduction in available fluorophores due to bleaching, and resulted in roughly double the amount of localizations per frame obtained with either Epi or standard HILO illumination. The images in Figure 41 are the result of a number of acquired frames (10,000) that is typically insufficient for an adequate sampling of the actin cytoskeleton, due to the high density of labelled structures and to the presence of very fine details in the image. However, by employing the HILO-slit configuration it was possible to generate highly detailed images, which with a standard HILO technique would be possible only by acquiring 2 to 3 times the amount of frames recorded in these experiments.

3.6 Conclusions and future perspectives

Summing up what has been discussed in the first part of this thesis, we have: (i) developed a set of experimental techniques that allow the characterization of laser beams propagating within microscopy samples; (ii) employed this technique to measure important parameters of the widely employed HILO microscopy technique, and set conditions to improve it in its most crucial aspect, i.e. the reduction of out-of-focus fluorescence background; (iii) tested our proposed improvements alongside the state-of-the-art technique in both diffraction-limited and super-resolution microscopy experiments.

Our results provide some valuable insight into the limitations of the traditional HILO approach. We demonstrate that the properties of a full-size highly inclined beam at 77° are indeed inadequate for reducing the out-of-focus fluorescence when imaging single layers of cells adhered to a coverslip, as the thickness of the illuminated volume (15 μm) is comparable to that of the sample itself. We show that, by decreasing the beam thickness through the use of a slit-shaped aperture in the proper orientation, we could obtain a noticeable increase in the image contrast in diffraction-limited microscopy as well as a massive increase in sampling efficiency of individual fluorescent molecules when applied to STORM super-resolution imaging.

The obvious limitation of the HILO-slit configuration is the reduction in field of view area. However, our future plans are to try and tackle this problem by changing the orientation of the camera in the detection path of the optical system. If the camera were inclined with respect to the optical axis in such a way that the field of view is coplanar with the excitation beam, the in-focus illuminated area would no longer be limited by the beam profile and the projected thickness *dz* would be even smaller. A similar approach has been used by Tang *et al.* in 2018[55].

In its current state, HILO-slit is a valid technique to acquire higher-quality images of relatively small cellular details or whole-cell images of smaller organisms, such as bacteria. The increase in sampling efficiency in single-molecule localization microscopy also means that this technique allows for faster PALM/STORM acquisitions and could couple very effectively with other time-reducing imaging techniques (such as the aforementioned "high-density labelling" super-resolution techniques) to move localization-based imaging towards the observation of living cells.

PART II

–

QUANTITATIVE IMAGING OF EFFLUX PUMPS IN PLANKTONIC AND BIOFILM-ASSOCIATED BACTERIA THROUGH SINGLE-MOLECULE LOCALIZATION MICROSCOPY

4 Bacterial efflux pumps and their role in antimicrobial resistance

Antimicrobial resistance (AMR) in pathogenic bacteria is a growing, worldwide health concern. As much as 50,000 people die prematurely every year due to antimicrobial-resistant infections in Europe and in the US alone. Massive use of antimicrobial drugs, such as antibiotics, during much of the last century has led to a widespread insurgence of microbial strains with varying degrees of resistance to one or several of the drugs that were previously being used to contrast them. One of the most successful strategies that bacteria use to resist antimicrobial treatment is that of expressing efflux pumps (EPs) – i.e., a class of transporter proteins capable of extruding a wide range of molecules from bacteria such as harmful metabolic products or xenobiotics. EPs are active transporter proteins, employing various sources of energy to make molecules move against their concentration gradient from the inside of cells to the outside. When EPs target antimicrobial compounds, they can lower the intracellular concentration of such drugs to low enough levels that their harmful effects are nullified[56,57]. These transport proteins are ubiquitous in bacteria, and often it is not the evolution of new varieties of pumps but rather the overexpression of preexisting ones with different physiological roles that determines an effective form of acquired resistance to multiple antimicrobial drugs, leading to a multiple drug resistance (MDR) phenotype[58]. In Gram-negative bacteria, the increased level of resistance to a broad range of antibiotics is often the product of a synergistic effect between efflux pump overexpression and intrinsic resistance mechanisms, such as the presence of an impermeable outer membrane[59].

Known EPs can be categorized into five superfamilies, based on amino acid sequence homology and on the energy source used to perform their function[60,61]:

- Major Facilitator Superfamily (MFS)

- ATP-Binding Cassette (ABC)
- Small Multidrug Resistance (SMR)
- Multi AnTimicrobial Extrusion (MATE).
- Resistance-Nodulation-cell Division (RND)

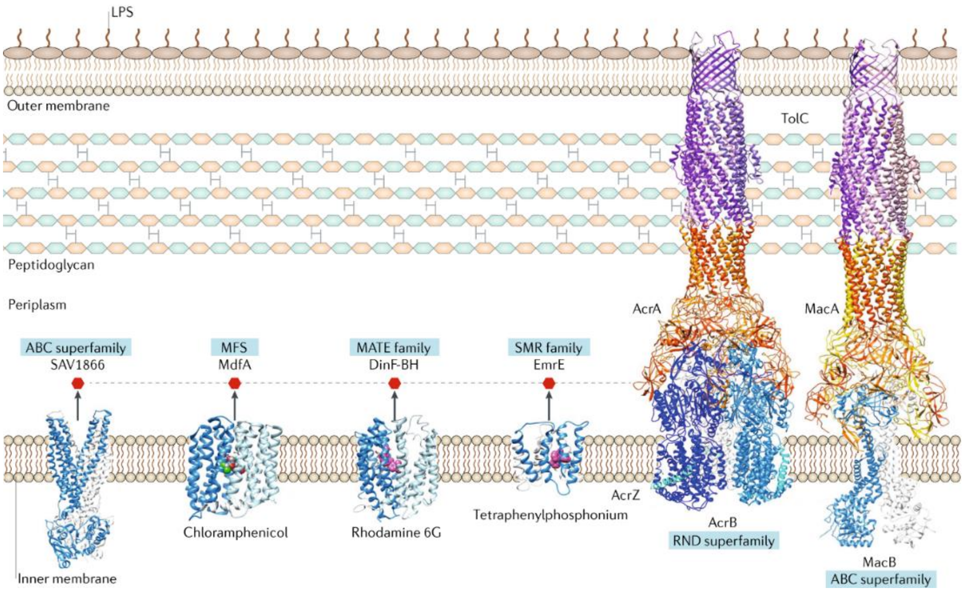

Figure 42. Proteins and complexes representative of each of the five EP superfamilies displayed in the context of a gram-negative bacterial membrane. The ABC transporters use ATP to drive transport processes, while the other families depicted use electrochemical gradients as an energy source. The groups also differ in architectural features, such as the number of transmembrane domains and the ability to form functional complexes with other proteins. The RND superfamily drug transporters mostly assemble with their partner proteins to form tripartite pumps, binding substrates at the outer leaflet of the inner membrane and from the periplasm and effluxing them to the cell exterior. By contrast, members of the other families of drug transporters usually function as independent units in the inner membrane, translocating substrates across the membrane bilayer. Image and caption retrieved from [61].

This part of the thesis is deals with the RND superfamily, which is the most widespread EP type in Gram-negative bacteria. These pumps use the difference in proton gradient between the bacterial periplasm and cytoplasm as a source of energy[62], also known as proton motive force or PMF. The natural ligands of RND-type pumps are a variety of lipophilic and amphiphilic molecules such as fatty acids, dyes and detergents, but this family of EPs boasts an especially broad range of substrates including many antibiotics. This makes the RND family especially problematic in clinical scenarios, as most MDR phenotypes occurring in Gram-negative bacteria are associated with the overexpression of these proteins[63,64].

4.1 The acridine resistance complex in E. coli as an efflux pump model for gram-negative bacteria

AcrAB-TolC is the main representative of the RND family pumps in *Escherichia coli*[65,66] and also the best characterized. AcrAB-TolC is a tripartite system consisting of three different proteins: AcrB, an antiporter with broad substrate specificity which spans the cytoplasmic membrane; TolC, an outer membrane channel; and AcrA, a periplasmic adapter[67,68]. After a substrate has entered the periplasmic space through a porin or by simple diffusion, it can get into contact with AcrB either as it crosses the inner membrane or when it is already in the cytoplasm. AcrB interacts with the substrate by extruding it directly into the external medium through the TolC channel. Deletions in *acrAB* or *tolC* genes have been shown to increase the susceptibility of *E. coli* to a wide range of antibiotics and other toxic compounds[69].

Although AcrAB-TolC is only found in Enterobacteriaceae such as Escherichia coli, Salmonella species and Klebsiella pneumoniae[70], many RND efflux pumps that are homologous to it exist in other species of Gram negative bacteria, which makes this specific system an ideal model for studying this widespread and clinically relevant class of proteins. Examples include the MexAB-OprM, MexCD-OprJ and MexXY-OprM EPs in

Pseudomonas spp., AdeABC in *Acinetobacter baumannii*, CmeABC in *Campylobacter spp.* and MtrCDE in *Neisseria spp.*[65,70–77].

4.1.1 Structure and mechanism of AcrAB-TolC

The AcrAB-TolC membrane pump has been extensively studied, and the structures of its components as well as that of the fully assembled complex have been determined through X-ray crystallography[78–85] and Cryo-EM[68,86–89]. The fully assembled complex consists in an AcrB trimer and a TolC trimer, linked through the periplasmic space by an AcrA hexamer (Figure 43). AcrB is a transmembrane protein anchored to the inner bacterial membrane, acting as the motor component of the tripartite complex. AcrB is responsible for the recognition and binding of substrates, and acts as a proton-drug antiporter by employing the transmembrane proton gradient created by bacterial respiration[90,91] to undergo conformational changes which push substrate molecules towards the outside of the cell. TolC forms a channel spanning the outer bacterial membrane that can exist in open or closed conformations[89]. TolC is a multifunctional protein, as it is part of several other efflux complex belonging to various superfamilies such as AcrEF-TolC, EmrAB-TolC, MdtEF-TolC, MdtABC-TolC and MacAB-TolC[92–99]. Ultimately, AcrA is a periplasmic protein that acts as an adapter, connecting AcrB with TolC[67]. Moreover, a few years ago a small peptide named AcrZ has been identified that binds to AcrB and appears to affect the pump specificity, conferring it a broader substrate tolerance[100].

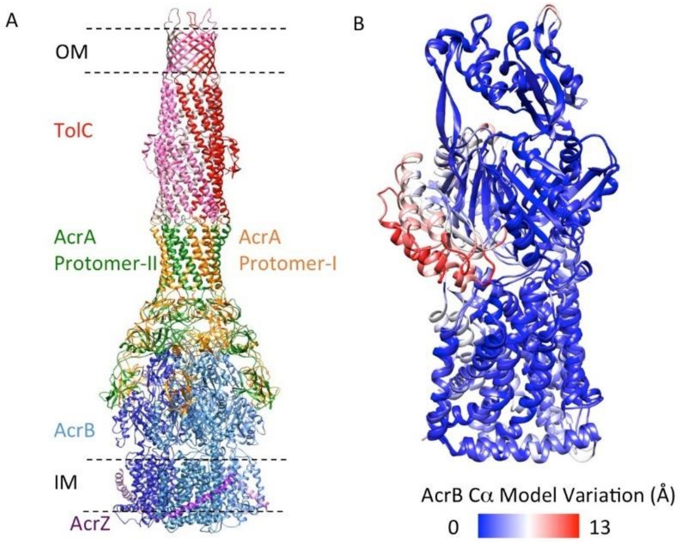

Figure 43. CryoEM asymmetric structure (5.9 Å resolution) of the AcrABZ-TolC complex in the presence of puromycin, which is a substrate of the pump. (A) Structure of asymmetric AcrABZ-TolC pump. Subunits are color-coded accordingly: TolC (red and pink), AcrA (orange and green), AcrB (blue) and AcrZ (purple). (B) Conformational change taking place in the AcrB subunits over the course of the pumping cycle. The three subunits are superimposed and the color gradient indicates displacement (increasing from blue to red) of the residuals from the subunit in the resting conformation. Image retrieved from [89].

Crystallographic studies on AcrB have shown that the AcrB trimer acquires an asymmetric structure when in the presence of a substrate, suggesting that a functional cycling between the three AcrB monomers takes place during pump activity[82,83] (Figure 43). Recent cryo-EM data on the full complex, moreover, show that a global rearrangement in the quaternary structure of the pump takes place when the complex transitions from an apo (resting) to a ligand-bound state; more specifically, it appears that the TolC channel is sealed shut when the pump is in a resting state and the AcrB trimer is symmetric. Upon binding to a substrate, structural changes in AcrB are relayed to AcrA, which in turn causes the TolC channel to open, allowing the ligand to be expelled in the outside environment[89].

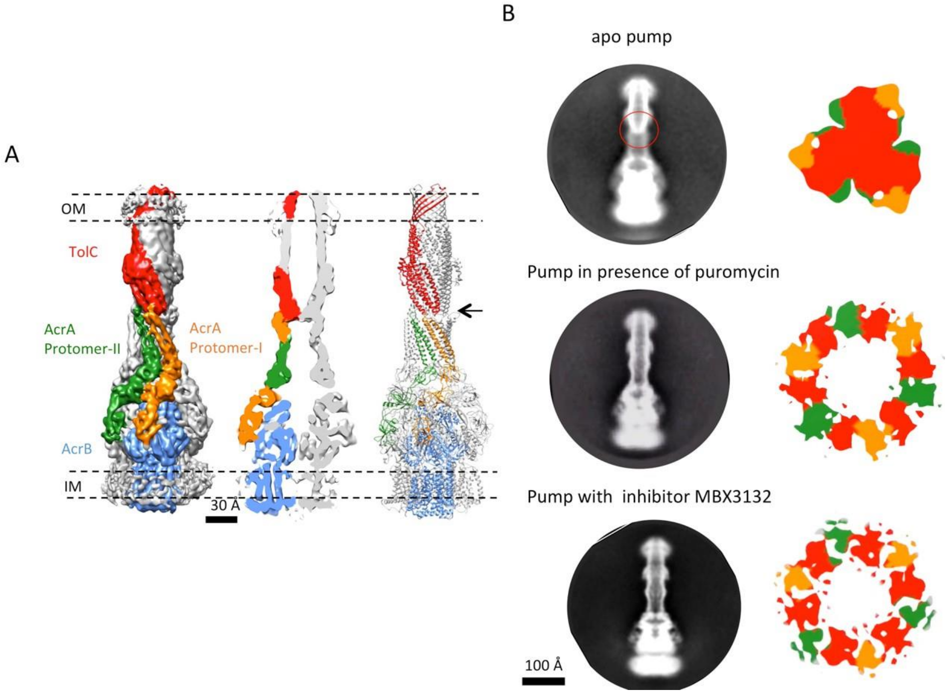

Figure 44. (A) CryoEM map (6.5 Å resolution) of the pump with TolC in the closed state, visualized in side view along the membrane plane. (left) The four components within one asymmetric unit of the assembly are color-coded: TolC (red), AcrA (orange and green) and AcrB (blue). (middle) A sliced view of the pump shows the closed channel. (right) Ribbon representation of the pump with a closed-state TolC with the same color code as in the left panel. The black arrow indicates the closed site in TolC. (B) Comparison of reference- free 2D averages (left) and slice view of 3-D maps at the arrow (right) of the apo pump with closed TolC (top), pump in presence of puromycin (middle) and pump with the inhibitor MBX3132 (bottom). Image and caption retrieved from [89].

4.1.2 The acrAB operon and its regulation

The *acrA* and *acrB* genes constitute an operon in the chromosome of *E. coli*, and therefore share the same promoter[101]. Expression of the *acrAB* operon is subject to a complex and layered regulation system, broadly divided in local repression and global regulation through a number of transcription factors[70].

Local repression of *acrAB* is under the control of AcrR, a transcriptional repressor of the TetR family whose gene is located a few bases upstream of the *acrAB* operon and transcribed divergently[102–104]. AcrR represses its own synthesis, acting more as a modulator of *acrAB* with the effect of preventing pump overexpression; indeed, inactivation of *acrR* through mutations has been associated with MDR in clinical isolates of *E. coli*. However, AcrR expression appears to be induced under the same general stress conditions which lead to AcrA and AcrB overexpression[102,103], suggesting a more complex repression network. For example another local regulation system of *acrAB* is mediated by AcrS/EnvR, a transcriptional repressor that seems to inhibit *acrAB* expression in response to efflux activity by another EP system, AcrEF-TolC[105].

In addition to the aforementioned repression systems, a number of transcription factors exist that positively regulate the expression of *acrAB*. The primary regulator of *acrAB* (as well as *tolC*) expression is the MarA transcription factor, a global transcriptional activator encoded as part of the multiple antibiotic resistance operon *marRAB*. MarA expresses its function by upregulating a number of genes involved in drug efflux and MDR. However, in the absence of external stimuli the *marRAB* operon is repressed by its own product MarR, which tightly regulates the intracellular concentration of MarA[106–108]. MarR has the ability to recognize and bind phenolic compounds, which can modify its affinity towards the operator sequence of *marRAB*. A number of these substrates, such as sodium salicylate, can cause the detachment of MarR from the operator leading to the transcription of *marA*[109].

A number of other transcription factors are also thought to regulate the expression of *acrAB*, including the histone-like nucleoid structuring protein (H-NS) and the suppressor of division inhibition (Sdi)A[65], but their role is still not completely clear.

Two other known factors that contribute to the regulation of the AcrAB-TolC efflux pump in *E. coli* are post transcriptional and post translational in nature.

The translation of the AcrAB proteins can be enhanced by the carbon storage regulator A (CsrA), a global translation regulator involved in the modulation of several genes[110]. CsrA is an RNA binding protein that recognizes and binds the 5’ end of the acrAB transcript, facilitating ribosome binding and protein synthesis initiation[110].

The global regulation of MDR-associated genes by MarA can also be influenced at a post translational level by the action of the Lon protease, an ATP-dependent protease associated with a variety of cellular activities[111,112]. Lon proteolytically degrades MarA, resetting its intracellular concentration to basal levels when an inducing stimulus is not present[113]. Indeed, inactivating mutations in Lon lead to increased AcrAB-mediated efflux and MDR[111].

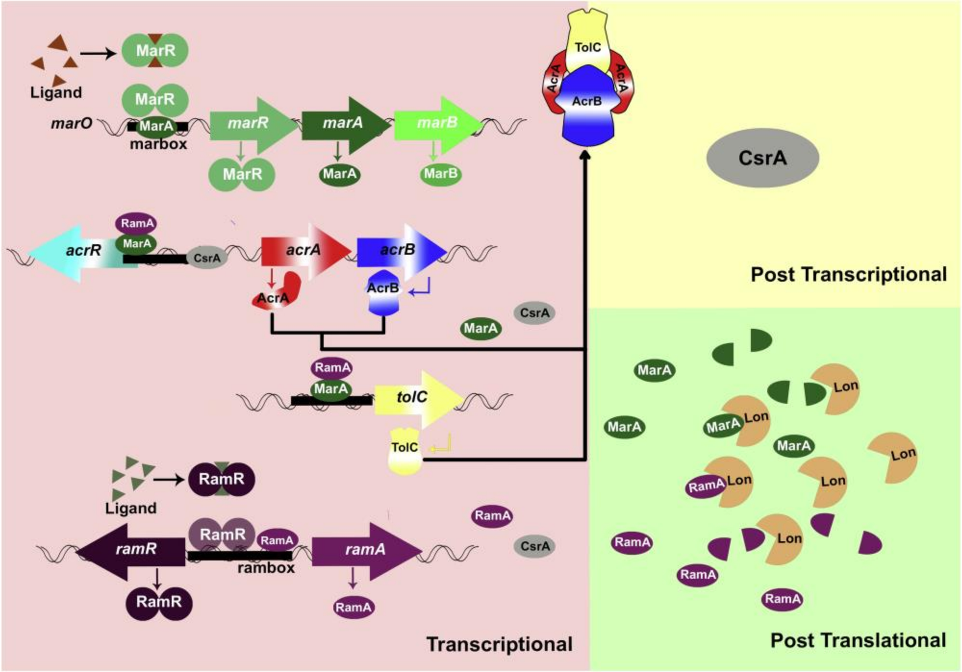

Figure 45. Transcriptional regulation of the acrAB (red and blue) and tolC (yellow) regulon by E. coli marRAB (green) and S. enterica ramRA (purple) genes. Post-transcriptional regulation of acrAB by CsrA (grey) and post-translational regulation of RamA by Lon protease (orange). Image and caption retrieved from [70].

4.2 Biofilms: a prokaryotic step towards multicellularity

Although historically bacteria have been mostly studied as free-swimming (planktonic) organisms, most naturally occurring prokaryotes actually live as complex surface-associated communities referred to as biofilms[114–117]. The realization that biofilms can adhere and grow on almost every surface in aqueous environments, including a range of industrially and medically relevant surfaces, has sprouted a widespread interest in biofilm research in the last few decades[118]. Another important problem driving biofilm research is that biofilm-associated pathogenic bacteria have a tendency to become highly resistant to a broad range of environmental stressors, including hydrodynamic shear forces, host immune defenses and antimicrobial treatments, often leading to recurrent or chronic infections[119–121]. Biofilm-associated bacteria have been found to be up to 2500 times more resistant to antibiotics than their freely swimming counterparts[122], and the mechanisms underlying this extreme resiliency are still not completely clear. Biofilm communities are enmeshed in a viscous extracellular matrix composed mainly of exopolysaccharides (EPS), proteins and nucleic acids which surely hampers the diffusion of harmful molecules[123,124], but more specific defense mechanisms are known to be at play. For example, many biofilms are packed with amyloid protein fibers named “curli”[125,126], which organize in a sort of “net” that has been demonstrated to selectively bind and inactivate bacteriophages[127]. Biofilm resistance to antibiotics has been linked to an increased expression of EPs[128,129], which is likely the evolutionary solution to a “waste management problem” within cramped microbial communities[129,130], and the use of EP inhibitors on biofilms has been shown to significantly decrease the resistance of biofilms against drugs[129,131]. Biofilms are highly heterogeneous structures: in most cases they harbor multiple microbial species, which entertain both cooperative and competitive relationships, but also isogenic bacteria in single-species biofilms are known to differentiate into subgroups with widely different gene expression patterns, a behavior not dissimilar to that of cells making up a multicellular organism[115]. The mechanisms regulating group behaviors within biofilms are mostly intercellular signaling (quorum sensing) and reaction to environmental concentration gradients[115]. A characteristic of biofilm environments is the existence of concentration gradients of nutrients and oxygen from the outside of the biofilm to the biofilm base layer, at the interface with the substratum[128,132], as well as pH gradients and gradients in the concentration of a variety of signaling molecules such as quorum sensing factors[116] (Figure 46).

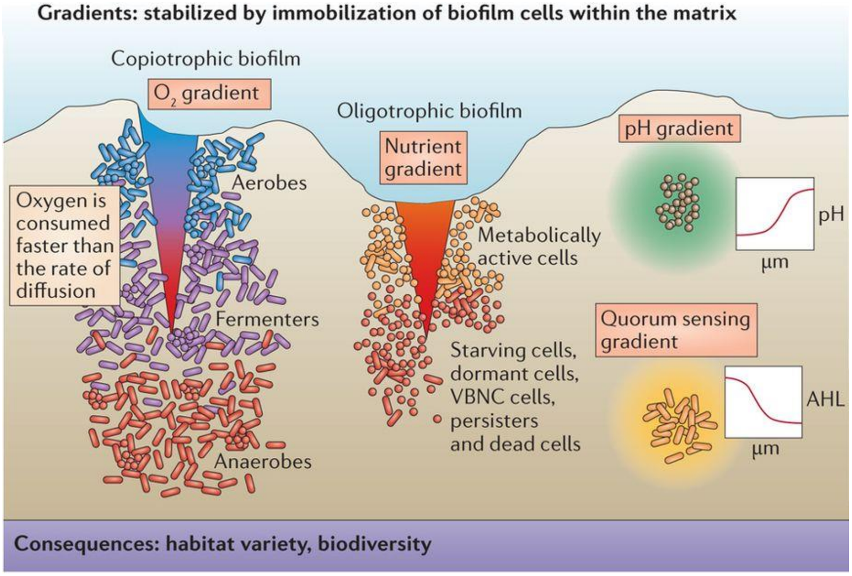

Figure 46. The formation of the EPS matrix leads to the establishment of stable gradients that generate different localized habitats at a small scale. In an aerobic copiotrophic biofilm [ed, where the nutrient concentration is abundant], organisms are stratified according to oxygen availability, which becomes depleted in the lower layers of the biofilm, as the consumption of oxygen by the cells located in the higher layers of the biofilm is faster than the rate of diffusion. Similarly, in aerobic oligotrophic biofilms [ed, in nutrient-limiting conditions], nutrient consumption by organisms in the upper layers results in the starvation of organisms in the lower layers, which may lead to the adoption of slow growth states such as the persister state, and to an increase in cell death. Other gradients that are present in biofilms include pH gradients, which are produced by cellular metabolism, and gradients of signaling molecules, in which the concentration of quorum sensing molecules varies according to the distance from producing cells. Image and caption retrieved from [116].

The lower availability of energy sources is associated with a decreased metabolic activity of the bacteria residing in the biofilm core[133–135]; this “dormancy” state of certain bacterial subgroups, which are referred to as “persisters”[136], is believed to play a major role in the ability of biofilms to withstand heavy antimicrobial treatments and to rebuild the colony after a near-complete wipeout[137]. However, even though the existence of persisters in many bacterial biofilms has been thoroughly proven, with this phenotype having been observed for the first time in the early 1940s[138,139], the mechanisms through which these bacteria achieve such especially high levels of resistance are still under a heated debate[140]. More specifically, while some researchers claim that bacterial dormancy can alone explain this behavior[136,140–142], others argue that the peculiar resilience of persisters is caused by some active mechanism, such as an enhanced antimicrobial efflux activity caused by the overexpression of EPs[143,144]. Currently available data on the expression of efflux pumps in bacterial populations is the result of bulk experiments such as DNA microarrays[129,145–147] and transcriptional fusions to reporter genes[148,149], which do not provide any information related to the internal inhomogeneity of the samples. As such, questions about the expression and distribution of efflux pumps within biofilms in general and persisters in particular remain yet unanswered.

5 Quantification of the expression and distribution of AcrB through single-molecule imaging

As we mentioned earlier, much is still unclear about the regulation dynamics of efflux pumps and their spatial distribution within and between bacterial cells. Due to traditional gene expression assays being performed on bulk samples such as plated colonies or broth cultures, after incubation times of hours or days, all the experimental data we get is a global average obtained from billions of individual bacteria. We lack the ability to (i) detect gene expression changes occurring on short timescales, and to (ii) do so with single-cell or even subcellular spatial resolution. Furthermore, in order to acquire any noteworthy information about spatial organization in relatively static, three-dimensional communities such as biofilms, we need to be able to obtain our data without perturbing the overall structure of the samples. Moreover, subtle changes in the expression pattern of a given protein would be apparent only if the measurement had a very high precision – ideally, on the order of the single protein.

Our ideal solution came from single-molecule localization microscopy.

As described in section 2, PALM allows investigators to determine the position of individual proteins in a cell with a few nanometers of accuracy. However, the way PALM is traditionally performed does not convey any useful information about the amount of proteins being imaged, but merely a high-resolution information about the shape of the structure that these proteins make up. The system through which photoactivatable fusion proteins are expressed in biological samples is usually a plasmid vector[150–152], which results in the transcription and translation of an arbitrary amount of protein that is ultimately under the control of the experimenter. Moreover, the use of reversibly photoswitchable (e.g.: rsTagRFP[153], Dreiklang[154], Dronpa[155], mGeos[156]) or photoconvertible (e.g: Dendra[157], mKikGR[158], Kaede[159], PSmOrange[160] and the Eos family[161]) fluorescent proteins for PALM hampers their use in quantitative experiments as these proteins can emit their signal multiple times during an acquisition, which can lead to individual molecules being localized and counted more than once.

In order to circumvent these traditional limitations of PALM techniques and perform a truly quantitative version of PALM (qPALM), we engineered a specific qPALM-ready bacterial strain that we could use to study the expression and distribution of the AcrB protein with single-molecule precision. We chose to label the AcrB component of the AcrAB-TolC efflux pump as it had already been shown that C-terminal fusions to this protein do not compromise its function[162], while no protein fusions with the other components of the complex have yet been reported. We solved the problem of maintaining the original expression pattern of AcrB by fusing a fluorescent protein-coding sequence directly with the original *acrB* gene in the chromosome of *E. coli*, while taking a series of precautions to minimize unintended effects on the gene expression rate, which are explained in detail in the next sections.

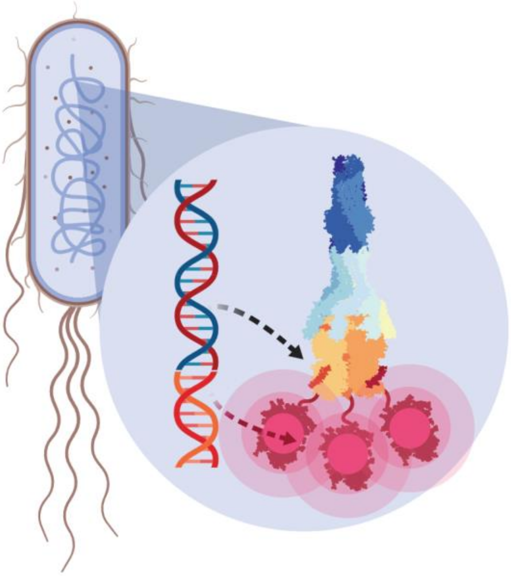

Figure 47. Simplified illustration of the labelling strategy employed in our study. The original acrB gene on the chromosome of E. coli was fused with a sequence encoding for the photoactivatable protein PAmCherry1 via genome editing. The resulting strain expresses a chimeric AcrB protein which is linked to PAmCherry1 through a short peptide link. As a functional AcrAB-TolC efflux pump contains three individual AcrB subunits, each pump expressed by our experimental strain is labelled with three fluorescent tags.

We tackled the problem of accurate protein counting by employing PAmCherry1 as a fluorescent marker, which is an irreversibly photoactivatable protein[26,30]. PAmCherry1 is expressed in a non-fluorescent state, which is converted into a fluorescent state upon exposure to violet light; after being converted, PAmCherry1 emits fluorescence until it permanently bleaches (Figure 48). As such, it is possible to accurately count every instance of PAmCherry1 within a given cell as long as some precautions are taken during imaging and image analysis, which are discussed in sections 5.2.2 and 5.2.3.

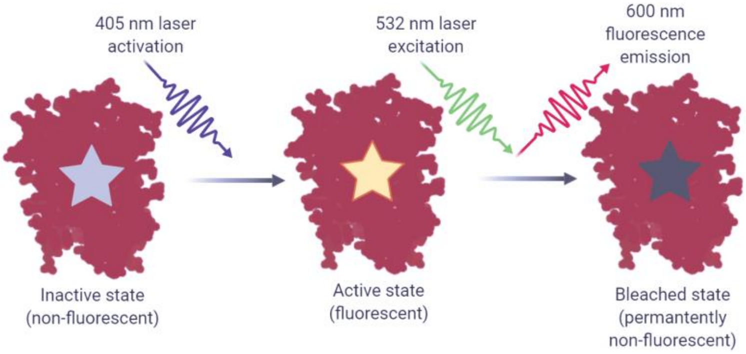

Figure 48. PAmCherry1 is expressed in a non-fluorescent state with an absorbance peak at around 400 nm. Upon excitation with this wavelength, a series of irreversible chemical changes occur to the fluorophore site of the protein, which were explained in detail in Figure 7. The end result is a red-emitting fluorescent protein which absorbs in the green spectral range. As it cannot convert back to the initial state, once activated PAmCherry1 remains fluorescent until eventually bleaching upon sustained excitation.

Performing qPALM on this bacterial strain allowed us to obtain otherwise inaccessible information regarding the spatial organization of AcrB both in planktonic and in biofilm-associated E. coli, to analyze the distribution of AcrB in bacterial populations, and to probe the short-term translational response of AcrB to external stimuli.

5.1 Development of an *ΩacrB::PAmCherry* E. coli strain

In order to perform quantitative PALM imaging as described in section 5, we engineered *E. coli* strain TV001 by creating a fusion between the native *acrB* gene and a codon-optimized coding sequence for PAmCherry1 in the chromosome of *E. coli* strain BW25113[163]. The native STOP codon at the 3' end of the *acrB* gene in *E. coli* strain BW25113 was replaced with the engineered PAmCherry1 sequence followed by a new STOP codon. We achieved this by employing a slight variation of the no-SCAR protocol by Reisch & Prather[164], which is a λ Red recombination-mediated genetic engineering approach (a.k.a. "recombineering"[165]) employing a CRISPR/Cas9 system to select for positive recombinants.

Section 5.1.1 will be an explanation of the mechanism of CRISPR/Cas9-assisted recombineering, while sections 5.1.2 and 5.1.3 will be a systematic description of the design and production process of *E. coli* strain TV001.

5.1.1 CRISPR/Cas9-assisted recombineering

Recombineering is a popular genome editing technique that allows for the insertion or removal of arbitrary sequences from virtually any locus of a bacterial replicon (be it the chromosome, a plasmid or any other replicative element) by using homologous recombination. Homologous recombination in recombineering approaches typically rely on non-bacterial recombination enzymes which need to be expressed transiently through an expression vector (e.g., a plasmid), and the most commonly used are the Exo, Beta and Gam proteins from bacteriophage λ Red[165]. These enzymes express their function in different ways: Exo and Beta recognize double-stranded linear DNA in the bacterial cytoplasm and bind to it, promoting its insertion within an active replication site on a bacterial replicon as an Okazaki fragment, while Gam prevents bacterial endogenous nucleases from destroying the exogenous dsDNA[166]. The insertion site of the exogenous DNA is determined by the regions of homology between the template and the bacterial replicon. This mechanism is shown in Figure 49.

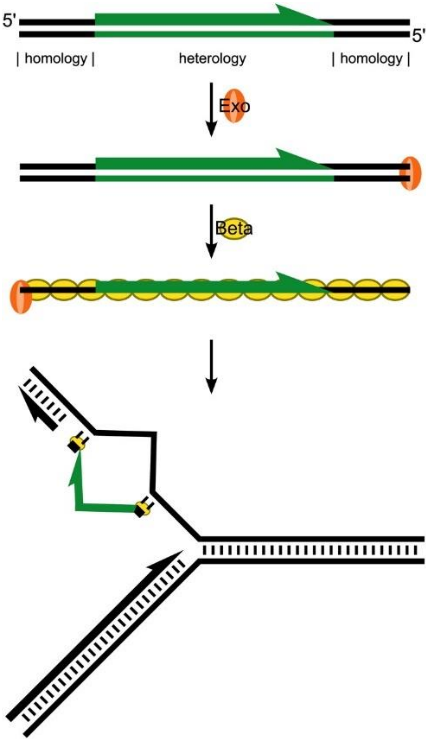

Figure 49. λ Red-mediated recombination mechanism. At first, one strand of linear dsDNA is completely digested by Exo (orange). Beta (yellow) then facilitates annealing of the remaining ssDNA to the lagging strand of the replication fork in place of an Okazaki fragment. The heterologous region (green) does not anneal to the genomic sequence. Image retrieved from [166].

In traditional recombineering approaches, the recombination template needs to harbor a selectable marker (e.g., an antibiotic resistance cassette) in order for recombinant bacteria to be selected. If the goal of a recombineering experiment is to insert a non-selectable feature such as a fluorescent protein coding sequence, the selectable marker needs to be removed afterwards. This is typically achieved by flanking the antibiotic resistance cassette in the recombination template either with two Flippase Recognition Target sequences (FRT), which trigger the removal of the flanked sequence upon induction of a plasmid-encoded flippase protein[163], or with two loxP sites, which achieve the same effect upon induction of a Cre protein[167,168]. This procedure, however, leaves a so-called "scar" sequence where the original selectable marker was located, as the two FRT sequences are not removed by flippase activity (Figure 50).

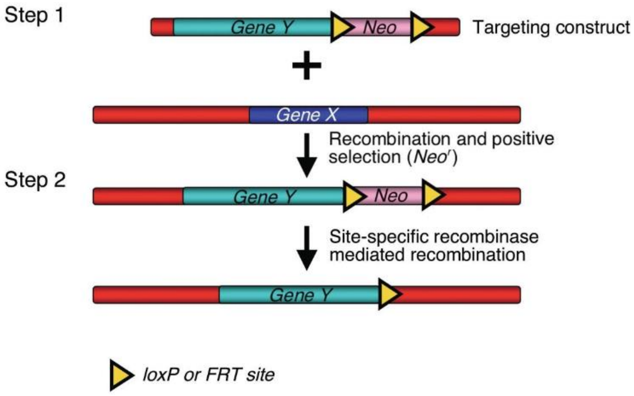

Figure 50. In step 1, a non-selectable DNA fragment (Gene Y) is introduced along with a selectable marker, Neo, which is flanked by loxP or FRT sites. Recombinants are selected for the presence of Neo. In step 2, Neo is deleted by site-specific recombinase mediated recombination (Cre for loxP sites and Flp for FRT sites). A single loxP or FRT "scar" site is retained after recombination. Image and caption retrieved from [165].

Other recombineering approaches exist which avoid the problem of scar sequences in different ways. For example, it is possible to perform a two-step recombination in which at fist only a so-called "landing pad" containing an antibiotic resistance cassette is inserted in the bacterial replicon. This is followed by a second recombination in which the landing pad is replaced with the intended insert, which can be selected by screening recombinant colonies for the loss of antibiotic resistance[169] (Figure 51).

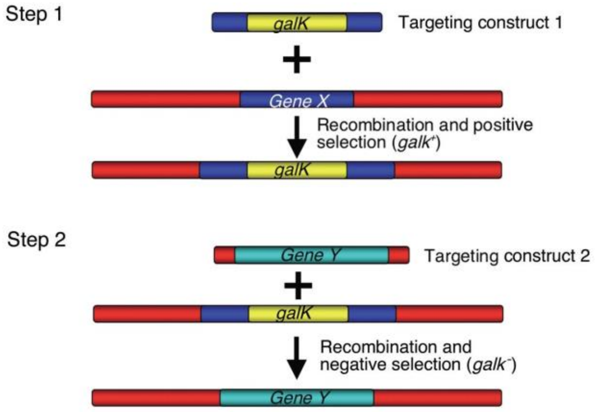

Figure 51. In this two-step method, first the selectable galK marker is targeted to the site (Gene X) where the non-selectable DNA fragment (Gene Y) is to be inserted. In the second step, a targeting construct containing the non-selectable DNA fragment flanked by the same regions of homology to the target site is transformed into Gal+ bacterial cells containing the recombinant DNA from step 1. Clones in which the Gene Y DNA fragment is correctly inserted can be counter-selected for loss of the galK gene. Image and caption retrieved from [165].

However, this procedure carries the inherent problem of producing a potentially unstable "intermediate" strain before the second recombination is carried out: if the landing pad insertion disrupts an essential gene in the host, the cells cannot survive the first recombination and this approach becomes unfeasible.

Quicker, single-step approaches that do not require the recombination of any selectable marker are the CRISPR/Cas9-assisted recombineering techniques. A few variations exist[170,171], but they all rely on the same principle: λ Red-mediated recombination of non-selectable DNA sequences is followed by the induction of a CRISPR/Cas9 system that selectively kills non-recombinant bacteria by causing double-strand breaks (DSBs) in their chromosome (Figure 52).

Cas9 is a bacterial RNA-guided DNA endonuclease, which can express its function only when bound to specific RNAs forming a ribonucleoprotein complex. A Cas9-binding RNA is called a "guide RNA", as it serves as a sequence recognition domain for the complex: when Cas9 finds a DNA sequence which perfectly matches with the 20-bp "spacer" region of its guide RNA, it cleaves it creating a double-strand break. Cas9 is able to recognize virtually any 20-bp sequence (which takes the name of "protospacer"); however, it is able to cleave the DNA only if the target sequence is followed by a so-called "Protospacer Adjacent Motif" site (PAM site), a three-base sequence of NGG where N can be any nucleotide[172].

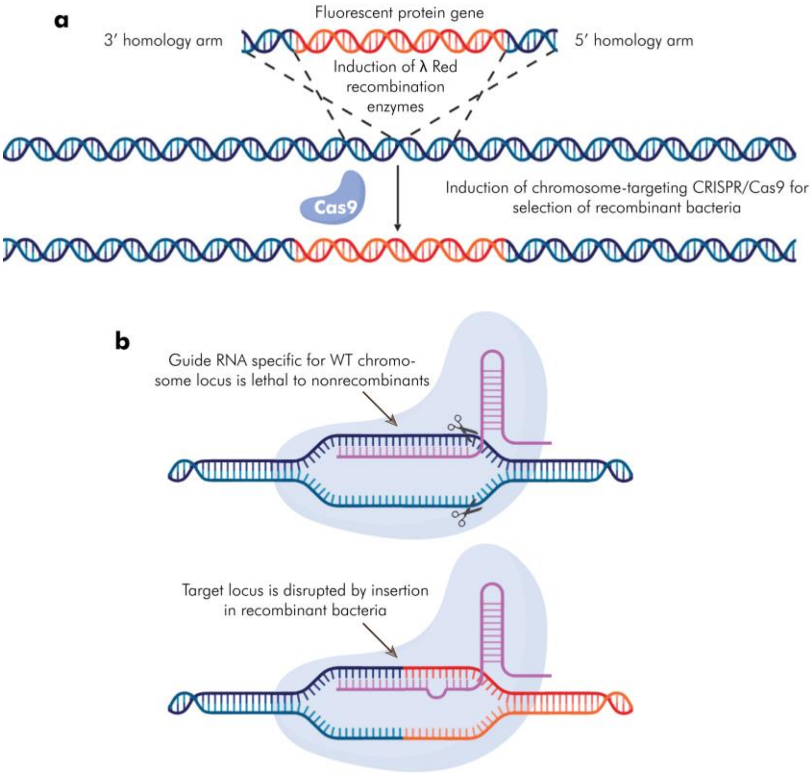

Figure 52. (a) Overview of a CRISPR/Cas9-assisted recombineering method. First, a non-selectable dsDNA fragment is inserted in the desired genomic locus via homologous recombination. Then a CRISPR/Cas9 system targeting the original recombination locus is induced, killing the nonrecombinant bacteria via double strand break of their DNA. (b) Schematic showing the Cas9 activity in recombinant (bottom) versus nonrecombinant (top) bacteria. The guide RNA associated with Cas9 is complementary to a specific locus in the chromosome of the wild type (WT) bacteria: this causes Cas9 to recognize that sequence and

expressing its endonuclease activity. When the target is disrupted by the insertion of foreign DNA, Cas9 is no longer able to recognize the original locus and the bacteria survive. The 10-12 bases closest to the PAM site (the so-called "seed" region") are known to be crucial for target recognition by Cas9[173]*, and a single mutation in that sequence may be enough to prevent DNA cleavage. However, disrupting the original PAM site is the most effective method to achieve that.*

The recombineering approach we decided to pursue was the no-SCAR method by Reisch and Prather[164], as mentioned in the previous section. This approach was relatively simpler than the other CRISPR/Cas9-assisted recombineering methods, as they managed to condensate all the molecular machinery necessary for both homologous recombination and recombinant selection into two neatly organized plasmids (pCas9-CR4 and pKDsgRNA). The detailed workflow of this technique will be described in the following sections.

5.1.2 Design and amplification of the recombination template

A priority in the design of our fluorescent construct was that of minimizing unintended effects on the transcription and translation rate of the engineered gene and of the acrAB operon as a whole. The insertion of a foreign sequence can drastically modify the expression rate of a gene if not properly designed; especially, adding codons that are rarely present in the host genome can lead to bottlenecks during translation due to lack of the relevant aminoacyl-tRNA[174]. The relative prevalence of different synonymous codons in an organism's DNA is called the "codon bias" of that organism[175], and needs to be taken into account when designing an expression construct. Moreover, a bias in the pairing of neighboring codons called "codon context" has been proven to play a significant role in determining the translation rate of coding sequences[176–178]. As such, we employed the web-based multi-objective optimization tool "Codon

Optimization On-Line (COOL)” (http://cool.syncti.org/)[179] to optimize both codon bias and codon context of our PAmCherry1 sequence for its expression in *E. coli*.

We first obtained the coding sequence for PAmCherry1 from plasmid pBAD/HisB-PAmCherry1 (https://www.addgene.org/31931/). Despite it being a bacterial expression vector the protein coding sequence appeared to be poorly optimized for expression in E. coli, which resulted in 48.51% of codons (19.5% of bases) being modified after optimization with the COOL web server. Figure 53 shows the sequences before and after optimization.

```
GTGAGCAAGGGCGAGGAGGATAACATGGCCATCATTAAGGAGTTCATGCGCTTCAAGGTGCACATGGAGGGGTCCGTGAACGGCCACGTGTTCGAGATCG
    template sequence PAmCherry1 (not optimized)
GTTAGCAAAGGCGAAGAAGATAACATGGCGATCATCAAAGAATTTATGCGTTTCAAAGTGCATATGGAAGGTTCTGTTAACGGCCACGTTTTTGAAATCG
    aligned sequence PAmCherry1 (codon optimized)

AGGGCGAGGGCGAGGGCCGCCCCTACGAGGGCACCCAGACCGCCAAGCTGAAGGTGACCAAGGGTGGCCCCCTGCCCTTCACCTGGGACATCCTGTCCCC
    template sequence PAmCherry1 (not optimized)
AAGGGGAAGGCGAAGGTCGTCCGTATGAAGGTACTCAGACCGCGAAATTGAAAGTCACCAAAGGCGGTCCGCTGCCGTTCACCTGGGATATTCTGTCTCC
    aligned sequence PAmCherry1 (codon optimized)

TCAATTCATGTACGGCTCCAATGCCTACGTGAAGCACCCCGCCGACATCCCCGACTACTTTAAGCTGTCCTTCCCCGAGGGCTTCAAGTGGGAGCGCGTG
    template sequence PAmCherry1 (not optimized)
GCAGTTCATGTACGGCAGCAACGCCTATGTGAAACACCCGGCAGACATCCCGGACTACTTCAAACTGAGCTTCCCTGAAGGCTTTAAATGGGAACGCGTA
    aligned sequence PAmCherry1 (codon optimized)

ATGAAATTCGAGGACGGCGGCGTGGTGACCGTGACCCAGGACTCCTCCCTGCAGGACGGTGAGTTCATCTACAAGGTGAAGCTGCGCGGCACCAACTTCC
    template sequence PAmCherry1 (not optimized)
ATGAAATTCGAAGACGGTGGCGTGGTGACCGTTACCCAGGACAGCAGCCTGCAGGATGGTGAGTTCATCTACAAAGTTAAACTGCGTGGCACCAACTTCC
    aligned sequence PAmCherry1 (codon optimized)

CCTCCGACGGCCCCGTAATGCAGAAGAAGACCATGGGCTGGGAGGCCCTCTCCGAGCGGATGTACCCCGAGGACGGCGCCCTGAAGGGCGAGGTCAAGCC
    template sequence PAmCherry1 (not optimized)
CGTCTGACGGCCCGGTGATGCAGAAAAAAACCATGGGCTGGGAAGCGCTGTCCGAGCGTATGTATCCGGAAGACGGCGCACTGAAAGGTGAAGTTAAGCC
    aligned sequence PAmCherry1 (codon optimized)

GAGAGTGAAGCTGAAGGACGGCGGCCACTACGACGCTGAGGTCAAGACCACCTACAAGGCCAAGAAGCCCGTGCAGCTGCCCGGCGCCTACAACGTCAAC
    template sequence PAmCherry1 (not optimized)
GCGTGTGAAGCTGAAAGATGGCGGTCACTACGATGCGGAAGTGAAAACCACCTATAAAGCGAAGAAACCGGTTCAGCTGCCGGGCGCTTACAACGTGAAC
    aligned sequence PAmCherry1 (codon optimized)

CGCAAGTTGGACATCACCTCACACAACGAGGACTACACCATCGTGGAACAGTACGAACGTGCCGAGGGCCGCCACTCCACCGGCGGCATGGACGAGCTGT
    template sequence PAmCherry1 (not optimized)
CGTAAACTGGATATCACCAGCCACAACGAAGATTACACCATCGTTGAACAGTACGAACGTGCTGAAGGCCGTCACTCTACCGGTGGTATGGATGAACTGT
    aligned sequence PAmCherry1 (codon optimized)

ACAAG
    template sequence PAmCherry1 (not optimized)
ACAAA
    aligned sequence PAmCherry1 (codon optimized)
```

Figure 53. Sequence alignment between the PAmCherry1 sequence contained in the bacterial expression plasmid (template) and the PAmCherry1 sequence we obtained via codon usage and codon context optimization for E. coli (query). Bases that were replaced during optimization are highlighted.

As explained in section 5.1.1, in order to be recombined in a specific genomic locus by the λ Red enzymes, the exogenous DNA needs to be flanked by two "homology arms" (HAs) – i.e. sequences that pair exactly with the specific region on the bacterial chromosome in which recombination needs to occur.

Longer exogenous sequences need longer HAs in order to be efficiently recombined[165]. As such, we inserted a 214-bp HA at the 5' and a 272-bp HA at the 3’ of the codon-optimized PAmCherry sequence. The 5’ and 3’ HAs were homologous to, respectively, the last 214 bases of the native *acrB* gene on the chromosome of BW25113 (excluding the STOP codon) and the first 272 bases following the original STOP codon. Moreover, the 5’ HA was linked to the PAmCherry coding sequence with 9 additional bases encoding for a Gly-Gly-Gly flexible peptide. This same linker design was successfully employed by Yamamoto *et al.*[162] for a C-terminal protein fusion between AcrB and GFP.

Ultimately, in the design of our recombination template we had to take into account the need for selectability through a CRISPR/Cas9 system. As explained in section 5.1.1, a gRNA-Cas9 complex can only express its endonuclease activity if the target sequence is followed by a PAM site. The most convenient PAM site in our case occurred at position 3129-3130 of the acrB coding sequence, close to the STOP codon, and this site was included in the 5’ HA of our recombination template. We disrupted the PAM site in the 5’ HA by switching the cytosine (C) at position 3129 with a thymine (T), which changed codon n°1043 into a synonymous codon encoding for serine (AGC->AGT). As such, the recombination template would not be susceptible to Cas9’s endonuclease activity.

The engineered recombination template, as shown in Figure 54, was commissioned as a 1203 bp-long double-stranded DNA fragment (GeneStrand) to Eurofins Genomics (https://www.eurofinsgenomics.eu/).

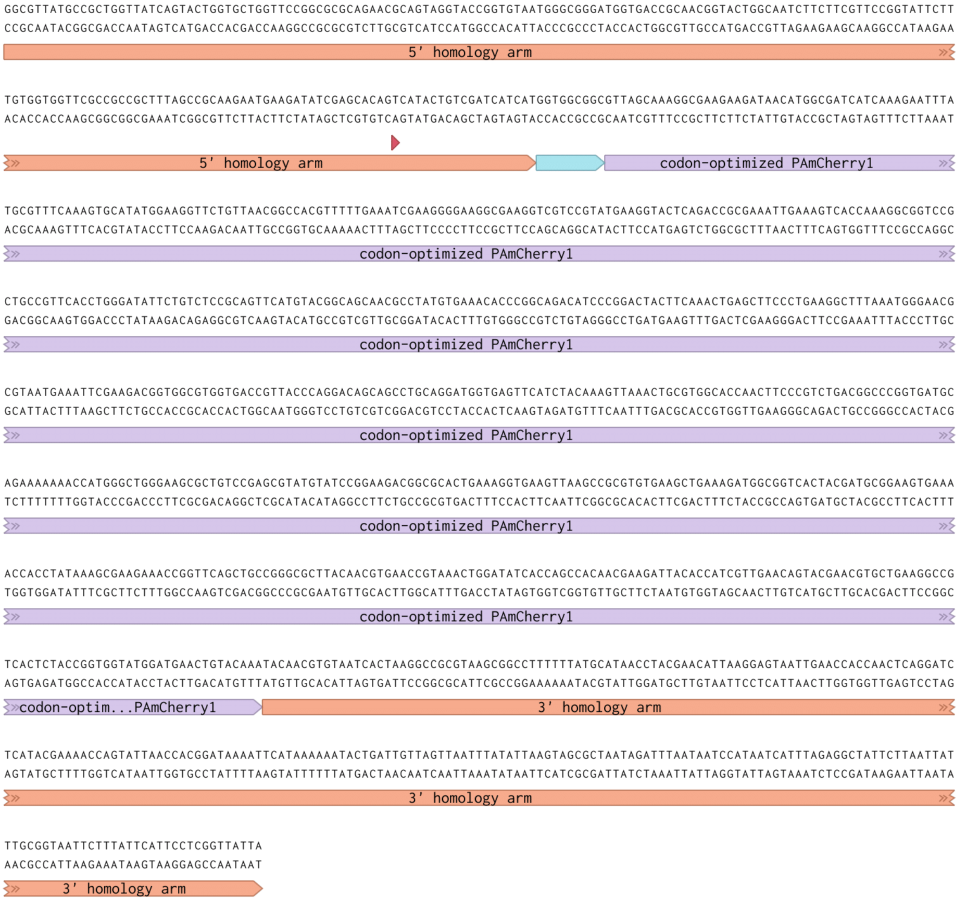

Figure 54. Sequence of the GeneStrand used as a recombination template. The 5’ homology arm is identical to the last 214 bases of the acrB coding sequence as found on the E. coli BW25113 chromosome, with the exception of a C->T mutation in position 2139 (red arrowhead). The light blue segment indicates the sequence encoding for the Gly-Gly-Gly linker peptide. The 3’ homology arm starts with the original stop codon of the acrB gene and continues with the 3’ untranslated region, which contains the terminator sequence.

However, GeneStrands are provided by Eurofins in the form of 300 nanograms of lyophilized double-stranded DNA. This amount is intended for plasmid cloning purposes and it is barely enough to perform a single recombination attempt in *E. coli*; therefore, we devised a method to amplify the GeneStrand sequence indefinitely. We engineered a commercial expression vector to act as a platform to replicate the GeneStrand in bacteria, after which we could easily obtain large amounts of dsDNA template to use in the recombination procedure. The detailed procedure is described in appendix 7.

5.1.3 Creation of E. coli strain TV001

We employed the "no-SCAR" protocol[164] to engineer *E. coli* strain TV001 from strain BW25113. As mentioned in section 5.1.1, this technique relies on the use of two plasmids, harboring both the recombination machinery (λ-Red based) and the CRISPR/Cas9-based selection system. The CRISPR guide RNA (sgRNA), which acts as the "homing system" of the Cas9 warhead, needs to be expressly coded on the plasmid in order for it to target the correct sequence on the bacterial genome. As such, the plasmid containing the sgRNA sequence needs to be modified according to the specific site one wants to target.

After retargeting the sgRNA, both plasmids are inserted into the desired bacterial strain and the recombination machinery is chemically induced, followed by the introduction of the external DNA fragment into the bacteria via transformation. After introducing the foreign sequence, the CRISPR/Cas9 counter-selection system is activated and the bacteria that did not undergo recombination at the correct genomic locus are killed via double-strand break of their DNA.

A detailed protocol of the whole procedure, along with some considerations on the reasons of specific passages, is reported in appendix 7. Figure 55 shows a schematization of the process.

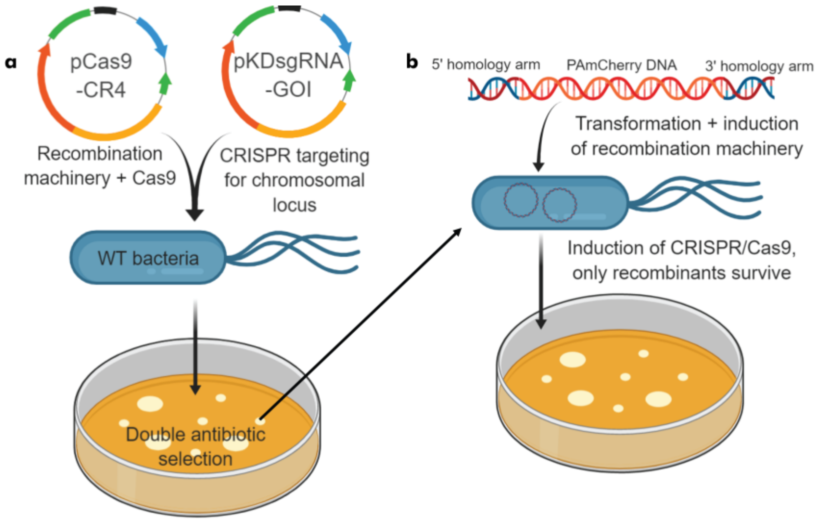

Figure 55. (a) The two plasmids encoding for the recombination/selection machinery are transformed in the desired bacterial strain and selected for their respective antibiotic resistance genes. (b) A single transformant colony is picked, grown while inducing the recombination machinery, and transformed with the linear dsDNA containing the insert. After transformation, the bacteria are plated on dishes containing an inductor of the CRISPR/Cas9 system (anhydrotetracycline) to select for positive recombinants.

After successfully editing the genome of *E. coli* BW25113 obtaining strain TV001, the two plasmids used for the recombination process had to be removed. pKDsgRNA-acrB was cured from *E. coli* TV001 by culturing the cells in LB medium without antibiotic selection at 37°C, taking advantage of the temperature-sensitive origin of replication of the plasmid. pCas9-CR4 was subsequently removed via replica plating[180], by growing the cells in the absence of antibiotics and selecting colonies for their loss of resistance against chloramphenicol.

The functionality of the fluorescently labelled AcrB protein expressed by TV001 was verified by measuring the minimal inhibitory concentration (MIC, which is the lowest concentration of an antimicrobial drug that will prevent the visible growth of a microorganism after overnight incubation) of chloramphenicol, an antibiotic that is a specific substrate of AcrB, via the microdilution method in LB medium[181]. Growth of the acrB-PAmCherry strain was tested at different chloramphenicol concentrations, alongside the wild-type BW25113 strain and two deletion mutants (*ΔacrB*[182] and *ΔtolC*[182]). The measured MIC for both the acrB-PAmCherry strain and the WT strain was 8 µg/ml while both deletion mutants could not grow at chloramphenicol concentrations of 2 µg/ml or higher (Figure 56).

N.B.: chloramphenicol was also employed for plasmid selection during the process of creating strain TV001, as described in section 5.1.3. However, the antibiotic concentration used for selection (25 µg/ml) was already known to be sufficient to prevent the growth of *E. coli* harboring a working efflux pump, as this concentration is commonly used for plasmid selection.

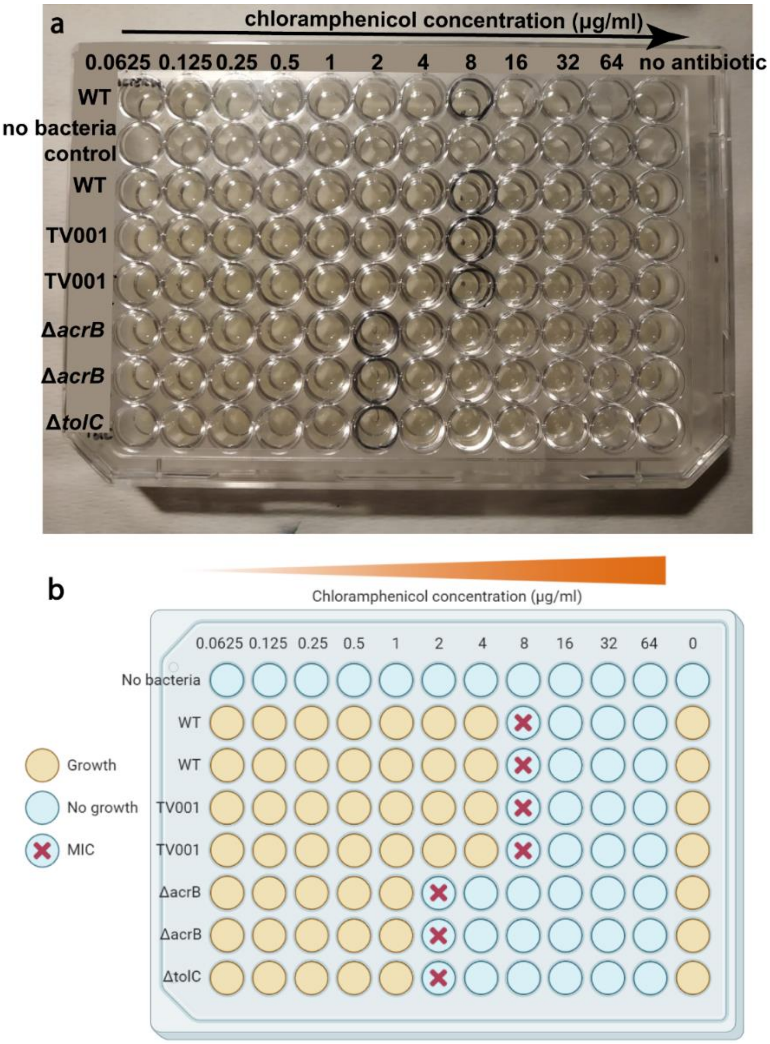

Figure 56. (a) Photo of the 96-well plate used for the microdilution experiment. Each well contains LB medium with a chloramphenicol concentration indicated by the respective column header, and a bacterial inoculum indicated by the row. Black marker circles highlight the minimal concentration of chloramphenicol for each row at which no bacterial growth is visible. The MIC for both TV001 and wild-type bacteria is 8 µg/ml, while the MIC for both efflux pump mutants is 2 µg/ml. The image was taken after an overnight incubation (~16 hours). (b) Schematization of the results.

The *E. coli* strain obtained at the end of this process represents an ideal system in which to perform quantitative PALM as described in section 5. It expresses a fluorescent version of AcrB from the native chromosomal locus, which keeps the translation rate and conditions as close to the original as possible; furthermore, codon optimization of the label sequence minimizes unwanted translational effects. The photoactivatable PAmCherry moiety also displays an ideal photochemical behavior, as its irreversible photoactivation followed by bleaching means that the same protein cannot appear at separate times during a PALM acquisition and thus cannot be mistakenly counted more than once. As stated in section 5, performing quantitative PALM on such a strain would provide unique information about the expression and distribution (both within single cells and in a population context) of AcrB in a variety of conditions and on short timescales.

5.2 Quantitative imaging of AcrB in planktonic and biofilm-associated bacteria

As explained in section 4.2, the role of efflux pumps in bacterial biofilms is still a largely unexplored subject. Therefore, we set forth to shed light on this phenomenon by performing qPALM on our engineered bacterial strain in order to compare AcrB expression patterns in planktonic and biofilm-associated growth conditions.

In sections 5.2.1 to 5.2.4, I will describe the experimental procedures we employed to prepare and image planktonic bacterial samples as well as biofilms, and to analyze the resulting data.

5.2.1 Preparation of bacterial samples

In order to compare data obtained from bacteria grown in two different conditions, it was crucial to minimize differences in sample preparation apart from the growth condition itself (planktonic and biofilm-associated). Since our *E. coli* strain does not form biofilms in common Lysogeny Broth (LB) but requires a nutrient-limiting environment, minimal medium (M9) with added glucose as a carbon source was used to grow bacteria for the preparation of both planktonic and biofilm samples. A peculiar advantage of using M9 medium instead of LB is that the former is completely transparent and does not emit any measurable fluorescence in our imaging conditions. LB, on the other hand, is noticeably fluorescent on account of containing a complex mixture of proteins and cellular extracts (yeast), which can generate noise in fluorescence microscopy experiments if the samples are not thoroughly washed prior to imaging.

Moreover, it has been shown that growth medium composition plays a significant role in determining the expression levels of *acrB*, *marA* and other genes involved in the efflux activity of *Escherichia coli*[145]. As many pathogenic bacteria experience a nutrient-limiting environment in their hosts, it has been suggested that in vitro experiments designed to study the expression of clinically relevant genes should be performed in minimal medium[145].

A detailed protocol for the preparation of both planktonic and biofilm samples can be found in appendix 7.

5.2.2 Quantitative PALM imaging procedure

We performed qPALM with the optical setup described in section 3.1.1, by using the 532 nm laser line for fluorescence excitation and the 405 nm laser line for the photoactivation of PAmCherry1, using a standard HILO configuration ($\theta_r = 77°$, $R = 40$ µm). The fluorescence signal coming from PAmCherry1 was acquired after passing through a bandpass filter (central wavelength: 595 nm, bandwidth: 60 nm).

After centering the field of view on a region on the coverslip with several, well-separated bacteria, the fluorescent proteins in the cells were gradually photoactivated and their fluorescence recorded in the course of a 1000-frames-long movie. The length of the movie was sufficient to observe a complete photoactivation and subsequent bleaching of the fluorophores before the recording ended. We found that a continuous exposure to low-intensity violet light (~0.7 W/cm^2) provided a steady activation of well-resolved fluorophores in E. coli TV001. This photoactivation behavior was not observed in wild-type E. coli BW25113 in the same imaging conditions, where the only detected fluorescence consisted in a very low level of autofluorescence not associated with violet light excitation.

A detailed protocol of the imaging procedure can be found in appendix 7.

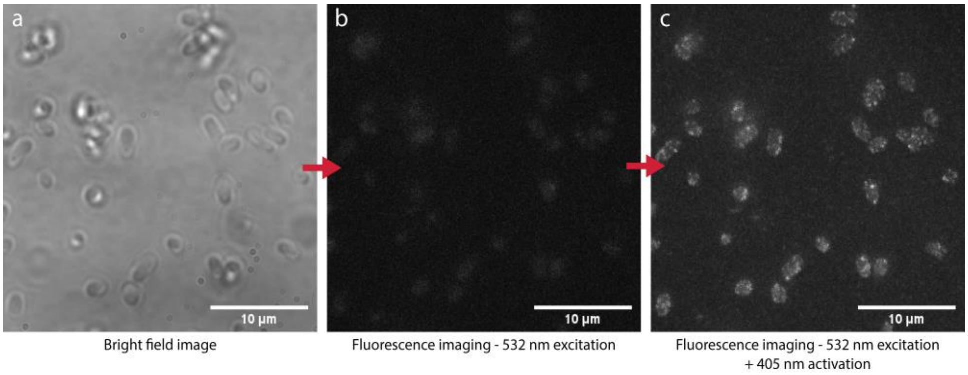

Figure 57. Schematization of the qPALM acquisition process. (a) A bright field image of a region of the sample where several bacteria are visible is acquired (in this case, a planktonic bacterial sample). (b) Without moving the sample, the illumination is switched from bright field to fluorescence excitation at 532 nm. The outlines of bacteria are still visible due to their dim autofluorescence. (c) While maintaining 532 nm illumination, the sample is irradiated with a 405 nm laser which activates the PAmCherry1 fluorophores present in the bacteria, and a PALM movie is acquired. Image (c) is a maximum intensity projection obtained from a full 1000-frames-long PALM movie.

It is important to note that biofilm specimens are especially difficult to image with single-molecule techniques, due to the samples being thick, composed in large part of a highly scattering matrix, and strongly autofluorescent. By employing the HILO illumination technique, we were able to effectively localize individual proteins up to 15 µm from the glass/biofilm interface, which made it possible to acquire data on AcrB expression in an area of the biofilm which is defined as the "core"[132].

The procedure employed for imaging biofilms differs slightly from the one used to image planktonic samples. The image acquisition process is exactly the same (as reported in appendix 7), but the process of selecting a field of view is carried out in the following way:

- At first, the piezoelectric stage translator is set to zero in both the x and y axes, and a field of view is selected on the coverslip plane in an area with several clearly distinguishable bacteria by moving the stage via the mechanical controllers.
- After performing qPALM, the second field of view is selected by moving the piezoelectric translator to -50 µm in both the x and y axes. As biofilms are extremely crowded samples and it is often hard to locate several clearly discernible cells in any given point, the focus is adjusted along z within 15 µm from the coverslip until a suitable area is chosen for imaging.
- From this point, after imaging each field of view, the next one is selected by moving the piezoelectric translator by 50 µm steps in a 3x3 grid centered around the first field of view. In every instance, the focus is adjusted within a 15 µm range in order to find a suitable area.

Therefore, the output of a qPALM imaging session on a biofilm sample consists in 9 image stacks acquired at different z depths within a 15 µm range from the coverslip. The results reported in section 5.2.4 (Figure 60) on the number of AcrB-PAmCherry copies per cell refer to an average between bacteria imaged over this depth range.

5.2.3 Reconstruction of super-resolved localization maps

The movies acquired during imaging were processed with the ThunderSTORM software as described in section 2.2.2 in order to localize individual fluorescent proteins in the images. The exact parameters used for the analysis of PAmCherry1 images differ slightly from the ones used for Alexa Fluor dyes, mainly due to the lower brightness of the former, and are displayed in Figure 58.

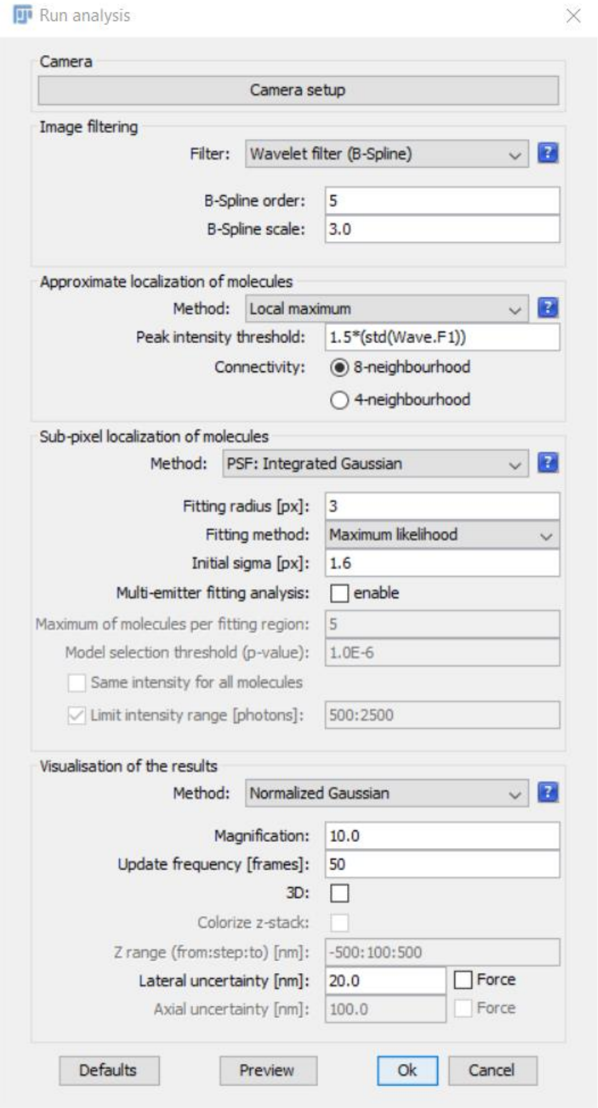

Camera

Image filtering
Filter: Wavelet filter (B-Spline)
B-Spline order: 5
B-Spline scale: 3.0

Approximate localization of molecules
Method: Local maximum
Peak intensity threshold: 1.5*(std(Wave.F1))
Connectivity: ● 8-neighbourhood
○ 4-neighbourhood

Sub-pixel localization of molecules
Method: PSF: Integrated Gaussian
Fitting radius [px]: 3
Fitting method: Maximum likelihood
Initial sigma [px]: 1.6
Multi-emitter fitting analysis: ☐ enable
Maximum of molecules per fitting region: 5
Model selection threshold (p-value): 1.0E-6
☐ Same intensity for all molecules
☑ Limit intensity range [photons]: 500:2500

Visualisation of the results
Method: Normalized Gaussian
Magnification: 10.0
Update frequency [frames]: 50
3D: ☐
Colorize z-stack: ☐
Z range (from:step:to) [nm]: -500:100:500
Lateral uncertainty [nm]: 20.0 ☐ Force
Axial uncertainty [nm]: 100.0 ☐ Force

Figure 58. ThunderSTORM UI showing the parameters used for the reconstruction of a typical PALM image of bacteria expressing PAmCherry1.

An important issue that required careful calibration in the analysis of qPALM data was that of "merging" of neighboring fluorescent molecules. As we explained earlier, PAmCherry exhibits an ideal photochemical behavior for molecule counting, as it cannot reversibly switch from a fluorescent to a non-fluorescent state. This way it is impossible for the same protein to emit fluorescence at separate times during a movie acquisition; however, it is not impossible for a molecule to emit fluorescence for a time longer than the frame integration time, which results in a fluorescent spot appearing for two or more consecutive frames. ThunderSTORM gives the user the option to “merge” in post-processing individual molecules that are localized close together in different frames, within a distance threshold that can be defined by the user. As the localization precision for the position of individual molecules in our qPALM experiments was ~20 nm (calculated on single frames by ThunderSTORM using Equation 2), we opted for a distance threshold of 40 nm. Which means that molecules appearing within 40 nm of each other in consecutive frames were considered to be the same molecule. There is a risk that two different copies of PAmCherry located at a distance of less than 40 nm from each other (for example because they are part of a functional trimer in the same efflux pump) are activate exactly at the same time or in consecutive frames, which would lead to merge them into one and to an underestimation of the real number. However, the intensity of the activation laser was finely tuned to promote the activation of a small number of fluorophores per cell at any given time, so we considered this risk to be negligible.

5.2.4 Quantification of AcrB-PAmCherry copies per cell

The data we were interested in obtaining from our qPALM experiments was the amount of AcrB-PAmCherry instances present in individual bacterial cells. As such, the super-resolved molecular maps obtained in section 5.2.3 had to be further processed in order to assign each localized protein to a specific bacterium.

The bright field reference images acquired as part of the imaging procedure described in section 5.2.2 were manually segmented in order to obtain the external borders of the bacterial cells being imaged. In practice, a Wacom

Intuos 4 graphic tablet was employed in conjunction with the “lazo” tool on ImageJ to accurately trace ROIs around the membrane of individual bacteria present in each of the bright field images. Only clearly visible and isolated bacteria which were lying flat on the glass surface were selected for tracing. Around 10-20 bacteria were segmented per image. The ROIs were then checked against the localization maps reconstructed by ThunderSTORM and manually realigned to correct for possible lateral drifts which may have occurred between bright field and fluorescence acquisitions. Ultimately, the ROIs were combined and converted into a mask with the ImageJ “Create Mask” function and the resulting black and white image was saved in tiff format (Figure 59).

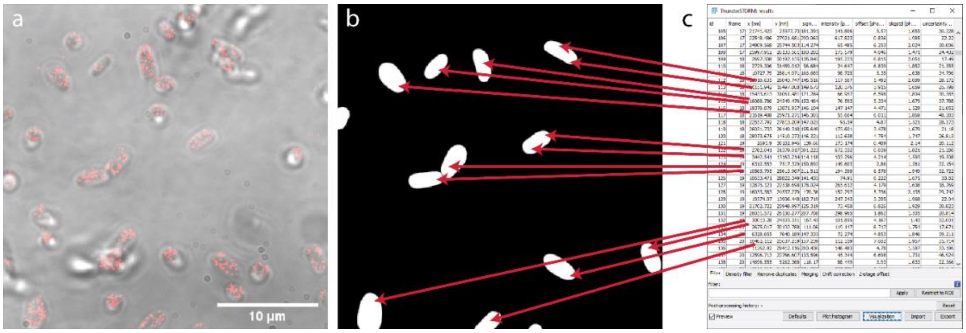

Figure 59. A brightfield reference image (a, planktonic bacteria in this example) is manually segmented in order to generate a binary mask (b) outlining individual bacterial cells. Only well-separated cells which are lying flat on the coverslip are segmented. Afterwards, the molecular coordinates generated by the ThunderSTORM analysis (c) are assigned to their respective bacterium in the image in order to quantify the amount of AcrB-PAmCherry copies per cell.

After creating a mask for each qPALM dataset, both the masks and the respective ThunderSTORM output (set of localization coordinates) were loaded in a MATLAB workspace and processed with a custom-made pipeline in order to assign each localized fluorescent protein to a specific bacterial cell. For each qPALM dataset, the pipeline outputs a list of *n* values, where *n* is the number of segmented bacteria in the mask, and each value indicates the number of fluorescent molecules localized within a specific bacterial cell.

Our results are reported in Figure 60, while in Figure 61 two qPALM images acquired respectively in a planktonic sample and in a biofilm can be compared.

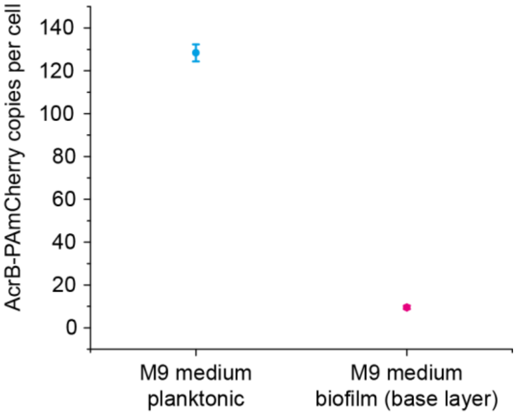

Figure 60. Average copy number of AcrB-PAmCherry observed in planktonic and biofilm-associated bacterial cells. The values represent averages between 207 (planktonic) and 220 cells (biofilm). Error bars represent the standard errors of the mean.

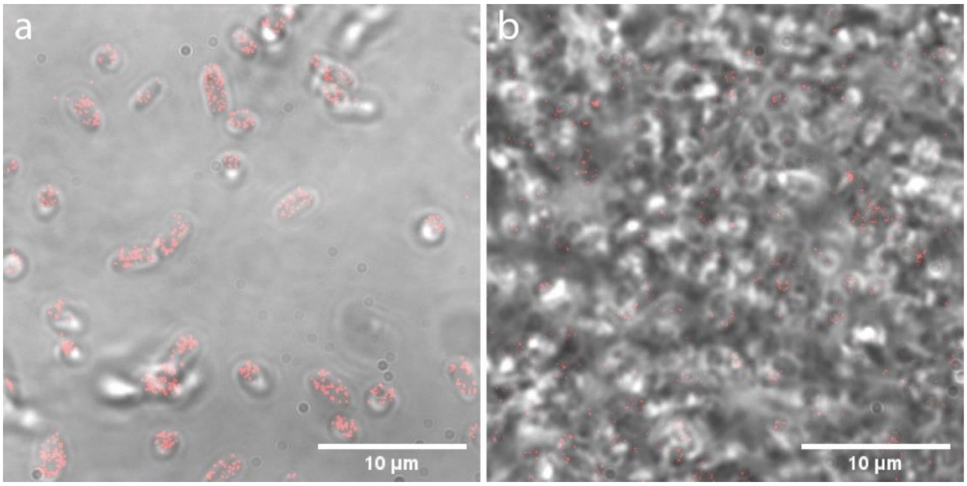

Figure 61. (a) Bright field reference image of a planktonic bacterial sample with a superimposed map of localized AcrB-PAmCherry proteins (red dots). (b) Bright field reference image and superimposed localization map of a biofilm sample.

As described in the biofilm imaging procedure (section 5.2.2), the value of AcrB-PAmCherry copies per cell reported for the biofilm samples consists in an average between individual bacteria imaged within a range of 15 µm starting from the glass/biofilm interface.

We were able to quantify an average of 128±4 instances of AcrB-PAmCherry in our homogeneous populations of planktonic bacteria, while the bacteria in the observable sections of the biofilm specimens contained an average of 9.5±0.9 fluorescent proteins. This finding was surprising, as efflux pumps such as AcrAB-TolC are known to play important functions in biofilms as discussed in 4.2. However, this could be explained either by assuming temporal inhomogeneities in the expression of AcrB (i.e.: the gene is expressed only at specific moments during biofilm growth), spatial inhomogeneities (i.e.: the gene is expressed only in specific regions of the biofilm, or in specific subpopulations of bacteria), or both. In any case, we could determine that a large difference exists in the general expression pattern of this efflux pump between free-swimming and biofilm-associated *E. coli* that was previously unobserved.

5.3 Using qPALM to elucidate the mechanism of action of a novel efflux pump inhibitor

Another opportunity to apply our strain and technique to tackle a real biological problem came from a collaboration between our group and the groups of Enrico Casalone (Department of Biology, University of Florence) and Elisabetta Teodori (NEUROFARBA, University of Florence). They had characterized a piperazine compound, namely 1-benzyl-1,4-diazepane (1-BD) (Figure 62), as an inhibitor of RND efflux pumps in *E. coli*. More specifically, they found out that 1-BD acts as a synergistic enhancer of the antimicrobial action of antibiotics which are specific substrates of the AcrAB and AcrEF pumps, such as levofloxacin[183]. Moreover, they had proof that 1-BD promotes the intracellular accumulation of ethidium bromide (EtBr), which again is a specific substrate of RND efflux pumps. What remained unclear was the mechanism of action of 1-BD: the observed effects could be explained both by a direct action of the compound on the efflux pump proteins (i.e. inhibiting the function) or by an effect of 1-BD on the regulation of the efflux pump genes (i.e. inhibiting the expression).

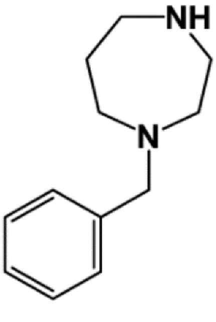

Figure 62. Structural formula of 1-BD.

We devised a qPALM experiment that would answer this question.

First, we performed a calibration experiment to determine the minimal time that needs to elapse before we are able to observe a variation in the expression of AcrB-PAmCherry through qPALM, after a stimulus is given to the bacteria. We incubated TV001 bacteria with sodium salicylate – which is known to induce the expression of *acrAB* by disrupting the MarR-mediated repression of the operon – and counted the number of AcrB-PAmCherry instances per bacterial cell through qPALM at different time intervals for 2 hours, comparing the salicylate-exposed bacteria with unexposed controls. Aliquots of incubating cells were harvested and fixed every 30 minutes, and qPALM imaging was performed on the following day. The exact procedures for sample preparation, qPALM imaging and data analysis are analogous to those described in sections 5.2.1 to 5.2.4. Figure 63 shows the result of our calibration experiment. The plotted values represent the ratio $N_{treated}/N_{control}$ between the average amount of fluorescent proteins localized in salicylate-exposed bacteria over the average amount localized in unexposed controls at each time point. The error bars represent the standard errors of the mean, propagated from the standard errors associated to $N_{treated}$ and $N_{control}$.

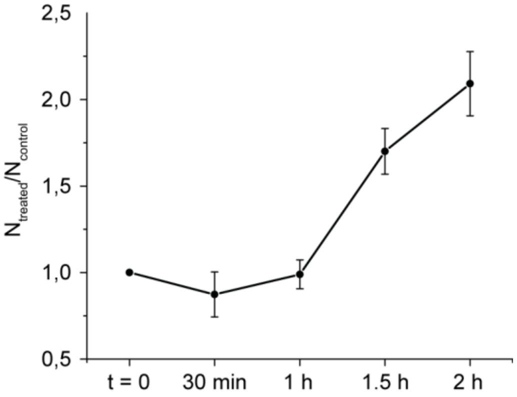

Figure 63. Ratio between the average AcrB-PAmCherry copy number per cell observed in salicylate-treated bacteria over the one observed in untreated controls, during the course of 2 hours after exposure to salicylate.

The calibration experiment showed that an increase in the expression of AcrB-PAmCherry was clearly visible after 1.5 hours of incubation with sodium salicylate with respect to the controls, and this delay is likely due to the maturation time of the fluorescent moiety of AcrB-PAmCherry.

This data suggested that the minimal wait time after a stimulus required to observe an expression variation of AcrB-PAmCherry via qPALM was between 1 and 1.5 hours. As such, we opted to perform the following measurements on cells exposed to 1-BD after 2 hours of incubation.

In order to characterize the effect of 1-BD on the expression level of AcrB, we quantified the number of AcrB-PAmCherry molecules in individual TV001 cells after 2 hours of incubation with either 1-BD, sodium salicylate (positive control) or no substance (negative control). The final concentrations of 1-BD and sodium salicylate present in the growth medium corresponded to ¼ of the minimal inhibitory concentration of the same compounds, which was previously determined by our study partners. The detailed protocol of this experiment is provided in appendix 7.

The average number of AcrB-PAmCherry copies observed in individual bacteria is reported in Figure 64 along with the respective standard error. Asterisks represent statistical significance as determined with Student's t-test (* $p<0.05$; ** $p<0.01$; *** $p<0.001$).

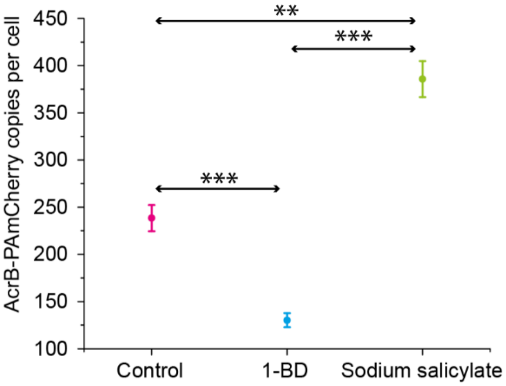

Figure 64. Average AcrB-PAmCherry copy number observed in bacterial cells grown for 2 hours in standard LB broth (Control), LB broth with added 1-BD and LB broth with added sodium salicylate.

There is a statistically significant decrease in the amount of observable AcrB-PAmCherry in bacterial cells after exposure to 1-BD with respect to unexposed controls, which suggests an inhibitory effect of 1-BD on the expression of AcrB. The number of AcrB-PAmCherry copies in bacteria treated with 1-BD (110.1±6.1) is about half of the copies measured in control cells (226.5±11.2). Conversely, in the presence of sodium salicylate, AcrB-PAmCherry expression is roughly doubled (389.2±18.3).

The procedure used for sample preparation, qPALM imaging and data analysis is the same described in sections 5.2.1 to 5.2.4. The only notable difference was that all bacterial samples were grown in LB medium instead of M9 minimal medium. This was due to the fact that all previous characterizations of the activity of 1-BD had been performed by our partners on LB medium, so we had to implement the same growth conditions to produce compatible results. However, this introduced a noticeable level of background fluorescence in all the PALM movies acquired as part of these experiments. This means that all the reported numbers of localizations are likely overestimated by the detection of false events, but the differences highlighted in our results were consistent between three independent experiments and are statistically significant.

5.4 Conclusions and future perspectives

In the second part of this thesis, I have reported on our development of a unique biological platform for the study of bacterial efflux pumps, on our development of an imaging technique that allows us to obtain quantitative data from that platform, and on some early information we have obtained by employing this technique. We have: (i) engineered a novel *E. coli* strain (TV001) that expresses a functional, fluorescently labelled version of the AcrB protein at physiological levels; (ii) developed a method to extract quantitative information on the number of copies of AcrB in individual bacteria via PALM microscopy; and (iii) employed this system to investigate the expression regulation of AcrB in biofilm-associated bacteria as well as to unravel the mechanism of action of a novel AcrB inhibitor.

Directly observing and counting the instances of a protein inside individual cells is a laborious process, requiring ad hoc engineering of a model organism and all the infrastructure required for single-molecule localization microscopy; however, it allows investigators to obtain information with a spatial and temporal resolution that is otherwise completely inaccessible. As such, the development of a strain such as TV001 is a result in and of itself, as it allows to bypass the first roadblock to this kind of experiments and can be employed in a variety of studies concerning the protein of interest. Applying our quantitative PALM technique to our engineered strain allowed us to directly answer a question on the activity of 1-BD that was otherwise outside of the reach of other techniques. Providing direct evidence that 1-BD acts as an inhibitor of the expression of AcrB suggests that 1-BD may have a very desirable mode of action, as EP inhibitors that instead target pump activity are more prone to select for resistant phenotypes[184]. Further investigation, using our technique, of other EP inhibitors characterized by our study partners is being planned for the near future.

Our early investigation into AcrB expression in biofilms has also produced some very interesting results, which need to be studied more in deep. The extremely low levels of AcrB expression by bacterial cells located in the bottom layer of the biofilm is totally unexpected, but our inability to deal with the high scattering levels of the higher biofilm layers (above 15 μm) prevented us from investigating the situation elsewhere in the samples during our early experiments. One of the future steps in this research will surely be to try and overcome this limitation in order to scan deeper within these samples, either by optimizing the preparation of samples in order to reduce scattering (e.g.: with clearing techniques), or by imaging the biofilms in an inverted configuration (e.g.: by mounting a coverslip on top of a mature biofilm).

The issue of persisters can also be tackled by implementing a method to discriminate between actively growing and metabolically inactive cells in a population. Pu *et al.*[142] employed a coarse filter via penicillin-mediated killing of actively replicating bacteria in order to select for persisters in their experiments, while Shah *et al.*[136] employed a bacterial strain expressing an unstable version of GFP from a promoter whose activity depends on the growth rate. Adopting one of these or a similar method in conjunction with our strain and technique would allow us to shed light on the issue of efflux pump production by persister bacteria.

6 Conclusions and future perspectives

As I have expressed in the introduction to this dissertation, super-resolution and single-molecule microscopy techniques have become increasingly relevant in biology over the last couple of decades. Since their first introduction in the mid-2000s, SMLM techniques have been rapidly developing, increasing both in their technical capabilities and in their range of applications. However, there is still much room for improvement.

In this thesis, we have tackled both the topic of improving SMLM techniques and that of finding novel and useful applications for them.

In the first part of our work, we showed that the most commonly used illumination technique for PALM/STORM microscopy (namely, HILO illumination) can greatly benefit from an optimized configuration. At first, we described a method that can be used to thoroughly characterize the propagation of a laser beam within a microscopy sample. We showed that HILO illumination, in its standard form, provides for a relatively low background reduction when applied to the imaging of thin biological specimens such as single-cell layers. We demonstrated that reducing the inclined beam thickness to around 2.7 μm with a very simple method leads to a significant reduction in the background fluorescence when imaging mammalian cell samples, which in turn allows for a much better sampling of fluorophores in SMLM experiments.

In the second part of this dissertation, we presented our efforts towards unlocking the intrinsic capabilities of PALM microscopy to provide quantitative single-molecule information, and our application of this to a relevant biological problem. By specially engineering a biological system for use in quantitative microscopy, we could reliably use PALM to count individual proteins in bacterial cells. Even though this is not the first reported attempt at quantitative PALM, this intrinsic possibility of single-molecule imaging is still largely unexplored and unexploited. Moreover, in our genomic engineering efforts for the creation of a qPALM-ready bacterial strain, we present a number of good practices that prospective investigators should adopt when designing a biological system for the same purpose – for instance, the seamless genomic integration of the label sequence, the process of codon-optimization of any foreign DNA, and the use of irreversibly photoactivatable fluorescent proteins. By applying our quantitative PALM technique to the study of the AcrB protein, we could directly count efflux pumps in individual bacteria for the first time. We exploited this capability to unravel the mechanism of action of a novel efflux pump inhibitor (1-BD), and we also obtained some very interesting preliminary results on the differences in efflux pump expression between planktonic and biofilm-associated bacteria. Moreover, the creation of TV001 as part of this study opens up a great number of possibilities regarding the investigation of the expression regulation and the distribution of AcrB in bacteria. As we are already over the major technical hurdle of producing a novel bacterial strain, it is now just a matter of designing new imaging experiments – both for us, and for other groups that might be interested in this subject.

As stated in the individual conclusions of Part I and Part II, our future perspectives revolve around further improving our optimized HILO technique (for instance, by solving the problem of the reduction in field of view), as well as deepening our initial investigation into the distribution of AcrB in biofilms. Moreover, continued collaboration with our study partners for the characterization of a larger number of efflux pump inhibitors is on the table, and experiments for the investigation of the role of AcrB in persisters are being planned.

7 Appendix: DNA sequences, custom-made scripts and additional protocols

7.1 Imaging buffer composition for STORM imaging experiments involving Alexa Fluor 488 or Alexa Fluor 647 (2.1.1)

This buffer is prepared by freshly mixing the following components (all quantities are relative to the amount of buffer required for a single sample):

- 335 µl of phosphate-buffered saline (PBS), pH-adjusted to 8-8.5 with NaOH
- 100 µl of calcium lactate (Sigma-Aldrich)
- 50 µl of 1 M MEA (Sigma-Aldrich) dissolved in water
- 15 µl of OxyFluor (Sigma-Aldrich)

Once prepared, this buffer maintains its activity for at least 8 hours.

7.2 Protocol for the growth and preparation of mammalian cells for STORM imaging (2.1.1)

In this section I will describe the growth and preparation of mammalian cells samples to be used in STORM microscopy experiments. I will give the example of an actin cytoskeleton staining with Alexa Fluor 488-conjugated phallotoxins, but the general protocol can be equally integrated with any other staining approach for labelling intracellular targets, including classical immunostaining with primary and secondary antibodies.

- Under a sterile laminar flow hood, a frozen stock aliquot (approximately 1 ml) of the cell line of choice is thawed by immersing it into 4 ml of the appropriate culture medium, previously warmed at 37°C.

- After the frozen stock has completely dissolved, the cell suspension is centrifuged for 3 minutes at 300 x g in order to separate the cells from the DMSO-containing storage medium.
- The supernatant is removed and the cells are resuspended in 5 ml of fresh culture medium. The cell suspension is plated in a 60 mm cell culture dish and placed in a CO_2 incubator for growth.
- The cells are cultured according to the specifications for their respective line, and should be passaged at least twice before being used for imaging.
- The cells are plated at around 10% confluency on top of 18 mm glass coverslips placed in a 12-well culture plate (optional: the coverslips can be previously coated in poly-L-lysine to improve the adhesion of certain cell types).
- After 16-24 hours, the cells are rinsed three times in PBS with added $MgCl_2$ (0.5 mM) and $CaCl_2$ (0.8 mM), and fixed by incubating for 10 minutes in a 4% paraformaldehyde (PFA) solution in PBS.
- The cells are rinsed three times in PBS with added $MgCl_2$ and $CaCl_2$, and permeabilized by incubating for 7 minutes in a 0.075% Triton X-100 solution in PBS.
- The cells are rinsed three more times in PBS with added $MgCl_2$ and $CaCl_2$, and then blocked by incubating for at least 30 minutes in a 4% bovine serum albumin (BSA) solution in PBS with added $MgCl_2$ and $CaCl_2$.
- At this point the BSA solution is removed and the labelling reagent is added at the appropriate concentration. STORM experiments require especially dense labelling: in the case of actin staining, 30 µl of a stock solution of Alexa Fluor 488 phalloidin (Thermo Fisher Scientific) in methanol (approximate concentration: 6.6 µM) are diluted into 400 µl of PBS, yielding a final concentration of

approximately 0.5 µM of fluorescent label. The samples are then incubated in the dark at 4°C overnight.

NOTE: for primary and secondary antibody labelling, a first incubation period with the primary antibody is followed by three washes in PBS before the secondary antibody is applied.

- After the staining process is complete, the samples are washed a single time in PBS before being mounted in an imaging chamber and immersed in the imaging buffer as described in section 2.1.1.

7.3 Protocol for the preparation of a model sample of homogeneously distributed fluorescent microspheres in agarose (3.3)

- Agarose is dissolved in distilled water at a 2% concentration and brought to a boil using a microwave.
- 50 µl of the melted agarose solution are placed in a pre-warmed microcentrifuge tube which is immersed in a ~95°C water bath.
- A vial of TetraSpeck™ microspheres (Invitrogen) is sonicated for about 1 minute in a 45 kHz ultrasonic cleaner and thoroughly vortexed before taking 1 µl of the microsphere suspension and adding it to the 50 µl of melted agarose.
- The agarose-microsphere mixture is dropped in the center of a clean, pre-heated microscope glass slide, sitting on top of a heat block at ~95°C.
- The melted agarose drop is covered with a clean 20x20 mm coverslip and lightly pressed in order to have it spread evenly under the whole coverslip surface.
- The sample is cooled for a few minutes in order to have it solidify before imaging.

7.4 Procedure for correcting the number of localizations in STORM images to account for bleaching (3.5.3)

After normalizing the number of localization per dSTORM measurement to account for bleaching as described in section 3.5.2, the reconstructed images were adapted as follows:

1) For the measurement with the highest number of localizations in the set, the ratio between the original number of localizations and the normalized number was calculated. $a = N_1/N_{1norm}$
   Where N_1 is the original number and N_{1norm} is the normalized number of localizations.
2) The corresponding reconstructed image was not changed, and kept the original number of localizations. $N_{1img} = aN_{1norm} = N_1$
   Where N_{1img} is the number of spots in the final reconstructed image.
3) The a ratio was used to normalize the number of spots in the other 2 images of the set. $N_{2img} = aN_{2norm} < N_2$
   $N_{3img} = aN_{3norm} < N_3$
4) In order to produce a second and third reconstructed image with respectively N_{2img} and N_{3img} spots, the original images containing N_2 and N_3 localizations were "pruned" by removing a number of spots equal to $N_2 - N_{2img}$ and $N_3 - N_{3img}$. The spots to be removed were chosen at random with a custom MATLAB function.

7.5 Description of the strategy employed for the amplification of the GeneStrand dsDNA template (5.1.2)

A commercial bacterial expression plasmid by Promega (pFC20A), designed for expressing HaloTag fusion proteins, was modified to be used as a platform for replicating the GeneStrand in bacteria. The plasmid was PCR amplified with the following primers:

FW: 5’-GTCATATTCAGAGCAATCCTGTCTAGGCCCAGTAGCTGACATTCATC-3’

REV: 5’-CGAGGATAAACGCCAGCGAGTCTAGGTGTGCCATGTGGATTCCTTAC-3’

We designed these primers in order to remove from the plasmid a region containing the HaloTag coding sequence and a lethal gene (barnase) which was originally used for positive selection of plasmid inserts. The resulting PCR product was a linear dsDNA containing only the origin of replication of the plasmid (*Col*E1-derived) and an ampicillin resistance gene. The two primers were engineered in order to flank the PCR product with two regions of homology (20 and 21 bp long) with the 5’ and 3’ extremities of the GeneStrand described in section 5.1.2. The PCR product was digested with DpnI in order to remove the template plasmid and then purified using a Qiagen PCR cleanup kit.

The abridged and linearized pFC20A was then recombined with the PAmCherry-encoding GeneStrand via AQUA cloning[185] in order to obtain plasmid pFC20A-PAmCherry.

Shortly: about 36 ng of PCR product were mixed with 36 ng of GeneStrand in 10 µl of Milli-Q water and incubated overnight at room temperature. The next morning, the reaction mix was transformed via heat shock in chemically competent bacteria (DH5-Alpha, Invitrogen) which were then plated on ampicillin-containing LB-agar dishes. Colonies were then screened for the presence of pFC20A-PAmCherry via colony PCR with the following primers:

gStrand_FW: 5’-CTCGCTGGCGTTTATCCTC-3’

gStrand_REV: 5’-CAGGATTGCTCTGAATATGACG-3’

Positive colonies were then verified by sequencing.

We could then easily obtain large amounts of pFC20A-PAmCherry by culturing the plasmid-containing bacteria in LB broth with added ampicillin and extracting the plasmid with a standard miniprep. The original GeneStrand could then be extracted by PCR amplifying pFC20A with primers gStrand_FW and gStrand_REV, and a high fidelity DNA polymerase (Phusion by Thermo Fisher Scientific).

7.6 Description of the CRISPR/Cas9-assisted genome editing process of TV001 (5.1.3)

Plasmid pCas9-CR4 (https://www.addgene.org/62655/) containing the *cas9* gene and plasmid pKDsgRNA-ack (https://www.addgene.org/62654/) containing the λ Red recombination genes *exo*, *beta* and *gam* as well as a single-guide RNA (sgRNA) expression cassette, were ordered from Addgene.

Plasmid pKDsgRNA-ack contains a sgRNA cassette designed for targeting the *ack* gene in *E. coli*. We retargeted this plasmid towards the PAM site in the *acrB* gene through site-specific mutagenesis (Quik Change kit, Agilent), obtaining plasmid pKDsgRNA-acrB.

Shortly: pKDsgRNA-ack was PCR amplified with the following mutagenic primers:

FW: 5'-ATCAATGATGATCGACAGTAGTTTTAGAGCTAGAAATAGCAAG-3'

REV: 5'-TACTGTCGATCATCATTGATGTGCTCAGTATCTCTATCACTGA-3'

These two primers anneal to the same region of the plasmid, replacing the 20-bp long protospacer targeting *ack* with a new protospacer targeting *acrB*.

The PCR product was then digested with DpnI to remove the original pKDsgRNA-ack plasmid from the mix and directly transformed via heat shock in XL 10-Gold chemically competent cells (Agilent), which were then selected on LB-agar plates with added spectinomycin. As pKDsgRNA plasmids hold a temperature-sensitive origin of replication, all growth passages involving these plasmids were performed at 30°C. Plasmid pKDsgRNA-acrB was then extracted from a few colonies via standard miniprep and the correct mutation was verified by sequencing.

After the sgRNA cassette had been retargeted, BW25113 bacteria were prepped for CRISPR/Cas9-assisted recombineering by transforming them sequentially with pCas9-CR4 and pKDsgRNA-acrB. It is crucial that these two transformations are performed in this exact sequence and at different times as both the *cas9* gene and the sgRNA cassette are under the control of a TetR-controlled operator. This transcription regulation system is extremely effective at maintaining a null expression level in the absence of the inductor (anhydrotetracycline, or aTC) but rely on a previous intracellular accumulation of the TetR repressor to block gene transcription. Since a single Cas9 molecule coupled with a single sgRNA is sufficient to induce a double-strand break on the DNA of a bacterium leading to cell death, it is crucial to prevent expression of both genes at the same time. The *tetR* gene is encoded on plasmid pCas9, therefore the transformation of this plasmid must happen before the transformation of pKDsgRNA to allow for the accumulation of the TetR protein inside cells.

First, BW25113 bacteria were made chemically competent with the calcium chloride method[186]; they were transformed with pCas9-CR4 via heat shock and then selected on LB-agar plates with added chloramphenicol. Cells harboring pCas9-CR4 were again made chemically competent with the same technique and transformed with pKDsgRNA-acrB. After a recovery step at 30°C, half of the transformation mix was plated on LB-agar with added chloramphenicol and spectinomycin. The other half was plated on dishes with added aTC. As aTC is a transcription inductor of both Cas9 and sgRNA, these plates were used to verify that the CRISPR/Cas9 selection system was working properly. A lot fewer colonies grew in the plates containing aTC compared to the other plates, confirming that Cas9 was successfully killing the bacteria.

BW25113 bacteria harboring both pCas9-CR4 and pKDsgRNA-acrB were then grown in LB broth with the proper antibiotics until mid-log phase, at which point arabinose was added at a final concentration of 1.2% in order to induce the λ Red genes in plasmid pKDsgRNA-acrB. After 15 minutes of induction, the cells were made electrically competent using glycerol/mannitol density step centrifugation as described by Warren[187].

Electrically competent cells were immediately transformed with 1500 ng of (PCR-amplified and purified) linear GeneStrand via electroporation, recovered at 30°C, and then plated on LB-agar containing chloramphenicol, spectinomycin and aTC. Colonies were screened for positive recombination via colony PCR with primers gStrand_FW and gStrand_REV, and then verified by sequencing.

The pCas9-CR4 plasmid (Addgene plasmid # 62655 ; http://n2t.net/addgene:62655 ; RRID:Addgene_62655) and the pKDsgRNA-ack plasmid (Addgene plasmid # 62654 ; http://n2t.net/addgene:62654 ; RRID:Addgene_62654) were gifts from Kristala Prather, Massachusetts Institute of Technology, Department of Chemical Engineering. All of the E. coli BW25113 strains used in this study were gifts from Laura Piddock, University of Birmingham, Institute of Microbiology and Infection.

7.7 Protocol for the growth and preparation of planktonic bacteria and biofilm samples for qPALM imaging (5.2.1)

Samples of planktonic bacteria were prepared in the following way:

- *E. coli* TV001 was grown in M9 with added glucose (0.4%) for around 36 hours at 37°C under vigorous shaking.

- 1 ml of culture was centrifuged (5,000 g for 5 minutes), resuspended in a paraformaldehyde solution (4% PFA in PBS) and incubated for 10 minutes.
- The cells were centrifuged (5,000 g for 5 minutes) and resuspended in PBS twice to remove excess formaldehyde.
- 20 µl aliquots of fixed bacterial suspension were then fluxed in custom-built glass imaging chambers coated with poly-L-lysine and left to adhere to the coverslip for at least 20 minutes prior to imaging. A schematic illustration of these chambers is shown in Figure 65.

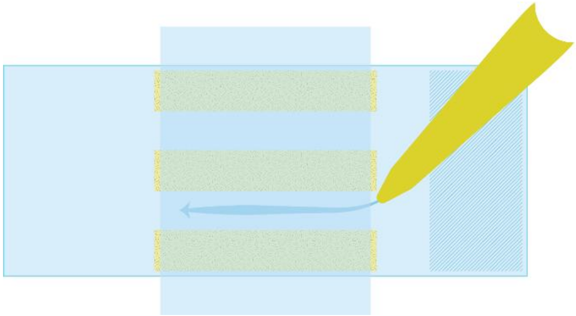

Figure 65. Imaging chamber composed of a rectangular glass coverslip attached on a microscope slide through thin strips of double sticky tape, which also serve as delimiters between separate channels. Each channel has a volume of approximately 20 µl. Samples and solutions are fluxed into the channels by pipetting through one of the open ends.

Biofilm samples were prepared in the following way:

- A starting *E. coli* TV001 culture was grown overnight in LB medium.
- The next day, 1 ml of the starting culture was centrifuged (10,000 g for 2 minutes) and resuspended in an equal volume of PBS in sterile conditions.
- While maintaining sterility, 25 µl of the bacterial suspension were inoculated in 1 ml of fresh M9 medium with added glucose (0.4%) previously placed on an open-ceiling imaging chamber like the one

described in 2.1.1, assembled with a bottom coverslip coated with poly-L-lysine.

- The imaging chamber containing the inoculated medium was placed inside of a 100 mm sterile culture dish, and incubated at 37°C for around 36 hours without any shaking.
- After the incubation period, a biofilm layer is clearly visible at the bottom of the imaging chamber. The culture medium is very gently removed, paying attention not to detach the biofilm from the coverslip.
- Still very carefully, the biofilm is covered with 500 µl of a 4% PFA solution in PBS and incubated for 10 minutes.
- The fixing solution is delicately removed and the biofilm is covered with 500 µl of PBS.
- The chamber is mounted on the microscope for imaging. Figure 66 shows a biofilm mounted for imaging. The characteristic wrinkles of *E. coli* biofilms are visible.

Figure 66. Biofilm sample mounted on the microscope.

7.8 qPALM imaging procedure for E. coli TV001 (5.2.2)

The following is a step-by-step description of the imaging process:

- The EM gain on the EMCCD camera is set to 0, and the sample is explored with bright field illumination until a suitable field of view is found. A reference bright field image is taken.
- The EM gain is set to 400 and the field of view is illuminated with the 532 nm laser at high intensity (~740 W/cm^2) in order to lower the cellular autofluorescence for about 10 seconds or until there is no more visible fluorescence.
- Without turning off the 532 nm laser, the acquisition of a 1000-frames-long movie is started with an integration time of 100 ms per frame. As soon as the acquisition begins, the field of view is illuminated by low-intensity 405 nm light (~0.7 W/cm^2) in order to gradually photoactivate the underlying PAmCherry molecules. The 405 nm laser power is finely tuned to activate a small enough percentage of fluorescent molecules per frame that the overlap of neighboring PSFs is not an issue. Typically, all of the PAmCherry instances within the field of view are activated, imaged and bleached before the 1000-frame movie acquisition ends.

N.B.: the illumination configuration for both the 405 nm and the 532 nm lasers was HILO, with an angle θ_r of 77° within the sample and a field of view with a diameter R of 40 µm.

7.9 Protocol for the growth and preparation of bacterial samples to investigate the effects of 1-BD (5.3)

- *E. coli* strain TV001 was grown in LB medium at 37°C with shaking (210 rpm) overnight.

- The next day, the cells were diluted 1:100 in fresh LB medium and kept at 37 °C with shaking in vented tubes for 2 hours to reach the logarithmic growth phase.
- Afterwards, the bacteria were treated with (i) 1-BD at 0.4 mg/ml final concentration or (ii) sodium salicylate at 0.8 mg/ml final concentration. A third sample was left untreated as a control. Bacteria were treated for 2 hours while shaking at 37°C.
- The cells were washed twice by centrifuging at 5000 g for 5 minutes and resuspending in PBS.
- After washing, the cells were fixed by resuspending the pellet in 500 µl of a 4% PFA solution in PBS and incubating it at room temperature for 10 minutes.
- After fixation, the samples were washed twice by centrifuging and resuspending the pellet in PBS. The samples were stored at 4°C for less than 24 hours prior to imaging.
- 20 µl of bacterial suspension were fluxed in imaging chambers like the one described in Figure 65 and the cells were left to adhere to the coverslip for at least 20 minutes prior to imaging.

7.10 Bacterial strains, plasmids and cell types used in this study

	Relevant characteristics	Parent	Source or reference
E. coli strains			
BW25113	Wild type	W1485	[163]
JW0451	ΔacrB::kan	BW25113	[182]
JW5503	ΔtolC::kan	BW25113	[182]
TV001	ΩacrB::PAmCherry	BW25113	This study
Plasmids			
pFC20A	vector		Promega
pFC20A-PAmCherry	PAmCherry sequence flanked by homology regions for recombination	pFC20A	This study
pCas9-CR4	Cas9		[164]
pKDsgRNA-ack	λ Red genes, protospacer targeting *ack*		[164]
pKDsgRNA-acrb	λ Red genes, protospacer targeting *acrb*	pKDsgRNA-ack	This study
Cell types			
HEK 293	Wild type		Sigma-Aldrich

7.11 Antibiotic concentrations used

Antibiotic	Purpose	Concentration
Ampicillin	pFC20A-PAmCherry selection	100 µg/ml
Spectinomycin	pKDsgRNA-ack/acrb selection	50 µg/ml
Chloramphenicol	pCas9-CR4 selection	25 µg/ml
Chloramphenicol	MIC screening	0.0625-64 µg/ml

8 Bibliography

[1] Heimstädt, O., “Das Fluoreszenzmikroskop,” Z. Wiss. Mikrosk. **28**, 330–337 (1911).

[2] Haitinger, M. and Hamperl, H., “Die Anwendung des Fluoreszenmicroskops zur Untersuchung tierischer Gewebe,” Z. Microskop. Anatom. Forsch. **33**, 193–221 (1933).

[3] Coons, A. H., Creech, H. J. and Jones, R. N., “Immunological Properties of an Antibody Containing a Fluorescent Group,” Proc. Soc. Exp. Biol. Med. **47**(2), 200–202 (1941).

[4] Coons A H, Creech H J, Jones R N and Berliner G., “The demonstration of pneumococcal antigen in tissues by the use of fluorescent antibody,” J. Immunol. **45**, 159 (1942).

[5] Abbe, E., “Beiträge zur Theorie des Mikroskops und der mikroskopischen Wahrnehmung,” Arch. für Mikroskopische Anat. **9**(1), 413–418 (1873).

[6] “Search BioNumbers - The Database of Useful Biological Numbers.”, <https://bionumbers.hms.harvard.edu/search.aspx> (9 October 2019).

[7] Xu, K., Babcock, H. P. and Zhuang, X., “Dual-objective STORM reveals three-dimensional filament organization in the actin cytoskeleton,” Nat. Methods **9**(2), 185–188 (2012).

[8] Selvin, P. R., Lougheed, T., Tonks Hoffman, M., Park, H., Balci, H., Blehm, B. H. and Toprak, E., “Fluorescence Imaging with One-Nanometer Accuracy (FIONA),” Cold Spring Harb. Protoc. **2007**(10), pdb.top27 (2007).

[9] “Micron Oxford Advanced Bioimaging: Localisation Microscopy.”, <https://www.micron.ox.ac.uk/research/localization-microscopy>

(9 October 2019).

[10] Airy, G. B., “On the diffraction of an object-glass with circular aperture,” Trans. Cambridge Phil. Soc. **5**, 283–291 (1835).

[11] “A Simple Model for Sharpness in Digital Cameras – I | Strolls with my Dog.”, <https://www.strollswithmydog.com/resolution-model-digital-cameras-i/> (9 October 2019).

[12] “Numerical Aperture | MicroscopyU.”, <https://www.microscopyu.com/microscopy-basics/numerical-aperture> (9 October 2019).

[13] “Milestones in light microscopy.”, Nat. Cell Biol. **11**, 1165 (2009).

[14] De Broglie, L., “Recherches sur la théorie des Quanta,” Ann. Phys. (Paris). **10**(3), 22–128 (1925).

[15] Ruska, E. and Knoll, M., “Die magnetische Sammelspule für schnelle Elektronenstrahlen,” Z. techn. Phys. **12**, 389–400 (1931).

[16] Cheezum, M. K., Walker, W. F. and Guilford, W. H., “Quantitative comparison of algorithms for tracking single fluorescent particles,” Biophys. J. **81**(4), 2378–2388 (2001).

[17] “ZEISS Microscopy Online Campus | Practical Aspects of Photoactivated Localization Microscopy (PALM).”, <http://zeiss-campus.magnet.fsu.edu/articles/superresolution/palm/practicalaspects.html> (9 October 2019).

[18] Thompson, R. E., Larson, D. R. and Webb, W. W., “Precise nanometer localization analysis for individual fluorescent probes,” Biophys. J. **82**(5), 2775–2783 (2002).

[19] Yildiz, A. and Selvin, P. R., “Fluorescence imaging with one nanometer accuracy: Application to molecular motors,” Acc. Chem.

Res. **38**(7), 574–582 (2005).

[20] Yildiz, A., Forkey, J. N., McKinney, S. A., Ha, T., Goldman, Y. E. and Selvin, P. R., "Myosin V walks hand-over-hand: Single fluorophore imaging with 1.5-nm localization," Science (80-.). **300**(5628), 2061–2065 (2003).

[21] Yildiz, A., Park, H., Safer, D., Yang, Z., Chen, L. Q., Selvin, P. R. and Sweeney, H. L., "Myosin VI steps via a hand-over-hand mechanism with its lever arm undergoing fluctuations when attached to actin," J. Biol. Chem. **279**(36), 37223–37226 (2004).

[22] Yildiz, A., Tomishige, M., Vale, R. D. and Selvin, P. R., "Kinesin Walks Hand-Over-Hand," Science (80-.). **303**(5658), 676–678 (2004).

[23] Betzig, E., Patterson, G. H., Sougrat, R., Lindwasser, O. W., Olenych, S., Bonifacino, J. S., Davidson, M. W., Lippincott-Schwartz, J. and Hess, H. F., "Imaging intracellular fluorescent proteins at nanometer resolution," Science (80-.). **313**(5793), 1642–1645 (2006).

[24] Rust, M. J., Bates, M. and Zhuang, X., "Sub-diffraction-limit imaging by stochastic optical reconstruction microscopy (STORM)," Nat. Methods **3**(10), 793–795 (2006).

[25] Jimenez, A., Friedl, K. and Leterrier, C., "About samples, giving examples: Optimized Single Molecule Localization Microscopy," Methods (2019).

[26] Subach, F. V., Patterson, G. H., Manley, S., Gillette, J. M., Lippincott-Schwartz, J. and Verkhusha, V. V., "Photoactivatable mCherry for high-resolution two-color fluorescence microscopy," Nat. Methods **6**(2), 153 (2009).

[27] Shcherbakova, D. M., Sengupta, P., Lippincott-Schwartz, J. and

Verkhusha, V. V., “Photocontrollable Fluorescent Proteins for Superresolution Imaging,” Annu. Rev. Biophys **43**, 303–329 (2014).

[28] Dempsey, G. T., Bates, M., Kowtoniuk, W. E., Liu, D. R., Tsien, R. Y. and Zhuang, X., “Photoswitching mechanism of cyanine dyes,” J. Am. Chem. Soc. **131**(51), 18192–18193 (2009).

[29] van de Linde, S., Sauer, M. and Heilemann, M., “Subdiffraction-resolution fluorescence imaging of proteins in the mitochondrial inner membrane with photoswitchable fluorophores,” J. Struct. Biol. **164**(3), 250–254 (2008).

[30] Subach, F. V., Malashkevich, V. N., Zencheck, W. D., Xiao, H., Filonov, G. S., Almo, S. C. and Verkhusha, V. V., “Photoactivation mechanism of PAmCherry based on crystal structures of the protein in the dark and fluorescent states,” Proc. Natl. Acad. Sci. U. S. A. **106**(50), 21097–21102 (2009).

[31] Marsh, R. J., Pfisterer, K., Bennett, P., Hirvonen, L. M., Gautel, M., Jones, G. E. and Cox, S., “Artifact-free high-density localization microscopy analysis,” Nat. Methods **15**(9), 689–692 (2018).

[32] Chozinski, T. J., Gagnon, L. A. and Vaughan, J. C., “Twinkle, twinkle little star: Photoswitchable fluorophores for super-resolution imaging,” FEBS Lett. **588**(19), 3603–3612 (2014).

[33] Van De Linde, S., Krstić, I., Prisner, T., Doose, S., Heilemann, M. and Sauer, M., “Photoinduced formation of reversible dye radicals and their impact on super-resolution imaging,” Photochem. Photobiol. Sci. **10**(4), 499–506 (2011).

[34] Van De Linde, S., Löschberger, A., Klein, T., Heidbreder, M., Wolter, S., Heilemann, M. and Sauer, M., “Direct stochastic optical reconstruction microscopy with standard fluorescent probes,” Nat. Protoc. **6**(7), 991 (2011).

[35] Nahidiazar, L., Agronskaia, A. V., Broertjes, J., Van Broek, B. Den and Jalink, K., “Optimizing imaging conditions for demanding multi-color super resolution localization microscopy,” PLoS One **11**(7), e0158884 (2016).

[36] Gardini, L., Calamai, M., Hatakeyama, H., Kanzaki, M., Capitanio, M. and Pavone, F. S., “Three-Dimensional Tracking of Quantum Dot-Conjugated Molecules in Living Cells,” [Nanoscale Imaging], Humana Press, New York, NY, 425–448 (2018).

[37] Dempsey, G. T., Vaughan, J. C., Chen, K. H., Bates, M. and Zhuang, X., “Evaluation of fluorophores for optimal performance in localization-based super-resolution imaging,” Nat. Methods **8**(12), 1027 (2011).

[38] Shroff, H., Galbraith, C. G., Galbraith, J. A. and Betzig, E., “Live-cell photoactivated localization microscopy of nanoscale adhesion dynamics,” Nat. Methods **5**(5), 417 (2008).

[39] Shannon, C. E., “Communication in the Presence of Noise,” Proc. IRE **37**(1), 10–21 (1949).

[40] “Molecular Density in Super-Resolution Microscopy | MicroscopyU.”, <https://www.microscopyu.com/tutorials/molecular-density-in-superresolution-microscopy> (8 October 2019).

[41] Dertinger, T., Colyera, R., Iyer, G., Weiss, S. and Enderlein, J., “Fast, background-free, 3D super-resolution optical fluctuation imaging (SOFI),” Proc. Natl. Acad. Sci. U. S. A. **106**(52), 22287–22292 (2009).

[42] Gustafsson, N., Culley, S., Ashdown, G., Owen, D. M., Pereira, P. M. and Henriques, R., “Fast live-cell conventional fluorophore nanoscopy with ImageJ through super-resolution radial fluctuations,” Nat. Commun. **7**(1), 1–9 (2016).

[43] Ovesný, M., Křížek, P., Borkovec, J., Švindrych, Z. and Hagen, G. M., "ThunderSTORM: A comprehensive ImageJ plug-in for PALM and STORM data analysis and super-resolution imaging," Bioinformatics **30**(16), 2389–2390 (2014).

[44] Schindelin, J., Arganda-Carreras, I., Frise, E., Kaynig, V., Longair, M., Pietzsch, T., Preibisch, S., Rueden, C., Saalfeld, S., Schmid, B., Tinevez, J. Y., White, D. J., Hartenstein, V., Eliceiri, K., Tomancak, P. and Cardona, A., "Fiji: An open-source platform for biological-image analysis," Nat. Methods **9**(7), 676–682 (2012).

[45] Schneider, C. A., Rasband, W. S. and Eliceiri, K. W., "NIH Image to ImageJ: 25 years of image analysis," Nat. Methods, 671–675 (2012).

[46] Quan, T., Zeng, S. and Huang, Z.-L., "Localization capability and limitation of electron-multiplying charge-coupled, scientific complementary metal-oxide semiconductor, and charge-coupled devices for superresolution imaging," J. Biomed. Opt. **15**(6), 066005 (2010).

[47] Kudalkar, E. M., Davis, T. N. and Asbury, C. L., "Single-Molecule Total Internal Reflection Fluorescence Microscopy," Cold Spring Harb Protoc. **2016**(5), pdb-top077800 (2016).

[48] Tokunaga, M., Imamoto, N. and Sakata-Sogawa, K., "Highly inclined thin illumination enables clear single-molecule imaging in cells," Nat. Methods **5**(2), 159–161 (2008).

[49] Saleh, B. E. A. and Teich, M. C., "Fundamentals of Photonics, 2nd Edition," Wiley (2007).

[50] Serdyuk, V. M. and Titovitsky, J. A., "A Simple Analytic Approximation for the Refracted Field at Gaussian Beam Incidence upon a Boundary of Absorbing Medium," J. Electromagn. Anal. Appl. (2010).

[51] Visser, T. D. and Oud, J. L., "Volume measurements in three-dimensional microscopy," Scanning **16**(4), 198–200 (1994).

[52] Diaspro, A., Federici, F. and Robello, M., "Influence of refractive-index mismatch in high-resolution three-dimensional confocal microscopy," Appl. Opt. **41**(4), 685–690 (2002).

[53] Hell, S., Reiner, G., Cremer, C. and Stelzer, E. H. K., "Aberrations in confocal fluorescence microscopy induced by mismatches in refractive index," J. Microsc. **169**(3), 391–405 (1993).

[54] Gardini, L., Capitanio, M. and Pavone, F. S., "3D tracking of single nanoparticles and quantum dots in living cells by out-of-focus imaging with diffraction pattern recognition," Sci. Rep. **5**, 16088 (2015).

[55] Tang, J. and Han, K. Y., "Extended field-of-view single-molecule imaging by highly inclined swept illumination," Optica **5**(9), 1063 (2018).

[56] Marquez, B., "Bacterial efflux systems and efflux pumps inhibitors," Biochimie **87**(12), 1137–1147 (2005).

[57] Webber, M. A. and Piddock, L. J. V., "The importance of efflux pumps in bacterial antibiotic resistance," J. Antimicrob. Chemother. **51**(1), 9–11 (2003).

[58] Piddock, L. J. V., "Multidrug-resistance efflux pumps - Not just for resistance," Nat. Rev. Microbiol. **4**(8), 629–636 (2006).

[59] Krishnamoorthy, G., Leus, I. V., Weeks, J. W., Wolloscheck, D., Rybenkov, V. V. and Zgurskaya, H. I., "Synergy between active efflux and outer membrane diffusion defines rules of antibiotic permeation into gram-negative bacteria," MBio **8**(5), e01172-17 (2017).

[60] Duraes, F., Pinto, M. and Sousa, E., "Medicinal Chemistry Updates

on Bacterial Efflux Pump Modulators," Curr. Med. Chem. **25**(42), 6030–6069 (2018).

[61] Du, D., Wang-Kan, X., Neuberger, A., van Veen, H. W., Pos, K. M., Piddock, L. J. V. and Luisi, B. F., "Multidrug efflux pumps: structure, function and regulation," Nat. Rev. Microbiol. **16**(9), 523–539 (2018).

[62] Venter, H., Mowla, R., Ohene-Agyei, T. and Ma, S., "RND-type drug efflux pumps from Gram-negative bacteria: Molecular mechanism and inhibition," Front. Microbiol. **6**, 377 (2015).

[63] Blair, J. M. A., Smith, H. E., Ricci, V., Lawler, A. J., Thompson, L. J. and Piddock, L. J. V., "Expression of homologous RND efflux pump genes is dependent upon AcrB expression: Implications for efflux and virulence inhibitor design," J. Antimicrob. Chemother. **70**(2), 424–431 (2015).

[64] Piddock, L. J. V., "Clinically relevant chromosomally encoded multidrug resistance efflux pumps in bacteria," Clin. Microbiol. Rev. **19**(2), 382–402 (2006).

[65] Li, X. Z., Plésiat, P. and Nikaido, H., "The challenge of efflux-mediated antibiotic resistance in Gram-negative bacteria," Clin. Microbiol. Rev. **28**(2), 337–418 (2015).

[66] Nikaido, H. and Pagès, J. M., "Broad-specificity efflux pumps and their role in multidrug resistance of Gram-negative bacteria," FEMS Microbiol. Rev. **36**(2), 340–363 (2012).

[67] Tikhonova, E. B. and Zgurskaya, H. I., "AcrA, AcrB, and TolC of Escherichia coli form a stable intermembrane multidrug efflux complex," J. Biol. Chem. **279**(31), 32116–32124 (2004).

[68] Du, D., Wang, Z., James, N. R., Voss, J. E., Klimont, E., Ohene-Agyei, T., Venter, H., Chiu, W. and Luisi, B. F., "Structure of the AcrAB-

TolC multidrug efflux pump," Nature **509**(7501), 512–515 (2014).

[69] Sulavik, M. C., Houseweart, C., Cramer, C., Jiwani, N., Murgolo, N., Greene, J., Didomenico, B., Shaw, K. J., Miller, G. H., Hare, R. and Shimer, G., "Antibiotic susceptibility profiles of Escherichia coli strains lacking multidrug efflux pump genes," Antimicrob. Agents Chemother. **45**(4), 1126–1136 (2001).

[70] Weston, N., Sharma, P., Ricci, V. and Piddock, L. J. V., "Regulation of the AcrAB-TolC efflux pump in Enterobacteriaceae," Res. Microbiol. **169**(7–8), 425–431 (2018).

[71] Hagman, K. E., Lucas, C. E., Balthazar, J. T., Snyder, L., Nilles, M., Judd, R. C. and Shafer, W. M., "The MtrD protein of Neisseria gonorrhaeae is a member of the resistance/nodulation/division protein family constituting part of an efflux system," Microbiology **143**(7), 2117–2125 (1997).

[72] Li, X. Z., Livermore, D. M. and Nikaido, H., "Role of efflux pump(s) in intrinsic resistance of Pseudomonas aeruginosa: Resistance to tetracycline, chloramphenicol, and norfloxacin," Antimicrob. Agents Chemother. **38**(8), 1732–1741 (1994).

[73] Li, X. Z., Ma, D., Livermore, D. M. and Nikaido, H., "Role of efflux pump(s) in intrinsic resistance of Pseudomonas aeruginosa: Active efflux as a contributing factor to β-lactam resistance," Antimicrob. Agents Chemother. **38**(8), 1742–1752 (1994).

[74] Lin, J., Overbye Michel, L. and Zhang, Q., "CmeABC functions as a multidrug efflux system in Campylobacter jejuni," Antimicrob. Agents Chemother. **46**(7), 2124–2131 (2002).

[75] Magnet, S., Courvalin, P. and Lambert, T., "Resistance-nodulation-cell division-type efflux pump involved in aminoglycoside resistance in Acinetobacter baumannii strain BM4454," Antimicrob. Agents

Chemother. **45**(12), 3375–3380 (2001).

[76] Masuda, N., Sakagawa, E., Ohya, S., Gotoh, N., Tsujimoto, H. and Nishino, T., “Substrate specificities of MexAB-OprM, MexCD-OprJ, and MexXY-OprM efflux pumps in Pseudomonas aeruginosa,” Antimicrob. Agents Chemother. **44**(12), 3322–3327 (2000).

[77] Pumbwe, L. and Piddock, L. J. V., “Identification and molecular characterisation of CmeB, a Campylobacter jejuni multidrug efflux pump,” FEMS Microbiol. Lett. **206**(2), 185–189 (2002).

[78] Koronakis, V., Sharff, A., Koronakis, E., Luisi, B. and Hughes, C., “Crystal structure of the bacterial membrane protein TolC central to multidrug efflux and protein export,” Nature **405**(6789), 914–919 (2000).

[79] Mikolosko, J., Bobyk, K., Zgurskaya, H. I. and Ghosh, P., “Conformational flexibility in the multidrug efflux system protein AcrA,” Structure **14**(3), 577–587 (2006).

[80] Eicher, T., Cha, H. J., Seeger, M. A., Brandstätter, L., El-Delik, J., Bohnert, J. A., Kern, W. V., Verrey, F., Grütter, M. G., Diederichs, K. and Pos, K. M., “Transport of drugs by the multidrug transporter AcrB involves an access and a deep binding pocket that are separated by a switch-loop,” Proc. Natl. Acad. Sci. U. S. A. **109**(15), 5687–5692 (2012).

[81] Murakami, S., Nakashima, R., Yamashita, E. and Yamaguchi, A., “Crystal structure of bacterial multidrug efflux transporter AcrB,” Nature **419**(6907), 587–593 (2002).

[82] Murakami, S., Nakashima, R., Yamashita, E., Matsumoto, T. and Yamaguchi, A., “Crystal structures of a multidrug transporter reveal a functionally rotating mechanism,” Nature **443**(7108), 173–179 (2006).

[83] Seeger, M. A., Schiefner, A., Eicher, T., Verrey, F., Diederichs, K. and Pos, K. M., "Structural asymmetry of AcrB trimer suggests a peristaltic pump mechanism," Science (80-.). **313**(5791), 1295–1298 (2006).

[84] Sennhauser, G., Amstutz, P., Briand, C., Storchenegger, O. and Grütter, M. G., "Drug export pathway of multidrug exporter AcrB revealed by DARPin inhibitors," PLoS Biol. **5**(1), e7 (2007).

[85] Sjuts, H., Vargiu, A. V., Kwasny, S. M., Nguyen, S. T., Kim, H. S., Ding, X., Ornik, A. R., Ruggerone, P., Bowlin, T. L., Nikaido, H., Pos, K. M. and Opperman, T. J., "Molecular basis for inhibition of AcrB multidrug efflux pump by novel and powerful pyranopyridine derivatives," Proc. Natl. Acad. Sci. U. S. A. **113**(13), 3509–3514 (2016).

[86] Daury, L., Orange, F., Taveau, J. C., Verchère, A., Monlezun, L., Gounou, C., Marreddy, R. K. R., Picard, M., Broutin, I., Pos, K. M. and Lambert, O., "Tripartite assembly of RND multidrug efflux pumps," Nat. Commun. **7**(1), 1–8 (2016).

[87] Jeong, H., Kim, J. S., Song, S., Shigematsu, H., Yokoyama, T., Hyun, J. and Ha, N. C., "Pseudoatomic Structure of the Tripartite Multidrug Efflux Pump AcrAB-TolC Reveals the Intermeshing Cogwheel-like Interaction between AcrA and TolC," Structure **24**(2), 272–276 (2016).

[88] Kim, J. S., Jeong, H., Song, S., Kim, H. Y., Lee, K., Hyun, J. and Ha, N. C., "Structure of the tripartite multidrug efflux pump AcrAB-TolC suggests an alternative assembly mode," Mol. Cells **38**(2), 180 (2015).

[89] Wang, Z., Fan, G., Hryc, C. F., Blaza, J. N., Serysheva, I. I., Schmid, M. F., Chiu, W., Luisi, B. F. and Du, D., "An allosteric transport mechanism for the AcrAB-TolC multidrug efflux pump," Elife **6**, e24905 (2017).

[90] Murakami, S., “Multidrug efflux transporter, AcrB-the pumping mechanism,” Curr. Opin. Struct. Biol. **18**(4), 459–465 (2008).

[91] Haddock, B. A. and Jones, C. W., “Bacterial respiration,” Bacteriol. Rev. **41**(1), 47 (1977).

[92] Nishino, K., Yamada, J., Hirakawa, H., Hirata, T. and Yamaguchi, A., “Roles of TolC-dependent multidrug transporters of Escherichia coli in resistance to β-lactams,” Antimicrob. Agents Chemother. **47**(9), 3030–3033 (2003).

[93] Elkins, C. A. and Nikaido, H., “Substrate specificity of the RND-type multidrug efflux pumps AcrB and AcrD of Escherichia coli is determined predominately by two large periplasmic loops,” J. Bacteriol. **184**(23), 6490–6498 (2002).

[94] Hirakawa, H., Nishino, K., Hirata, T. and Yamaguchi, A., “Comprehensive studies of drug resistance mediated by overexpression of response regulators of two-component signal transduction systems in Escherichia coli,” J. Bacteriol. **185**(6), 1851–1856 (2003).

[95] Nagakubo, S., Nishino, K., Hirata, T. and Yamaguchi, A., “The putative response regulator BaeR stimulates multidrug resistance of Escherichia coli via a novel multidrug exporter system, MdtABC,” J. Bacteriol. **184**(15), 4161–4167 (2002).

[96] Nishino, K. and Yamaguchi, A., “Analysis of a complete library of putative drug transporter genes in Escherichia coli,” J. Bacteriol. **183**(20), 5803–5812 (2001).

[97] Nishino, K. and Yamaguchi, A., “EvgA of the two-component signal transduction system modulates production of the YhiUV multidrug transporter in Escherichia coli,” J. Bacteriol. **184**(8), 2319–2323 (2002).

[98] Kobayashi, N., Nishino, K. and Yamaguchi, A., “Novel macrolide-specific ABC-type efflux transporter in Escherichia coli,” J. Bacteriol. **183**(19), 5639–5644 (2001).

[99] Lomovskaya, O. and Lewis, K., “emr, an Escherichia coli locus for multidrug resistance,” Proc. Natl. Acad. Sci. U. S. A. **89**(19), 8938–8942 (1992).

[100] Hobbs, E. C., Yin, X., Paul, B. J., Astarita, J. L. and Storz, G., “Conserved small protein associates with the multidrug efflux pump AcrB and differentially affects antibiotic resistance,” Proc. Natl. Acad. Sci. U. S. A. **109**(41), 16696–16701 (2012).

[101] Ma, D., Cook, D. N., Alberti, M., Pon, N. G., Nikaido, H. and Hearst, J. E., “Genes acrA and acrB encode a stress-induced efflux system of Escherichia coli,” Mol. Microbiol. **16**(1), 45–55 (1995).

[102] Ma, D., Alberti, M., Lynch, C., Nikaido, H. and Hearst, J. E., “The local repressor AcrR plays a modulating role in the regulation of acrAB genes of Escherichia coli by global stress signals,” Mol. Microbiol. **19**(1), 101–112 (1996).

[103] Webber, M. A., Talukder, A. and Piddock, L. J. V., “Contribution of mutation at amino acid 45 of AcrR to acrB expression and ciprofloxacin resistance in clinical and veterinary Escherichia coli isolates,” Antimicrob. Agents Chemother. **49**(10), 4390–4392 (2005).

[104] Su, C. C., Rutherford, D. J. and Yu, E. W., “Characterization of the multidrug efflux regulator AcrR from Escherichia coli,” Biochem. Biophys. Res. Commun. **361**(1), 85–90 (2007).

[105] Hirakawa, H., Takumi-Kobayashi, A., Theisen, U., Hirata, T., Nishino, K. and Yamaguchi, A., “AcrS/EnvR represses expression of the acrAB multidrug efflux genes in Escherichia coli,” J. Bacteriol. **190**(18), 6276–6279 (2008).

[106] Martin, R. G. and Rosner, J. L., “Transcriptional and translational regulation of the marRAB multiple antibiotic resistance operon in Escherichia coli,” Mol. Microbiol. **53**(1), 183–191 (2004).

[107] Alekshun, M. N. and Levy, S. B., “The mar regulon: Multiple resistance to antibiotics and other toxic chemicals,” Trends Microbiol. **7**(10), 410–413 (1999).

[108] Martin, R. G., Jair, K. W., Wolf, R. E. and Rosner, J. L., “Autoactivation of the marRAB multiple antibiotic resistance operon by the marA transcriptional activator in Escherichia coli,” J. Bacteriol. **178**(8), 2216–2223 (1996).

[109] Cohen, S. P., Levy, S. B., Foulds, J. and Rosner, J. L., “Salicylate induction of antibiotic resistance in Escherichia coli: Activation of the mar operon and a mar-independent pathway,” J. Bacteriol. **175**(24), 7856–7862 (1993).

[110] Ricci, V., Attah, V., Overton, T., Grainger, D. C. and Piddock, L. J. V., “CsrA maximizes expression of the AcrAB multidrug resistance transporter,” Nucleic Acids Res. **45**(22), 12798–12807 (2017).

[111] Nicoloff, H., Perreten, V., McMurry, L. M. and Levy, S. B., “Role for tandem duplication and lon protease in AcrAB-TolC-dependent multiple antibiotic resistance (Mar) in an Escherichia coli mutant without mutations in marRAB or acrRAB,” J. Bacteriol. **188**(12), 4413–4423 (2006).

[112] Ricci, V., Blair, J. M. A. and Piddock, L. J. V., “RamA, which controls expression of the MDR efflux pump AcrAB-Tolc, is regulated by the lon protease,” J. Antimicrob. Chemother. **69**(3), 643–650 (2014).

[113] Griffith, K. L., Shah, I. M. and Wolf, R. E., “Proteolytic degradation of Escherichia coli transcription activators SoxS and MarA as the mechanism for reversing the induction of the superoxide (SoxRS)

and multiple antibiotic resistance (Mar) regulons," Mol. Microbiol. **51**(6), 1801–1816 (2004).

[114] Costerton, J., "Bacterial Biofilms In Nature And Disease," Annu. Rev. Microbiol. **41**(1), 435–464 (1987).

[115] Webb, J. S., Givskov, M. and Kjelleberg, S., "Bacterial biofilms: Prokaryotic adventures in multicellularity," Curr. Opin. Microbiol. **6**(6), 578–585 (2003).

[116] Flemming, H. C., Wingender, J., Szewzyk, U., Steinberg, P., Rice, S. A. and Kjelleberg, S., "Biofilms: An emergent form of bacterial life," Nat. Rev. Microbiol. **14**(9), 563 (2016).

[117] Flemming, H. C. and Wuertz, S., "Bacteria and archaea on Earth and their abundance in biofilms," Nat. Rev. Microbiol. **17**(4), 247–260 (2019).

[118] Costerton, W. J. and Wilson, M., "Introducing Biofilms," Biofilms **1**(1), 1–4 (2004).

[119] Costerton, J. W., Stewart, P. S. and Greenberg, E. P., "Bacterial biofilms: A common cause of persistent infections," Science (80-.). **284**(5418), 1318–1322 (1999).

[120] James, G. A., Swogger, E., Wolcott, R., Pulcini, E. D., Secor, P., Sestrich, J., Costerton, J. W. and Stewart, P. S., "Biofilms in chronic wounds," Wound Repair Regen. **16**(1), 37–44 (2008).

[121] Hall-Stoodley, L. and Stoodley, P., "Evolving concepts in biofilm infections," Cell. Microbiol. **11**(7), 1034–1043 (2009).

[122] Anderl, J. N., Franklin, M. J. and Stewart, P. S., "Role of antibiotic penetration limitation in Klebsiella pneumoniae biofilm resistance to ampicillin and ciprofloxacin," Antimicrob. Agents Chemother. **44**(7), 1818–1824 (2000).

[123] Stewart, P. S., "Diffusion in biofilms," J. Bacteriol. **185**(5), 1485–1491 (2003).

[124] Hoyle, B. D., Alcantara, J. and Costerton, J. W., "Pseudomonas aeruginosa biofilm as a diffusion barrier to piperacillin," Antimicrob. Agents Chemother. **36**(9), 2054–2056 (1992).

[125] Barnhart, M. M. and Chapman, M. R., "Curli Biogenesis and Function," Annu. Rev. Microbiol. **60**(1), 131–147 (2006).

[126] Blanco, L. P., Evans, M. L., Smith, D. R., Badtke, M. P. and Chapman, M. R., "Diversity, biogenesis and function of microbial amyloids," Trends Microbiol. **20**(2), 66–73 (2012).

[127] Vidakovic, L., Singh, P. K., Hartmann, R., Nadell, C. D. and Drescher, K., "Dynamic biofilm architecture confers individual and collective mechanisms of viral protection," Nat. Microbiol. **3**(1), 26–31 (2018).

[128] Høiby, N., Bjarnsholt, T., Givskov, M., Molin, S. and Ciofu, O., "Antibiotic resistance of bacterial biofilms," Int. J. Antimicrob. Agents **35**(4), 322–332 (2010).

[129] Kvist, M., Hancock, V. and Klemm, P., "Inactivation of efflux pumps abolishes bacterial biofilm formation," Appl. Environ. Microbiol. **74**(23), 7376–7382 (2008).

[130] Van Acker, H. and Coenye, T., "The role of efflux and physiological adaptation in biofilm tolerance and resistance," J. Biol. Chem. **291**(24), 12565–12572 (2016).

[131] Kishen, A., Upadya, M., Tegos, G. P. and Hamblin, M. R., "Efflux pump inhibitor potentiates antimicrobial photodynamic inactivation of enterococcus faecalis biofilm," Photochem. Photobiol. **86**(6), 1343–1349 (2010).

[132] Bishop, P. L., “Biofilm structire and kinetics,” Water Sci. Technol. **36**(1), 287 (1997).

[133] Walters, M. C., Roe, F., Bugnicourt, A., Franklin, M. J. and Stewart, P. S., “Contributions of antibiotic penetration, oxygen limitation, and low metabolic activity to tolerance of Pseudomonas aeruginosa biofilms to ciprofloxacin and tobramycin,” Antimicrob. Agents Chemother. **47**(1), 317–323 (2003).

[134] Amato, S., Orman, M. and Brynildsen, M., “Metabolic Control of Persister Formation in Escherichia coli,” Mol. Cell **50**(4), 475–487 (2013).

[135] Sternberg, C., Christensen, B. B., Johansen, T., Nielsen, A. T., Andersen, J. B., Givskov, M. and Molin, S., “Distribution of bacterial growth activity in flow-chamber biofilms,” Appl. Environ. Microbiol. **65**(9), 4108–4117 (1999).

[136] Shah, D., Zhang, Z., Khodursky, A., Kaldalu, N., Kurg, K. and Lewis, K., “Persisters: A distinct physiological state of E. coli,” BMC Microbiol. **6**(1), 53 (2006).

[137] Lewis, K., “Multidrug tolerance of biofilms and persister cells,” Curr. Top. Microbiol. Immunol., 107–131 (2008).

[138] Hobby, G. L., Meyer, K. and Chaffee, E., “Observations on the Mechanism of Action of Penicillin,” Proc. Soc. Exp. Biol. Med. **50**(2), 281–285 (1942).

[139] Bigger, J. W., “Treatment of staphylococcal infections with penicillin by intermittent sterilization,” Lancet **247**, 497–500 (1944).

[140] Kim, J. S. and Wood, T. K., “Persistent persister misperceptions,” Front. Microbiol. **7**, 2134 (2016).

[141] Kwan, B. W., Valenta, J. A., Benedik, M. J. and Wood, T. K.,

"Arrested protein synthesis increases persister-like cell formation," Antimicrob. Agents Chemother. **57**(3), 1468–1473 (2013).

[142] Pu, Y., Zhao, Z., Li, Y., Zou, J., Ma, Q., Zhao, Y., Ke, Y., Zhu, Y., Chen, H., Baker, M. A. B., Ge, H., Sun, Y., Xie, X. S. and Bai, F., "Enhanced Efflux Activity Facilitates Drug Tolerance in Dormant Bacterial Cells," Mol. Cell **62**(2), 284–294 (2016).

[143] Orman, M. A. and Brynildsen, M. P., "Dormancy is not necessary or sufficient for bacterial persistence," Antimicrob. Agents Chemother. **57**(7), 3230–3239 (2013).

[144] Pu, Y., Zhao, Z., Li, Y., Zou, J., Ma, Q., Zhao, Y., Ke, Y., Zhu, Y., Chen, H., Baker, M. A. B., Ge, H., Sun, Y., Xie, X. S. and Bai, F., "Enhanced Efflux Activity Facilitates Drug Tolerance in Dormant Bacterial Cells," Mol. Cell **62**(2), 284–294 (2016).

[145] Bailey, A. M., Webber, M. A. and Piddock, L. J. V., "Medium plays a role in determining expression of acrB, marA, and soxS in Escherichia coli," Antimicrob. Agents Chemother. **50**(3), 1071–1074 (2006).

[146] Hayashi, S., Aono, R., Hanai, T., Mori, H., Kobayashi, T. and Honda, H., "Analysis of organic solvent tolerance in Escherichia coli using gene expression profiles from DNA microarrays," J. Biosci. Bioeng. **95**(4), 379–383 (2003).

[147] Sánchez-Céspedes, J. and Vila, J., "Partial characterisation of the acrAB locus in two Citrobacter freundii clinical isolates," Int. J. Antimicrob. Agents **30**(3), 259–263 (2007).

[148] Rand, J. D., Danby, S. G., Greenway, D. L. A. and England, R. R., "Increased expression of the multidrug efflux genes acrAB occurs during slow growth of Escherichia coli," FEMS Microbiol. Lett. **207**(1), 91–95 (2002).

[149] Fralick, J. A., “Evidence that TolC is required for functioning of the Mar/AcrAB efflux pump of Escherichia coli,” J. Bacteriol. **178**(19), 5803–5805 (1996).

[150] Fu, G., Huang, T., Buss, J., Coltharp, C., Hensel, Z. and Xiao, J., “In Vivo structure of the E. coli FtsZ-ring revealed by photoactivated localization microscopy (PALM),” PLoS One **5**(9) (2010).

[151] Buss, J., Coltharp, C., Huang, T., Pohlmeyer, C., Wang, S. C., Hatem, C. and Xiao, J., “In vivo organization of the FtsZ-ring by ZapA and ZapB revealed by quantitative super-resolution microscopy,” Mol. Microbiol. **89**(6), 1099–1120 (2013).

[152] Shroff, H., White, H. and Betzig, E., “Photoactivated localization microscopy (PALM) of adhesion complexes,” Curr. Protoc. Cell Biol. **41**(1), 4–21 (2008).

[153] Subach, F. V., Zhang, L., Gadella, T. W. J., Gurskaya, N. G., Lukyanov, K. A. and Verkhusha, V. V., “Red fluorescent protein with reversibly photoswitchable absorbance for photochromic FRET,” Chem. Biol. **17**(7), 745–755 (2010).

[154] Brakemann, T., Stiel, A. C., Weber, G., Andresen, M., Testa, I., Grotjohann, T., Leutenegger, M., Plessmann, U., Urlaub, H., Eggeling, C., Wahl, M. C., Hell, S. W. and Jakobs, S., “A reversibly photoswitchable GFP-like protein with fluorescence excitation decoupled from switching,” Nat. Biotechnol. **29**(10), 942 (2011).

[155] Habuchi, S., Ando, R., Dedecker, P., Verheijen, W., Mizuno, H., Miyawaki, A. and Hofkens, J., “Reversible single-molecule photoswitching in the GFP-like fluorescent protein Dronpa,” Proc. Natl. Acad. Sci. U. S. A. **102**(27), 9511–9516 (2005).

[156] Chang, H., Zhang, M., Ji, W., Chen, J., Zhang, Y., Liu, B., Lu, J., Zhang, J., Xu, P. and Xu, T., “A unique series of reversibly switchable

fluorescent proteins with beneficial properties for various applications," Proc. Natl. Acad. Sci. U. S. A. **109**(12), 4455–4460 (2012).

[157] Gurskaya, N. G., Verkhusha, V. V., Shcheglov, A. S., Staroverov, D. B., Chepurnykh, T. V., Fradkov, A. F., Lukyanov, S. and Lukyanov, K. A., "Engineering of a monomeric green-to-red photoactivatable fluorescent protein induced by blue light," Nat. Biotechnol. **24**(4), 461–465 (2006).

[158] Habuchi, S., Tsutsui, H., Kochaniak, A. B., Miyawaki, A. and van Oijen, A. M., "mKikGR, a monomeric photoswitchable fluorescent protein," PLoS One **3**(12) (2008).

[159] Ando, R., Hama, H., Yamamoto-Hino, M., Mizuno, H. and Miyawaki, A., "An optical marker based on the UV-induced green-to-red photoconversion of a fluorescent protein," Proc. Natl. Acad. Sci. U. S. A. **99**(20), 12651–12656 (2002).

[160] Subach, O. M., Patterson, G. H., Ting, L. M., Wang, Y., Condeelis, J. S. and Verkhusha, V. V., "A photoswitchable orange-to-far-red fluorescent protein, PSmOrange," Nat. Methods **8**(9), 771 (2011).

[161] Wiedenmann, J., Ivanchenko, S., Oswald, F., Schmitt, F., Röcker, C., Salih, A., Spindler, K. D. and Nienhaus, G. U., "EosFP, a fluorescent marker protein with UV-inducible green-to-red fluorescence conversion," Proc. Natl. Acad. Sci. U. S. A. **101**(45), 15905–15910 (2004).

[162] Yamamoto, K., Tamai, R., Yamazaki, M., Inaba, T., Sowa, Y. and Kawagishi, I., "Substrate-dependent dynamics of the multidrug efflux transporter AcrB of Escherichia coli," Sci. Rep. **6**(1), 1–10 (2016).

[163] Datsenko, K. A. and Wanner, B. L., "One-step inactivation of chromosomal genes in Escherichia coli K-12 using PCR products,"

Proc. Natl. Acad. Sci. U. S. A. **97**(12), 6640–6645 (2000).

[164] Reisch, C. R. and Prather, K. L. J., "The no-SCAR (Scarless Cas9 Assisted Recombineering) system for genome editing in Escherichia coli," Sci. Rep. **5**(1), 1–12 (2015).

[165] Sharan, S. K., Thomason, L. C., Kuznetsov, S. G. and Court, D. L., "Recombineering: a homologous recombination-based method of genetic engineering," Nat. Protoc. **4**(2), 206–223 (2009).

[166] Mosberg, J. A., Lajoie, M. J. and Church, G. M., "Lambda red recombineering in Escherichia coli occurs through a fully single-stranded intermediate," Genetics **186**(3), 791–799 (2010).

[167] Sauer, B., "Functional expression of the cre-lox site-specific recombination system in the yeast Saccharomyces cerevisiae.," Mol. Cell. Biol. **7**(6), 2087–2096 (1987).

[168] Sauer, B. and Henderson, N., "Site-specific DNA recombination in mammalian cells by the Cre recombinase of bacteriophage P1.," Proc. Natl. Acad. Sci. U. S. A. **85**(14), 5166–5170 (1988).

[169] Kuhlman, T. E. and Cox, E. C., "Site-specific chromosomal integration of large synthetic constructs," Nucleic Acids Res. **38**(6), e92–e92 (2010).

[170] Wenyan Jiang, David Bikard, David Cox, Feng Zhang, and L. A. M., "CRISPR-assisted editing of bacterial genomes," Nat biotechnol **31**(3), 233–239 (2013).

[171] Pyne, M. E., Moo-Young, M., Chung, D. A. and Chou, C. P., "Coupling the CRISPR/Cas9 system with lambda red recombineering enables simplified chromosomal gene replacement in Escherichia coli," Appl. Environ. Microbiol. **81**(15), 5103–5114 (2015).

[172] Anders, C., Niewoehner, O., Duerst, A. and Jinek, M., "Structural

basis of PAM-dependent target DNA recognition by the Cas9 endonuclease," Nature **513**(7519), 569–573 (2014).

[173] Mali, P., Esvelt, K. M. and Church, G. M., "Cas9 as a versatile tool for engineering biology," Nat. Methods **10**(10), 957–963 (2013).

[174] Gustafsson, C., Govindarajan, S. and Minshull, J., "Codon bias and heterologous protein expression," Trends Biotechnol. **22**(7), 346–353 (2004).

[175] Grosjean, H. and Fiers, W., "Preferential codon usage in prokaryotic genes: the optimal codon-anticodon interaction energy and the selective codon usage in efficiently expressed genes," Gene **18**(3), 199–209 (1982).

[176] Yarus, M. and Folley, L. S., "Sense codons are found in specific contexts," J. Mol. Biol. **182**(4), 529–540 (1985).

[177] Shpaer, E. G., "Constraints on codon context in Escherichia coli genes their possible role in modulating the efficiency of translation," J. Mol. Biol. **188**(4), 555–564 (1986).

[178] Berg, O. G. and Silva, P. J. N., "Codon bias in Escherichia coli: The influence of codon context on mutation and selection," Nucleic Acids Res. **25**(7), 1397–1404 (1997).

[179] Chin, J. X., Chung, B. K. S. and Lee, D. Y., "Codon Optimization OnLine (COOL): A web-based multi-objective optimization platform for synthetic gene design," Bioinformatics **30**(15), 2210–2212 (2014).

[180] "Replica Plating - an overview | ScienceDirect Topics.", <https://www.sciencedirect.com/topics/biochemistry-genetics-and-molecular-biology/replica-plating> (10 October 2019).

[181] "Determination of minimum inhibitory concentrations (MICs) of

antibacterial agents by broth dilution.", Clin. Microbiol. Infect. **9**(8), ix–xv (2003).

[182] Baba, T., Ara, T., Hasegawa, M., Takai, Y., Okumura, Y., Baba, M., Datsenko, K. A., Tomita, M., Wanner, B. L. and Mori, H., "Construction of Escherichia coli K-12 in-frame, single-gene knockout mutants: The Keio collection," Mol. Syst. Biol. **2**(1) (2006).

[183] Bohnert, J. A. and Kern, W. V., "Selected arylpiperazines are capable of reversing multidrug resistance in Escherichia coli overexpressing RND efflux pumps," Antimicrob. Agents Chemother. **49**(2), 849–852 (2005).

[184] Garvey, M. I. and Piddock, L. J. V., "The efflux pump inhibitor reserpine selects multidrug-resistant Streptococcus pneumoniae strains that overexpress the ABC transporters PatA and PatB," Antimicrob. Agents Chemother. **52**(5), 1677–1685 (2008).

[185] Beyer, H. M., Gonschorek, P., Samodelov, S. L., Meier, M., Weber, W. and Zurbriggen, M. D., "AQUA cloning: A versatile and simple enzyme-free cloning approach," PLoS One **10**(9) (2015).

[186] "CaCl2 Transformation Technique | MyBioSource Learning Center.", <https://www.mybiosource.com/learn/testing-procedures/cacl2-transformation-technique/> (10 October 2019).

[187] Warren, D. J., "Preparation of highly efficient electrocompetent Escherichia coli using glycerol/mannitol density step centrifugation," Anal. Biochem. **413**(2), 206–207 (2011).

9 Acknowledgements

First, I would like to express my gratitude to Prof. Francesco S. Pavone, for giving me the opportunity to become part of the Biophotonics group at LENS, and for providing me with the means and infrastructure to carry out all of the work I did here. I still remember the first time I walked through the corridors of the ground floor, as Marco was showing me around the workshops and the labs. I thought out loud: “this is the coolest lab I’ve ever seen!”. And I kept thinking the same for three years, even after becoming used to it, after experiencing the messy workspaces and overcrowded benches, even after the overnight blackouts killed all of my cells and stopped the computer in the middle of analysis – which happened multiple times. I kept thinking that LENS is, first and foremost, a bloody cool place. Because when you have a bunch of creatively-minded biologists, physicists, chemists, engineers helping each other out and working together in such close contact (and in such little space!), cool and unusual science is bound to happen. Also, it’s chock-full of lasers. So yeah, I am extremely grateful for having been given the opportunity to work here, to be enriched by this mess and – hopefully – to enrich this mess with some little contribution of mine.

Then my deepest and sincerest thanks go to Marco and Lucia, who together directed me and helped me in more ways than I can count, and fundamentally taught me what it means to be a scientist. You took an overenthusiastic, overly emotional kid and somehow implanted in him the notions of planning ahead, of being thorough, of keeping a cool head when trying to deal with a problem. I would have accomplished *nothing* without you.

Then I absolutely need to thank Claudia and Martino, who pretty much taught me everything I know about wet lab techniques. I got into LENS with a computational biology training and a crippling imposter syndrome, without any hands-on experience whatsoever concerning cells and bacteria, and with three years ahead of me to spend working with cells and bacteria. I was terrified to even ask for help, but you two were always so kind and helpful (not to mention skilled) that I somehow managed to get over it. I am now able to make HEK 293 cells die in the incubator without any contamination nor discernible cause, which is an ability that only the most powerful of biologists can wield. And this is all thanks to you guys. Also, I'd like to thank Claudia for feeding me sfogliatelle on a regular basis and Martino for… well, being Martino.

Now I want to address Valentina, who started alongside me in late 2016, as a thesis student who was way more capable than me, someone who was trying to pass as a PhD candidate. She is now pursuing her own scientific career in Marseille, but we shared the first part of this adventure and I have absolutely no idea how I would have figured out a great chunk of my thesis' work without her. Vale, you are absolutely brilliant and I wish you all the best. I hope we get to meet again soon.

I also need to thank Alessio, who always kept supporting and encouraging me after being the advisor for my Master's thesis. If it wasn't for you (and your electroporator!) I would still be trying to punch DNA in bacteria by screaming at them and praying to Padre Pio.

And now I want to thank all of my everyday companions who made LENS feel like more of a second home: my lab and lunch buddies Laura, Marios (R.I.P.), Eros, Antonino, Claudia, Francesco, Caterina, as well as all of the fellow inhabitants of the chicken coop.

A special thank you goes to Blanka, for giving me the strength to burn through countless pages by providing me with the official soundtrack of these last few harrowing months of writing (Oldschool Runescape: Sea Shanty 2 (10 hours extended)).

Finally, a huge thank you goes to my parents. When I talk about you with my friends, I always say that I have won the parents lottery and everyone agrees. Of course I have never told you this because it is hard for me to express feelings directly, but I can safely write it here since you cannot understand a word of English. I really appreciate all the love and support you have given me for 27 years.

Actually, I was joking. Not about my parents, but about it being the final thank you.

My final and most important thank you goes to Erika. Even though we are currently 1,413.03 kilometers apart, you are the single largest influence in my life. You are the best human I know and all my efforts toward bettering myself boil down to the eternal competition between the two of us that has been going on for the better part of a decade. You taught me that good things come from creative people, in all fields of human activity, and that artists and scientists have a whole lot in common. You are what has kept me going through my darkest times, and you managed to turn this hugely stressful experience of getting a PhD into what have arguably been the best 3 years of my life.